2004

Transport and deposition of fluid mud event layers along the western Louisiana inner shelf

Kristina Anne Rotondo
Louisiana State University and Agricultural and Mechanical College

TRANSPORT AND DEPOSITION OF FLUID MUD EVENT LAYERS ALONG THE WESTERN LOUISIANA INNER SHELF

A Thesis

Submitted to the Graduate Faculty of the
Louisiana State University and
Agricultural and Mechanical College
in partial fulfillment of the
requirements for the degree of
Master of Science

in

The Department of Oceanography and Coastal Sciences

by
Kristina Rotondo
B.A., State University of New York at Geneseo, 2000
August 2004

ACKNOWLEDGEMENTS

First, I would like to thank Dr. Sam Bentley for his endless patience, support, guidance and answers to the dumb questions. I would also like to thank my committee members Dr. Harry Roberts and Dr. Jaye Cable, for providing valuable feedback and insight.

Many others have been helped with lab and field work, and have demonstrated that they are not afraid to get dirty: Brian Velardo, Triniti Dufrene, Luke Patterson, Zahid Muhammad, Keegan Roberts, Judith Barnes, Will Vienne, Steven Chan, Chris Dautreve.

Thanks to Floyd DeMers and all the technicians and student workers in the Coastal Studies Institute. Also, many thanks to the captain and crew of the R/V Acadiana.

Finally, I would like to thank my family and friends, most of who think I am crazy for wanting to travel the world to look at mud, but have supported me at every step of the way.

Support for this project was provided by NSF CAREER grant OCE-009-3209 to Dr. S. J. Bentley.

TABLE OF CONTENTS

ABSTRACT

The western Louisiana inner shelf along the Chenier Plain coast has experienced fluid mud deposition in response to increased fine sediment supplied by the Atchafalaya River since ~1950's. The goal of this project is to assess the characteristics comprising the sedimentary strata and stratigraphic architecture that result from mud deposition on the inner shelf. Recent time-series cores collected from the inner shelf along the Chenier plain coast show the region is subject to transient fluid mud deposition, leading to high long-term accumulation rates. Sediment cores were collected in May 2001, March and May 2002 from the inner shelf landward of the 10 m isobath, 100 km west of Atchafalaya Bay. Porosity, granulometry, X-radiography, and ^{7}Be, ^{210}Pb and ^{137}Cs geochronology indicate the presence of high-porosity event layers 2-25 cm thick composed of clay with basal silt laminations. These event layers appear to concentrate around a depocenter located 95-110 km west of the Atchafalaya River, landward of the 7 m isobath, but can be ephemeral features on a seasonal time scale.

The combination of high-energy benthic hydrodynamics and sufficient fine sediment can result in cross-shelf gravity-driven flows (on very low slopes) that can blanket hundreds of square kilometers to thicknesses exceeding 10 cm. The sedimentary fabric that results from gravity-driven flows consists of a stacked pattern of predominantly fine-grained, fining upward packages. The resulting morphology of the shelf may be a clinoform, with maximum deposition occurring on the foreset (convex upward) region. The observations from the western Louisiana inner shelf (mud/silt couplets that comprise the fine-scale stratigraphy of the region, ephemeral ^{7}Be deposits, and clinoform morphology exhibiting erosional features in sidescan and chirp data) are consistent with the wave-enhanced gravity-driven flow model. These results indicate that

wave-enhanced gravity driven flows may be an important component in the dispersal of Atchafalaya River sediment.

INTRODUCTION AND SIGNIFICANCE

The general objective of this research is to contribute to our understanding of the transport and deposition of cohesive shelf sediments along muddy coastlines. Through analysis of sedimentology, sediment acoustic surveys, and sediment radiochemistry, this study attempts to piece together how short-term event sedimentation contributes to the long-term sediment record of the Western Louisiana inner shelf.

Muddy coastlines are found worldwide, common on all continents except Antarctica, and in regions with a high and continual supply of fine-grained sediment. Muddy coasts encompass over 20% of the world's coastline, but have not received sufficient attention relative to their sandy counterpart. Differences in sediment properties and behaviors of muddy and sandy coasts make models that have been developed for sediment transport and coastal evolution inapplicable to muddy coastlines (Kemp, 1986; Kirby, 2002). Research over the past few decades has shown that mud does not accumulate only in quiescent environments over long periods of time, as commonly believed, but it can be deposited rapidly, under the influence of waves and currents, and on extremely short time scales (hours, days, weeks) (Wells and Coleman, 1981; Wells and Kemp, 1981; Kineke et al., 1996; Sommerfield et al., 2000; Wright et al., 2001; Walsh et al., in press). There are many unknown and unquantified aspects of sediment transport and depositional processes associated with fine sediments (Wang et al., 2002). Additional research is needed to fully understand not only muddy coastlines, but also to recognize ancient mud deposits that may have formed in a similar manner.

Prior to the mid-twentieth century, muddy coastlines received little scientific consideration. Early research was funded by the Office of Naval Research to improve military ability to land craft along muddy coasts (Morgan, 1953). This research, conducted mainly along

the Chenier coast of western Louisiana, identified mudflat formation along an open, unsheltered coastline, and documented mud deposition during high energy sediment-transport events, such as cold-fronts and hurricanes, where erosion typically occurs on sandy coasts (Morgan, 1959; Kemp, 1986). Research on muddy coasts has expanded from the Louisiana coast to regions worldwide, to study coastlines, as well as the sediments accumulating along the adjacent inner shelf. Coastal mudflat accumulations have been studied along the Surinam coast, where Wells and Coleman (1977) first documented the progressive nearshore attenuation of wave energy along the inner shelf in areas of high suspended sediment concentration. The reduced wave energy was linked to reduced shear stress, and produced a positive feedback loop of increased deposition of suspended sediment carried by incoming waves (Wells and Roberts, 1981).

More recently, studies have focused on fluid muds that accumulate on the inner shelf along muddy coastlines. Fluid muds are defined as high concentration (>10 g l^{-1}) near-bed suspensions of fine-grained sediments and have been observed in many estuarine, coastal and shelf environments. Fluid muds typically occur during decelerating or slack currents where the deposition rate is too fast to permit consolidation of a mud bed (Kineke et al., 1996). However, fluid mud is not considered part of the consolidated seabed because it lacks mechanical strength (Mehta, 1991; Kineke et al., 1996).

It is likely that high-concentration near-bed sediment suspensions are more common and widespread than previously thought and are important modes of fine sediment transport in shelf systems (Wright et al., 2001). Fluid mud deposits have also been studied in the Gulf of Bohai off the mouth of the Yellow River (Wright et al., 2001), along the northern California coast (Eel River; Traykovski et al., 2000; Wright et al., 2001; Nittrouer, 1999; Ogston et al., 2000), and the

Amazon River (Kineke and Sternberg, 1995; Kuehl et al., 1995), in various tide ranges and wave energy regimes.

The AmasSeds project (A Multi-disciplinary Amazon Shelf SEDiment Study) was started in 1989 in order to better understand the oceanic processes associated with the large flux of sediment discharged from the Amazon River (Kineke et al., 1996). The study mapped thick (up to several meters) fluid mud deposits on the inner and mid-shelf regions. The deposits were found to be most extensive during periods of rising and high river discharge. Most sediment transport occurred within the bottom layers of the water column, not in the surface plume (Kineke and Sternberg, 1995; Kuehl et al., 1995).

Eel River studies, as a part of the STRATAFORM program, discovered that episodic flooding resulting from large winter storms allowed for high sediment discharge that coincided with high waves and strong wind-driven currents. Flood deposits formed during this time are internally stratified, consisting of alternating layers of cm-scale silty clay (likely deposited due to individual gravity flows) interbedded with silt/sand crossbeds and laminations (deposited during periods of lower sediment supply), overlying coarser bioturbated sediment that develops from seabed mixing in between flood events (Bentley and Nittrouer, 2003). Data from instrumented bottom boundary layer tripods indicated that sediment is redistributed across the continental shelf (Traykovski et al., 2000; Wright et al., 2001; Ogston et al., 2000). Acoustic backscatter sensor data showed a 10-15 cm thick, high concentration (>10 g l^{-1}) layer that appeared during periods of high and decelerating wave velocity. This layer had a sharp lutocline, typical of fluid mud suspensions; above the lutocline, the magnitude of seaward flux was much less than the flux associated with the gravity flows (Traykovski et al., 2000). The processes observed are similar to those seen on the Amazon shelf.

Prior to these studies, fluid muds and hyperpycnal plumes were only thought of as rarely occurring cases and were associated only with unusually large or sediment-laden depositional systems (Wright and Nittrouer, 1995). While it has been determined that dynamic muddy coastlines occur worldwide, the Western Louisiana inner shelf, where muddy coasts were first recognized as unique and ambiguous features, remains an excellent region to study transport and deposition of fine sediment. The objectives of this study are threefold: (1) to describe the sedimentology of an individual fluid mud event deposit on the inner shelf; (2) to determine sediment accumulation rates for the inner shelf; and (3) to use these observations to link present-day processes to the formation of the sedimentary strata and overall stratigraphic architecture.

Regional Geologic and Hydrographic Setting

The Mississippi River system drainage basin covers 3,334,560 km^2, about 70% of the United States, as well as parts of two Canadian provinces (Roberts, 1997). The river discharges an average of >15,360 $m^3 s^{-1}$ of freshwater into the Gulf of Mexico. Since the Holocene sea level rise, the process of delta switching on the Mississippi Delta has produced a delta complex consisting of at least six lobes (Fig. 1). Switching occurs every 1,000-2,000 years and consists of 3 major steps: (1) rapid delta growth, with increasing sediment discharge and sediment flux, (2) relative stability and decreasing hydraulic efficiency, and (3) rapid delta deterioration, leading to decreasing discharge and delta abandonment (Roberts, 1997). The Modern Balize delta of the Mississippi River is still building but is increasingly inefficient. The Atchafalaya River is presently capturing significant discharge from the river and building the youngest lobe of the delta complex. The Atchafalaya course has a gradient advantage; being 307 km closer to the Gulf of Mexico, as well as a hydraulic head advantage, with its surface typically ~5 m below that of the Mississippi at the capture site (Fisk, 1952). The Atchafalaya has been capturing

Mississippi River discharge since at least the 1500's, with discharge steadily increasing in the 1900s until 1963, when the Old River Control Structure was built to prevent the complete capture of the current Mississippi River discharge. Flow down the Atchafalaya River is presently regulated to ≤ 30% of Mississippi River discharge plus the contribution from the Red River.

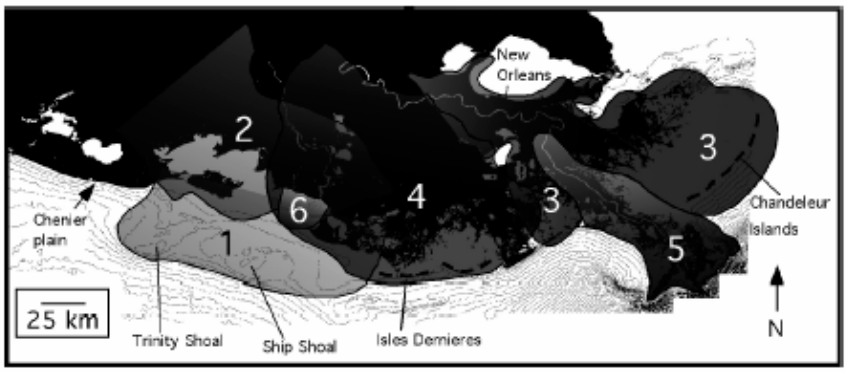

Youngest	Approximate Age
6. Atchafalaya	500 BP - present
5. Modern (Balize)	1000 BP - present
4. Lafourche	1500 - 500 BP
3. St. Bernard	4600 - 700 BP
2. Teche	5700 - 3900 BP
1. Maringouin	7200 - 6200 BP
Oldest	

Figure 1. Major lobes of the Mississippi River delta complex, based on Frasier (1967). The modern (Balize) Mississippi Delta and the Atchafalaya Delta are currently receiving sediment (Draut, 2003).

With the increased flow down the Atchafalaya River came the increased sediment discharge into the Gulf of Mexico. Once the river infilled the lakes and swamps of Atchafalaya basin, sediment was transported to Atchafalaya Bay, where it began the formation of subaqueous deltas at both the mouth of the Atchafalaya and Wax Lake outlet and reactivated mudflat accumulation along the Chenier coast (Fig. 2). After major flooding in 1973, the Wax Lake and

Atchafalaya deltas became subaerial features. From that time to the present, sandy sediment is being deposited in the delta, and finer sediment bypasses directly to the continental shelf, where some fraction is transported west to the Chenier Plain coast by prevailing currents (Roberts et al., 1980). This westward flow of sediment is a turbid plume that has been termed the "Atchafalaya Mud Stream" (Wells and Kemp, 1981). The mudstream is a highly variable residual flow

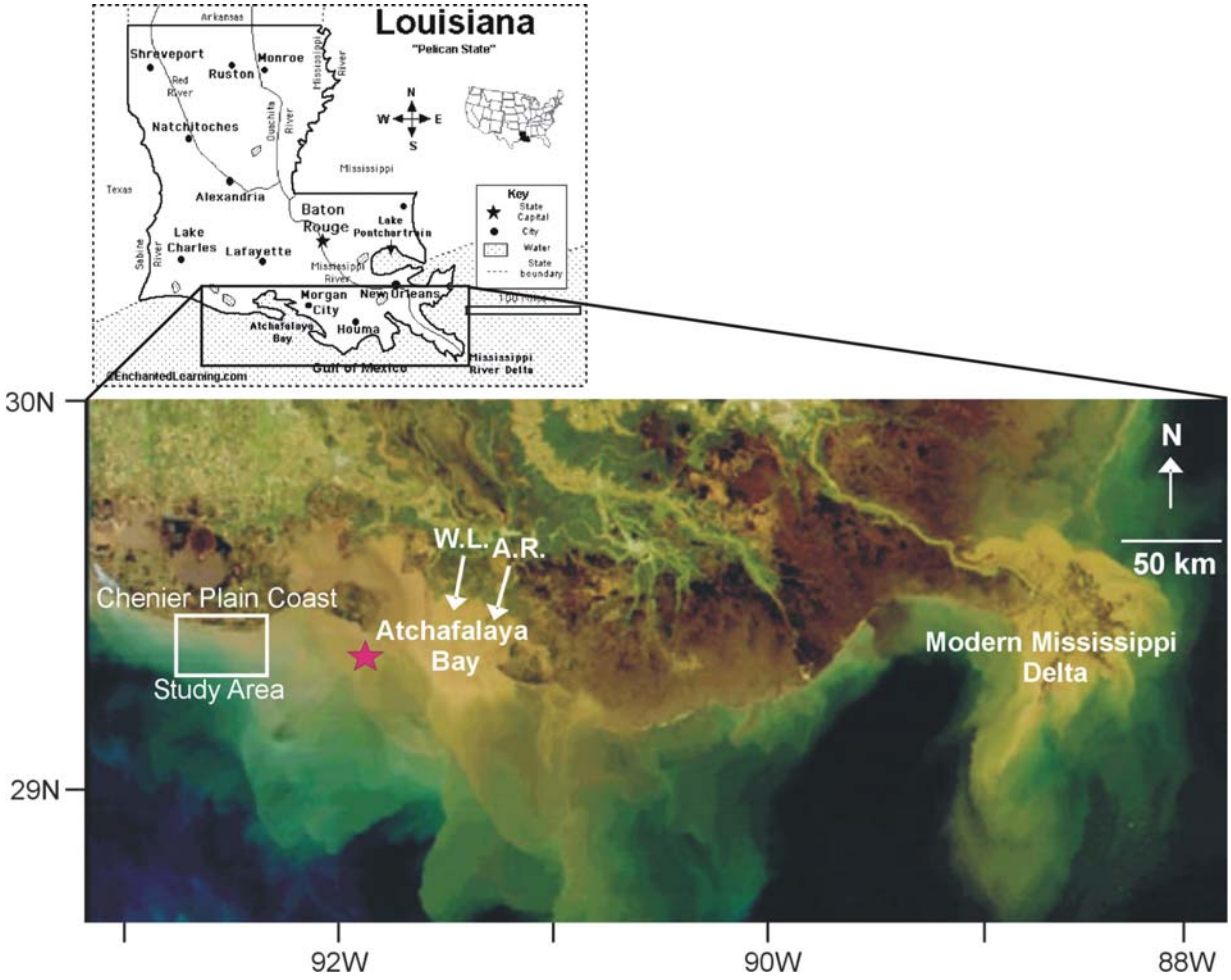

Figure 2. Location map of the state of Louisiana, with the black box outlining the region of interest (http://www.enchantedlearning.com/usa/statesbw/louisiana.html). Inset: Satellite image, collected March 5, 2001, during peak river discharge. The image shows the location of the modern Mississippi Delta, the study area along the Chenier plain coast, Atchafalaya River (A.R.) and Wax Lake (W.L.) outlets into Atchafalaya Bay, and the WAVCIS CSI-3 ocean observation station, denoted by a star (LSU Earth Scan Lab).

influenced by river discharge, tide stage, wind speed and direction (Wells and Kemp, 1981). It carries ~ $20x10^6$ t y^{-1} of sediment (Roberts, 1998), some of which is carried westward and deposited as annual flood deposit of fluid mud on the western Louisiana inner shelf (Allison et al., 2000). These muds are low density (1.10-1.35 g cm^{-3}) with high water content (61-89%). Once this mud is transported to the coastline, net deposition leads to long-term accumulation, causing the progradation of the Chenier Plain coastline (Wells and Kemp, 1981).

The Chenier Plain is located approximately 100 km west of Atchafalaya Bay (Fig. 2). It consists of alternating transgressive sandy or shelly ridges and regressive mudflats. Research by Howe et al. (1935) and Russell and Howe (1935) determined the Chenier coast formed during the Holocene by alternating deposition and erosion due to delta switching of the Mississippi River. Fisk and McFarlan (1955) first suggested it might be possible to correlate progradational events of the Chenier Plain to the proximal location of specific Mississippi subdeltas. Gould and McFarlan (1959) used radiocarbon dating to demonstrate that chenier formation was associated with the changing location of the Mississippi River and its associated sediment supply through time. Deposition occurs as mudflat progradation due to the proximity of the Mississippi River distributary in the delta plain. During periods when the Mississippi River delta is in the eastern part of the delta plain, distal to the Chenier Plain, wave activity reworks the muddy coastline into sandy/shelly ridges. Accumulation and mudflat progradation occur when river outlets are closest to the Chenier Plain. The last period of coastline progradation occurred about 1,000 years ago (Huh et al., 2001). Due to increasing discharge down the Atchafalaya River, mudflat progradation along the Chenier Plain has been reinitiated. The modern coastline began its transition from an erosional to a progradational coastline in the late 1940s (Roberts, 1998) and Morgan et al. (1953) began documenting this occurrence in the early 1950s.

Cold fronts (interfaces between cold, dry polar air traveling south and warm moist air traveling north) play a major role in the deposition of fluid mud and progradation of the coastline. Cold fronts make passages through the region 20-30 times per year during fall, winter and early spring. During a cold front passage, the wind direction shifts in a clockwise fashion, from pre-frontal southerly winds, which cause water level set-up, to westerly winds during the passage, to northerly post-frontal winds that cause air temperature and humidity to decrease significantly. The long fetch pre-frontal southerly winds create high wave activity against the coast, resuspending sediments and pushing mud-laden water over the coastal mudflats. After passage of the cold front, the rapid shift in wind direction to northerly winds causes water level set down, leaving mud stranded on the coastline, where it dessicates and forms hard cobbles that stabilize the coast and are quickly colonized by *Spartina* and *Panicum*. Previous studies have observed this process as the accumulation of transitory mudflats and mud "arcs" along the coast, causing only localized areas of progradation surrounded by widespread shoreline retreat (Wells and Kemp, 1981; Kemp, 1986). However, since 1987, coastal progradation has been increasing in overall scale and rate, with the coastline prograding at rates up to and exceeding 50 m y^{-1} (Fig. 3) (Huh et al, 2001).

While it is evident that cold fronts have a very important impact along the coastline, tropical cyclones also have an impact on the Louisiana coastline. Tropical systems differ from cold fronts in that they can be severe storms with higher wind speed, precipitation, waves, and storm surge. However, they generally impact smaller regions and are less frequent. Hurricanes along sand-dominated coasts can cause severe erosion. In contrast, tropical cyclones that impact muddy coastlines have effects similar to those of cold fronts. Tropical cyclones can contribute to coastal progradation by driving flux convergence along the coastline due to shoreward sediment

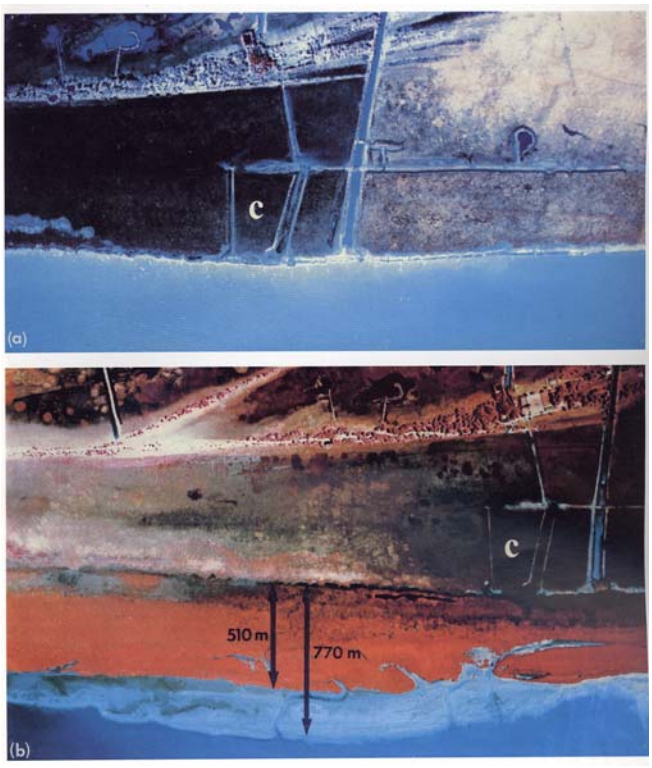

Figure 3. Aerial photographs showing progradation of the Chenier coast from 1987 to 1998. In 1998, there was an additional 770 m (510 m vegetated, 260 m non-vegetated) of mudflat along the coast (Huh et al., 2001).

transport and wave attenuation. Morgan (1959) noted such effects after Hurricane Audrey, which made landfall near the Louisiana-Texas border in 1957. The hurricane caused coastal retreat along most of the Chenier Plain except the areas dominated by mudflats, where coastline progradation occurred. While individual hurricane events may be more severe, cold fronts occur more frequently, impact larger regions, occur at much larger spatial scales and have repeated patterns of wind and wave forcing. As a result, cold fronts can have a more important continual impact on the coast.

Remote sensing is an invaluable tool being used to document changes in the coastline, as well as processes that contribute to fluid mud formation. High and low altitude color aerial photography is used to detect and measure changes in coastal geomorphology. Imagery from

NOAA AVHRR and Terra-MODIS satellites area also used to detect the changes in coastline morphology as well as the distribution of suspended sediment concentrations and current flow regimes in the Gulf of Mexico. Utilizing these technologies, researchers have documented impacts that weather systems can have on coastal regions (Roberts et al., 1989; Walker and Hammack, 2000; Huh et al., 2001). Between 1989 and 1994, NOAA satellite imagery shows the westward flow of Atchafalaya River mudstream occurs under the influence of NE and SE winds, which dominate all seasons except summer (Huh et al., 2001). Satellite observations also show that the Atchafalaya plume, which can extend 30-40 km seaward, results mainly from the resuspension of bottom sediments by wind-waves (Huh et al., 2001; Walker and Hammack, 2000). During the passage of a cold front, wind direction changes from southerly to northerly winds caused reduced water levels and significant sediment resuspension on the inner shelf. Clear-sky NOAA-14 AVHRR satellite imagery from the LSU EarthScan Lab (www.esl.lsu.edu) shows the increase in sediment concentration, as well as the increased areal extent (from ~1100 km^2 to 4400 km^2) of the mudstream. Time-series observations (Fig. 4), taken before and after the passage of a cold front in 1997, show the impact of winter storms on the suspended sediment concentration in Atchafalaya Bay and adjacent inner shelf. Figure 4B shows the two-lobed structure of the sediment plume similar in morphology to the 10 m isobath, indicating the high suspended sediment concentration is due to sediment resuspension. During these periods of high energy and resuspension, surface sediment concentrations in the mudstream can exceed 200 mg l^{-1} (Walker and Hammack, 2000).

While many of these studies have qualitatively described mud deposition and have identified the basic transport and depositional processes that contribute to fluid mud accumulation along the Chenier coast (seasonal Atchafalaya discharge, westward currents, cold

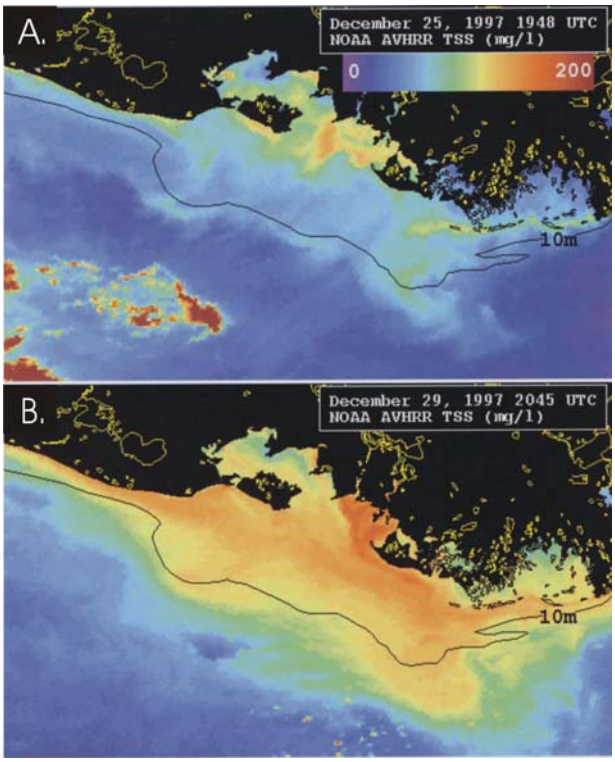

Figure 4. NOAA-14 AVHRR satellite imagery (A) during pre-frontal conditions; and (B) during post-frontal conditions. The scale relates image colors to suspended sediment concentration in mg l^{-1}. The 10 m isobath is drawn on the figure. Note how the two-lobed structure of the sediment plume follows the morphology of the isobath during post-frontal conditions (adapted from Walker and Hammack, 2000).

front forcing), Kemp (1986) is responsible for first quantitatively describing mud deposition on the shelf and subsequent mudflat formation. Through a four-day dynamics experiment during a cold front passage, Kemp (1986) concluded that the incident waves could be described by linear wave theory but exhibited progressive nearshore attenuation and absence of breaking, decreasing shear stress on the mud bottom and causing deposition nearshore. This effect is opposite of what occurs on sand-dominated coastlines.

Onshore transport of fluid mud occurs by low frequency flows associated with shore-amplified water-level oscillations. During the passage of a cold front, water-level oscillations are caused by setup and set-down associated with the clockwise rotation in wind direction.

These oscillations have the characteristics of a standing wave with an antinode at the shoreline. Water level fluctuations, as well as wave states, wind speed and direction and atmospheric conditions associated with cold front passages force cross-shore mud transport to the mudflats. As the muds are transported, sorting of cohesive and non-cohesive sediments occurs in the wave boundary layer, similar to the turbidity-sorting model of Stow and Bowen (1980) (Fig. 5). Rapid mud deposition occurs when the yield strength of the fluid mud layer supported above the wave boundary layer is equal to the wave boundary layer shear stress (Einstein, 1941; Kemp, 1986). Sudden deposition can then occur through a "freezing" process (Kemp, 1986). These fluid mud deposits can then be transported in the direction of mean flow by a decrease in yield strength of the deposit at the top of the wave boundary layer. The top of this layer marks the separation of the silt particles from the flocculent clay particles in the mixed suspension above the high shear zone. This break in the sediment concentration close to the bed results in decreased yield

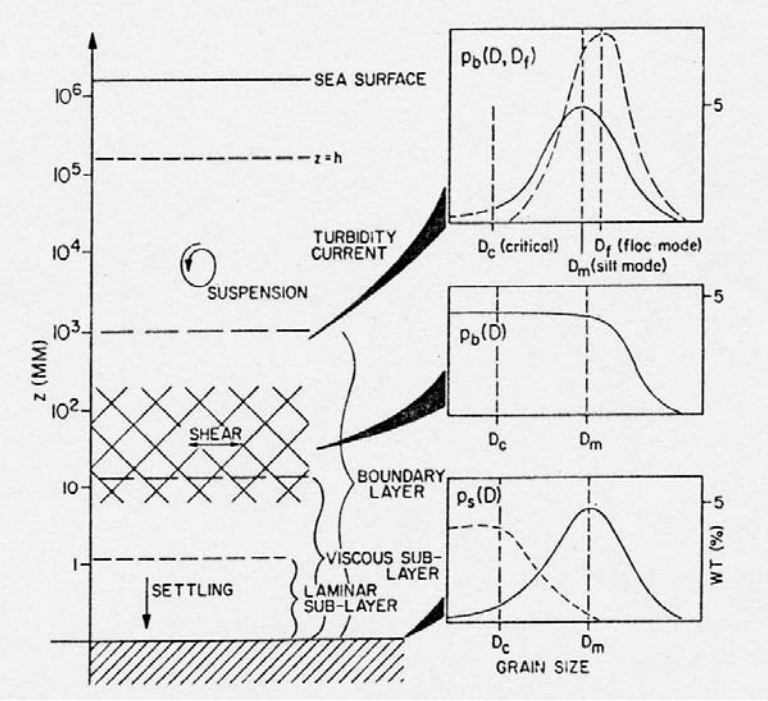

Figure 5. Model for shear sorting of sediments and the distribution of grain sizes in the bottom boundary layer (Stow and Bowen, 1980).

strength at the break. Transport can then occur under the influence of shear at the upper layer, along a shear plane defined by the drop in yield strength at the top of the high shear zone. The onshore decreasing shear stress gradient that develops under attenuating waves causes preferential deposition nearshore, resulting in vertically stacked packages of 2-10 cm thick beds composed of basal silt/shells layers overlain by mud in the mudflat cores (Kemp, 1986).

More recently, Wright et al. (2001) quantitatively described wave-enhanced gravity-driven sediment transport on continental shelves off the Yellow, Eel, and Mississippi Rivers. Their study focused on river sediment that settles and is mixed with seawater by ambient waves and currents before it is transported down-slope due to gravity. While the study environments have very different characteristics, wave-enhanced gravity-driven transport of fine-sediment deposits can occur in all. This process involves the interaction of wave and tidal or wind-driven currents with the gravity forces that act on near-bed turbid layers. Since the gentle slopes of most continental shelves are insufficient to sustain auto-suspending turbidity currents, turbulence by wind or wave currents is necessary to sustain gravity currents on the shelf. The presence of ambient currents enhances gravity currents as long as an unlimited supply of easily suspended sediment exists. With a limited sediment supply, turbulence generated by ambient currents increases bottom drag and lowers the potential rate of gravity induced sediment transport. Wright et al. (2001) indirectly observed wave-generated gravity flows on the south-central Louisiana shelf through bottom boundary layer measurements using an instrumented tripod. A two-phase high turbidity event was observed first during high orbital velocities (13 cm s^{-1}), followed by a pronounced increase in sediment concentration during decreasing orbital velocity. A lutocline, similar to that on the Eel River shelf, was visible from the bottom boundary data. During high orbital velocities, Wright et al. (2001) extrapolated the across-shelf current to the

top of the wave boundary layer, and found an average down-slope velocity of ~0.5 cm s^{-1}. Then under decreasing orbital velocities, the amount of suspended sediment increased to concentrations that could not be explained by local resuspension alone. During this phase, the sediment did not continue to move downslope due to the decreasing ambient currents and increasing thickness of the high-concentration layer. Since the south-central Louisiana shelf is both morphologically and dynamically similar to the western Louisiana shelf, it is likely such gravity flows play an important role in the redistribution of sediments west of the Atchafalaya River (Bentley, 2003).

Study Region

The Chenier Plain coast of western Louisiana extends from Tigre Point in the east to about 16 km west of Freshwater Bayou Canal (Fig. 2). The region is generally classified as a "low energy" environment. It is a shallow (< 10 m deep 25 km offshore), microtidal (40 cm diurnal tides), and low gradient ($\sin \theta \sim 0.001$-0.002) inner shelf. However, from October to April, frontal passages occur on 3-5 day cycles, generating waves that produce significant sediment resuspension. Real-time wave data is available by the LSU Coastal Studies Institute Wave-Current Surge Information System (WAVCIS), on a platform (CSI-3) located within the region of mud deposition on the inner shelf (Fig. 2). Typical winter storms can produce waves exceeding 1.4 m wave height, 5 s period, with an estimated $u_{wb} > 1$ m s^{-1} (Stone and Zhang, 2002). The end of this storm season coincides with the maximum discharge of the Atchafalaya, usually peaking in April. Since prevailing currents in this area are westward, the Chenier coastline is most influenced by the river in the springtime.

METHODS

In order to understand the spatial and temporal distribution of sediment, samples were collected in along- and cross-shore transects of the inner shelf opposite the area of coastline where most progradation is occurring, landward of the 10 m isobath, 100 km west of Atchafalaya Bay. Sampling in March and May 2002 also took place seaward of Southwest Pass, south of the CSI 3 WAVCIS station, in a transect crossing Trinity and Tiger Shoals. March and May 2002 sampling times were designated to coincide with pre- and post-Atchafalaya maximum discharge.

Gravity and box core samples were collected in May 2001, and box cores were collected in March and May 2002. The Atchafalaya River typically experiences its highest discharge in the spring, with a maximum in April. May 2001 sampling occurred after this maximum, and the March and May sampling periods of 2002 were designated to coincide with pre- and post-maximum Atchafalaya River discharge.

Box cores were sub-sampled for X-radiography, radioisotopes, grain size, porosity, and macrofauna content. Slabs for X-radiography were taken by inserting 3-sided Plexiglas trays into the box core then inserting the fourth side to minimize fabric distortion. The trays were sealed with neoprene plugs to prevent slumping and desiccation before they were brought back to the laboratory where they were analyzed using a portable veterinary X-ray machine. The X-rays were digitized for visual analysis of sedimentary structures and macrofauna burrows.

Box cores were additionally sub-sampled with two 10 cm internal diameter PVC pipes. One subcore was sieved for macrofauna (> 0.5 mm) using a 500μm sieve. Any macrofauna were counted and documented onboard ship, but were not preserved. The other subcore was extruded in 2 cm intervals onboard ship for grain size, porosity and radioisotopic analysis in the laboratory. Grain size analysis of wet sediment was conducted using a Micrometrics ET-5100

Sedigraph following standard procedures (Coakley and Syvitski, 1991). The samples were sieved using a 63 μm sieve to separate the coarse fraction then dispersed with a 50% sodium metaphosphate solution prior to analysis.

Beryllium-7 ($t_{1/2}$=53.3 days), ^{210}Pb ($t_{1/2}$ = 22.3 years) and ^{137}Cs ($t_{1/2}$=30.07 years) were used as tracers of sediment accumulation and mixing. Their range in half-lives allows for analysis of processes on both short (~3-5 months) and long (~100 years) time scales.

Beryllium-7 is a cosmogenic radionuclide formed by cosmic ray spallation of nitrogen in the earth's atmosphere. It is delivered to the earth's surface by wet and dry aerosol deposition and adsorbed onto sediments and suspended particles. Beryllium-7 distribution is a function of suspended sediment concentration, river input, and the rate of sediment deposition and biological mixing with respect to radioactive decay. On fluvial influenced coasts where the ratio of drainage basin area to receiving basin is high, the fluvial supply of ^{7}Be is much greater than atmospheric influx, making ^{7}Be an excellent tracer of river discharge (Sommerfield et al., 1999). The presence of ^{7}Be in the sediment also indicates it has been recently deposited (<4 half-lives).

Cesium-137 is the product of nuclear fission in nuclear reactors and bombs and was first released to the atmosphere by bomb testing in 1954, and reached a peak in concentration in 1963. Either the first occurrence of ^{137}Cs or its peak can be used as a time marker in sediments to estimate the average accumulation rate of the study area. Since minimal bioturbation occurs in this region, we are assuming bioturbation did not have a significant effect on the ^{137}Cs penetration depth.

Lead-210 is a naturally occurring product of the ^{238}U decay series. It has several sources in the marine environment, including delivery by fluvial discharge, atmospheric deposition from ^{222}Rn decay, and production from ^{226}Ra in both the water column and in sediments. Supported

^{210}Pb is that fraction produced *in situ* by decay of ^{226}Ra in the sediment column. Excess (unsupported) ^{210}Pb is the amount of ^{210}Pb present in fluvial sediment, plus that which is adsorbed from seawater by the sediment. It is determined by subtracting supported ^{210}Pb from total ^{210}Pb present in the sample and decay-corrected to the time of sample collection (Goldberg, 1963; Appleby and Oldfield, 1978).

The activities of ^{7}Be, ^{137}Cs, and ^{210}Pb were determined by gamma spectrometry of dried sediment (477.7 keV peak for ^{7}Be and 661 keV peak for ^{137}Cs). The sediment was homogenized and weighed before and after drying for water content to be used in porosity calculations. A known mass of ground sediment was then placed in a 6 cm petri dish and sealed with hot glue. After a 3 week waiting period to allow for ^{222}Rn and ^{226}Ra to grow into equilibrium with ^{210}Pb, the sealed samples were analyzed on a Canberra planar-style low-energy intrinsic germanium detector for 24 hours. Excess ^{210}Pb was calculated by subtracting supported ^{210}Pb (which are measured by averaging the net counts of ^{214}Pb ($t_{1/2}$ = 26.8 min; 295.2 keV and 352 keV peaks) and ^{214}Bi ($t_{1/2}$ = 19.7 min; 609 keV peak), intermediate daughter products between ^{222}Rn and ^{210}Pb assumed to be in secular equilibrium with ^{210}Pb) from total ^{210}Pb (46.5 keV peak). Samples were corrected for self-absorption using a high-activity sealed standard following the methods of Cutshall et al. (1983). Beryllium-7 detection limits, calculated as 3x the counting error of a blank sample, were determined to be approximately 0.3 dpm g^{-1}. The minimum detection limits for ^{137}Cs were about 0.05 dpm g^{-1}.

Lead-210 activities were also determined for select gravity core samples by extracting its granddaughter, ^{210}Po ($t_{1/2}$ = 138 d), from the sediments by partial acid digestion. Approximately 5g of dried and ground sediment was spiked with 1.0 ml ^{209}Po as a tracer, first leached with HNO_3 to remove organics, then HCl solution to extract the polonium from the sediment. Silver

planchets were then placed in the polonium/acid solution for ~24 hours to allow electro-deposition of the polonium onto the planchets. The planchets were analyzed for 24 hours on a Canberra alpha detector (Nittrouer, 1979). Lead-210 activity was calculated by assuming secular equilibrium with ^{210}Po and excess ^{210}Pb activity was determined by comparison with values at the base of each core.

Accumulation rates (S) were calculated from excess ^{210}Pb profiles, using a steady-state solution to the advection-decay equation, assuming a log-linear relationship between activity and depth (assuming negligible bioturbation):

$$S = \frac{-\lambda z}{\ln \frac{A_z}{A_0}} \quad \text{.....(1)}$$

where λ is the decay constant ($0.693/t_{1/2}$); z is depth in seabed (cm); A_o is excess activity at the surface (dpm g^{-1}); and A_z is excess activity at depth z (dpm g^{-1}) (Nittrouer et al., 1984; Bentley and Nittrouer, 1999).

The ^{7}Be inventory for the box cores was calculated from sediment-depth profiles using the following equation:

$$I = \sum \rho_s X_i (1 - \phi_i) A_i \quad \text{.....(2)}$$

where I is the sediment inventory of ^{7}Be (dpm cm^{-2}), ρ_s is the mineral density (2.6 g cm^{-3}), X is the thickness (cm) of the sampling interval I, ϕ is the porosity, and A is the activity (dpm g^{-1}) of the sampling interval. The inventories are summed over continuous sediment intervals, each 2 cm thick (Canuel et al., 1990; Sommerfield et al., 1999).

Gravity cores were analyzed using a GEOTEK Multi Sensor Core Logger (MSCL), which measures the bulk density profile of the cores by gamma-attenuation, with a narrow beam of gamma rays emitted from a 10 millicurie ^{137}Cs source. After analysis on the MSCL, the cores

were split so one half could be subsampled with small Plexiglas boxes for X-radiography and the other half subsampled in 2 cm intervals for grain size, porosity and radioisotopes, as previously described. Analyses of X-radiographs and subsamples were conducted using procedures described above for the box cores samples.

RESULTS

Atchafalaya River Discharge

In 2001, sampling occurred at the end of peak Atchafalaya River discharge, after the river discharged a total of $1.1x10^5$ m^3 s^{-1} of water (Fig. 6). The following year, as described in Chapter 2, the timing for the March and May 2002 sampling trips was designed to coincide with pre- and post-Atchafalaya peak discharge. Instead, the river experienced multiple discharge peaks of shorter duration, with sampling occurring before and after the third peak. By the time of May sampling, $13.6x10^5$ m^3 s^{-1} had been discharged by the river. Although this discharge is much higher than the previous year, it was not discharged at one time, with $8.2x10^5$ m^3 s^{-1} being discharged before the March sampling as two peaks (November-March), and an additional $5.5x10^5$ m^3 s^{-1} before sampling occurred in May.

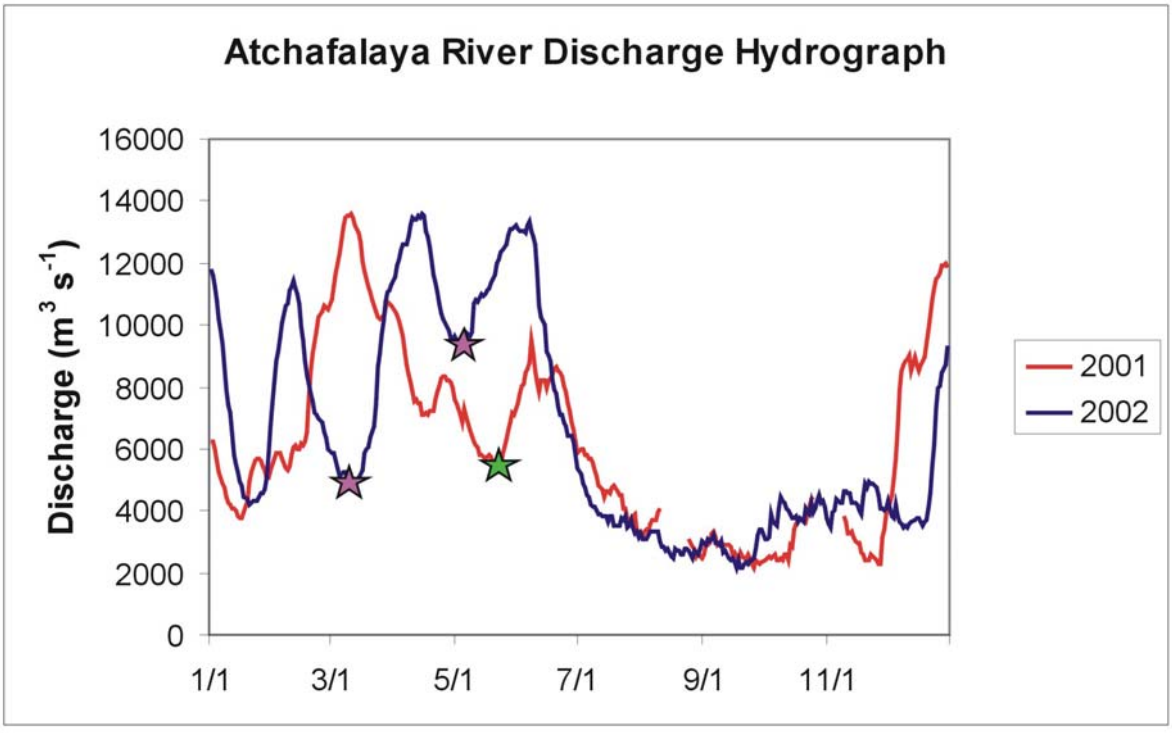

Figure 6. Atchafalaya River hydrograph for 2001 and 2002, measured at Simmesport, LA (USACE). The stars denote sampling periods.

May 2001

Sedimentary Facies

In May 2001, samples were collected from the region west of Freshwater Bayou (FWB) Canal (Fig. 7). The boxcores obtained displayed a continuous gradient from muddy water to watery mud instead of an obvious sediment-water interface. The surface sediment was yellowish brown, with a yogurt-like consistency. Surface porosities range from 87-95% and decrease to ~80% near the bottom of each boxcore sample (Figs. 8-13). Visual examination showed that the sediment became more consolidated downcore and was darker brown.

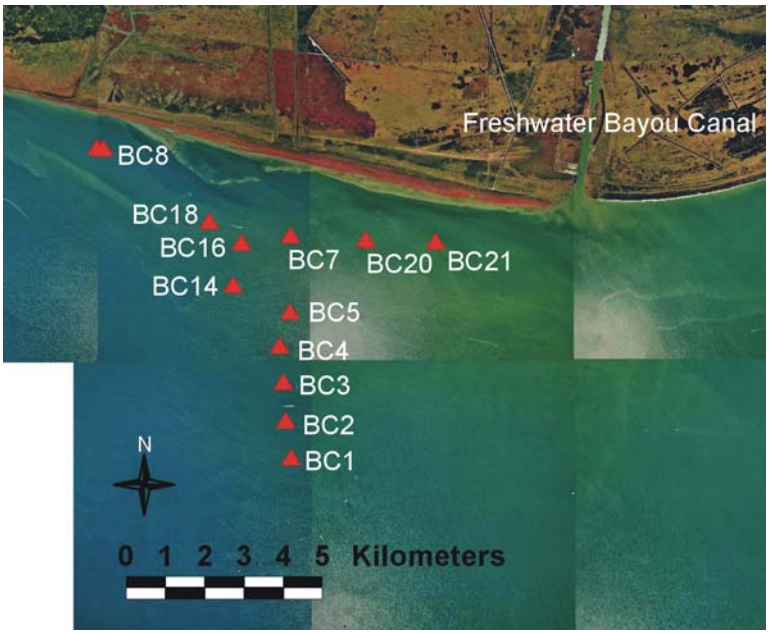

Figure 7. Location map of AC0501 boxcores collected in May 2001.

Examination of the surficial sediment showed no evidence of macrofauna activity, and the subcores from all sampling sites contained no macrofauna. X-radiographs show low-bulk-density sediments as dark regions and high-bulk-density sediments as bright regions. The X-radiographs show a mud layer 10-25 cm thick overlying multiple silty layers in each core (Figs. 8-12). Below this first silty "event" layer, most cores consist of packages of mud with multiple

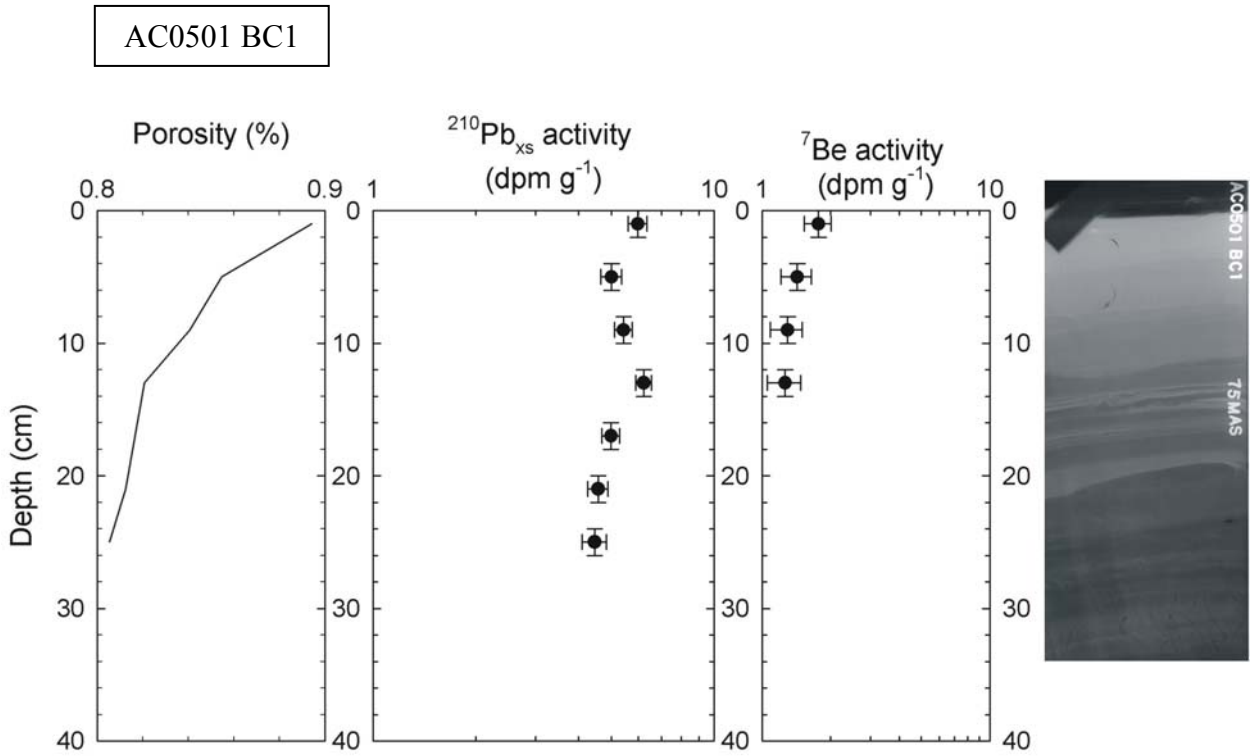

Figure 8. Porosity, $^{210}Pb_{xs}$ activity, ^{7}Be activity, and X-radiograph for site BC1.

AC0501 BC4

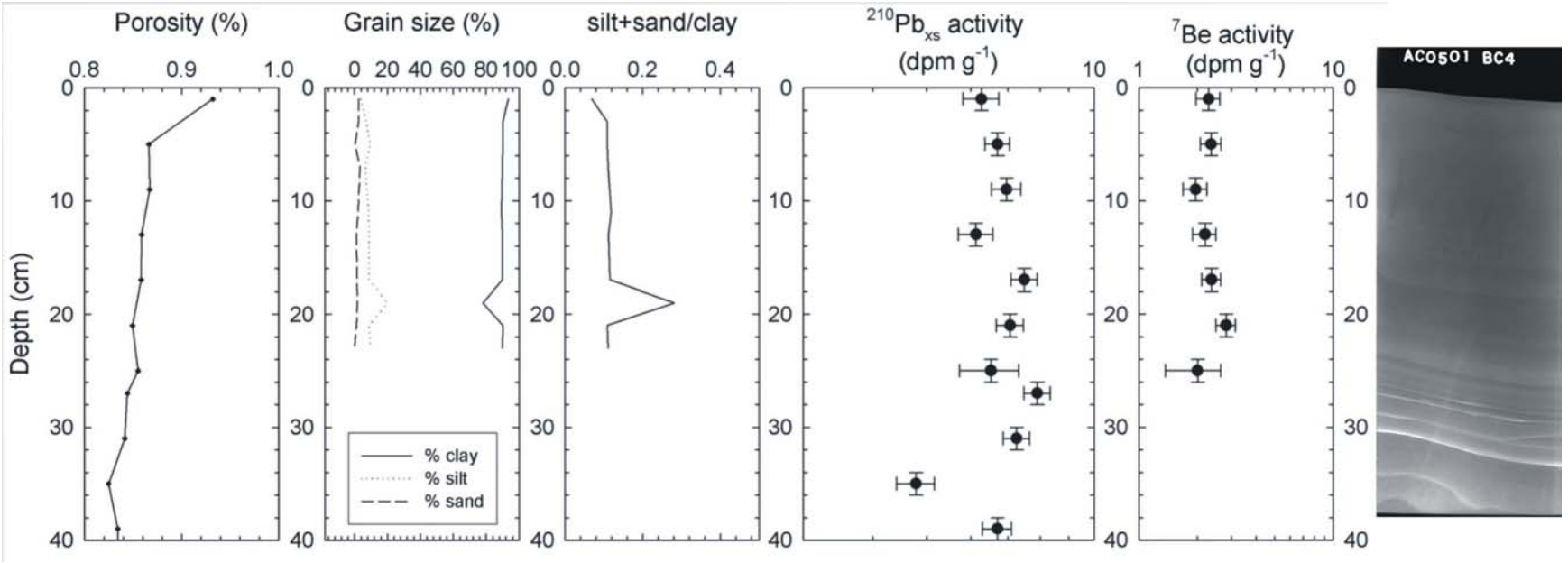

Figure 9. Porosity, grain size, silt+sand/clay ratio, $^{210}Pb_{xs}$ activity, ^{7}Be activity, and X-radiograph for core BC4

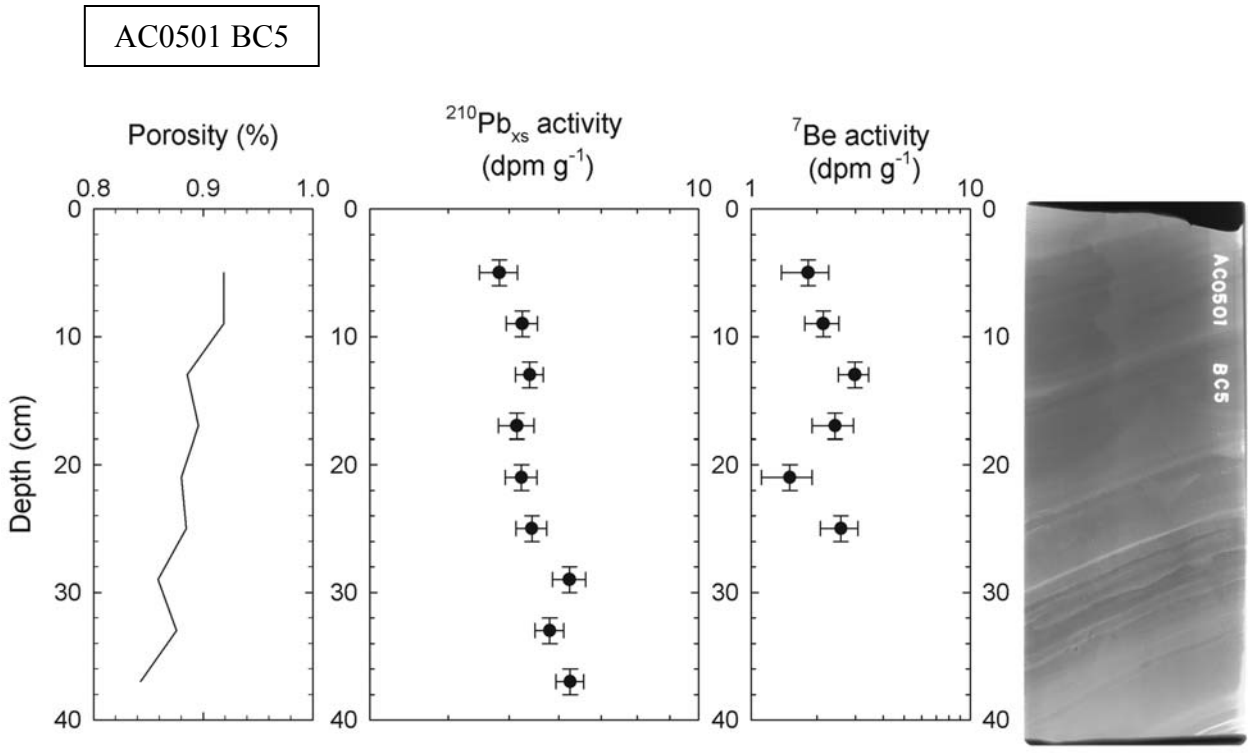

Figure 10. Porosity, ^{210}Pb activity, ^{7}Be activity and X-radiograph for core BC5.

AC0501 BC8

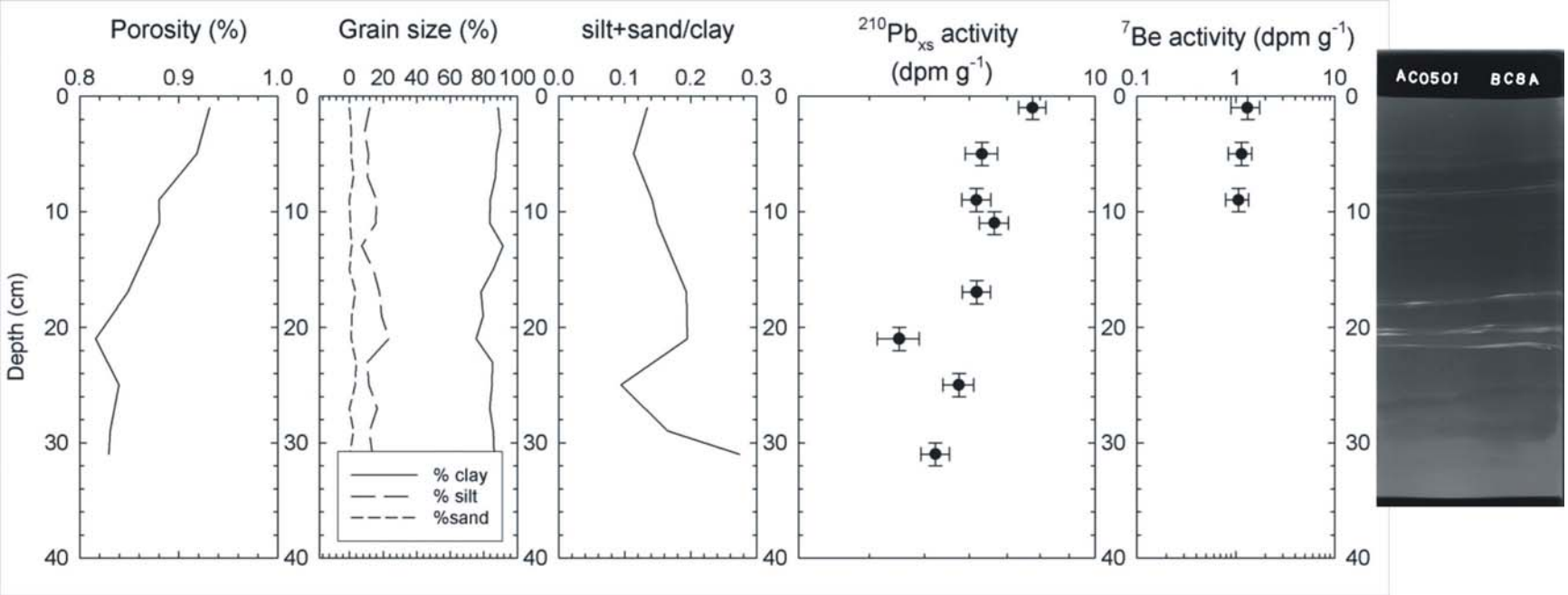

Figure 11. Porosity, grain size, silt+sand/clay ratio, $^{210}Pb_{xs}$ activity, ^{7}Be activity, and X-radiograph for core BC8

AC0501 BC14

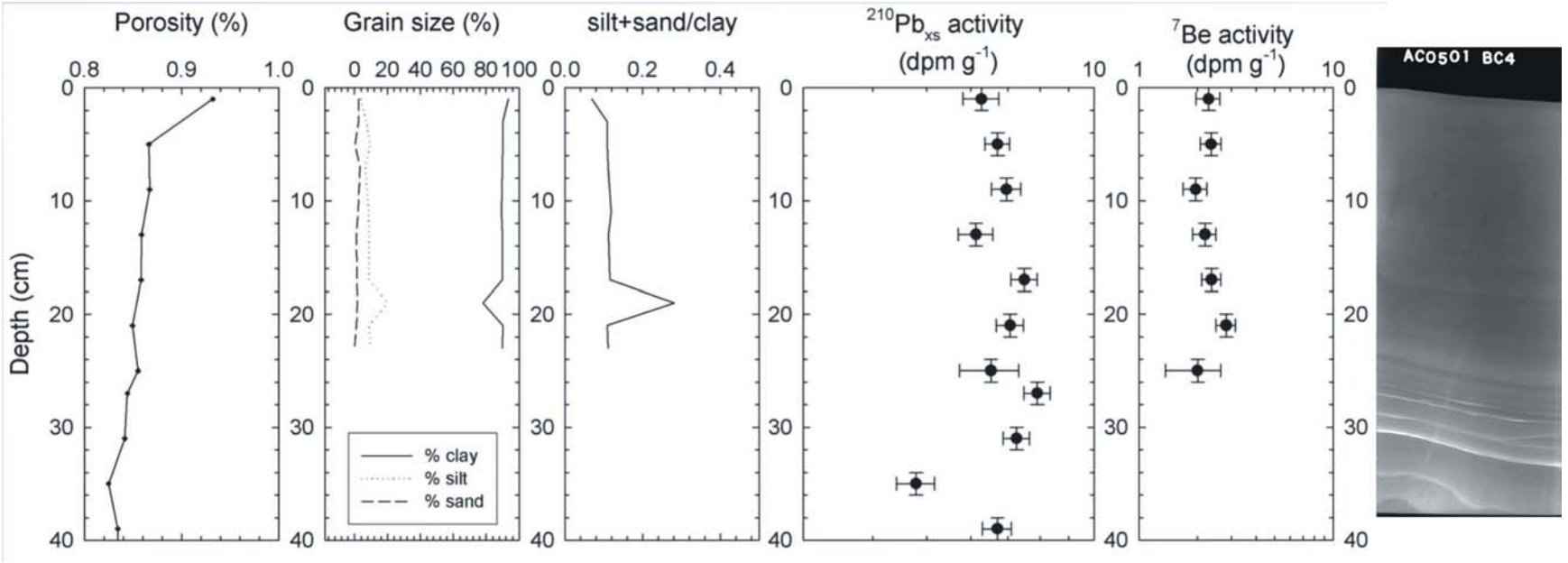

Figure 12. Porosity, grain size, silt+sand/clay ratio, $^{210}Pb_{xs}$ activity, ^{7}Be activity, and X-radiograph for core BC14

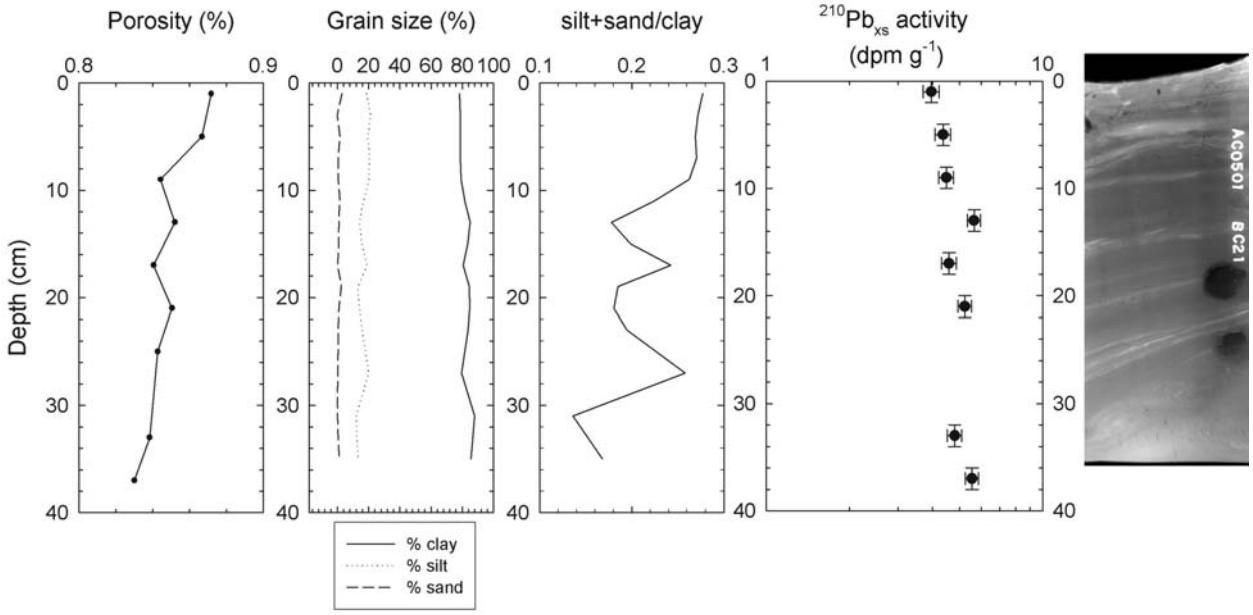

Figure 13. Porosity, grain size, silt+sand/clay ratio, $^{210}Pb_{xs}$ activity, and X-radiograph for core BC21.

basal silt layers. Primary physical stratification is evident in the X-radiographs, with nearly horizontal bedding and little to no visible bioturbation. While the thickness of the surface mud/silt couplets may range up to 25 cm, downcore these packages are typically 2-6 cm thick. Grain size analysis of cores BC4, BC8, BC14 and BC21 (Figs. 9,11-13) confirm that low density sediments visible in the X-radiographs are clay rich, and higher-density layers may contain up to ~15% of silt with very little (<4%) sand. Variations in grain size are particularly evident by the ratio of coarse (silt+sand) to fine sediment, with peaks in the ratio values representing coarser layers within the clay rich cores. These silty layers do not appear laterally continuous between sites, which are 1-2 km apart. The boundary between the silt layers and the underlying beds appears sharp, though the upper bound ranges from sharp to gradational into the overlying mud. Evidence of erosional contacts exists in most cores, such as crosscutting of underlying layers (e.g. BC1, BC16; Figs. 8, 14E), irregular contacts (e.g. BC2, BC3, BC5; Figs. 14A, 14B, 10),

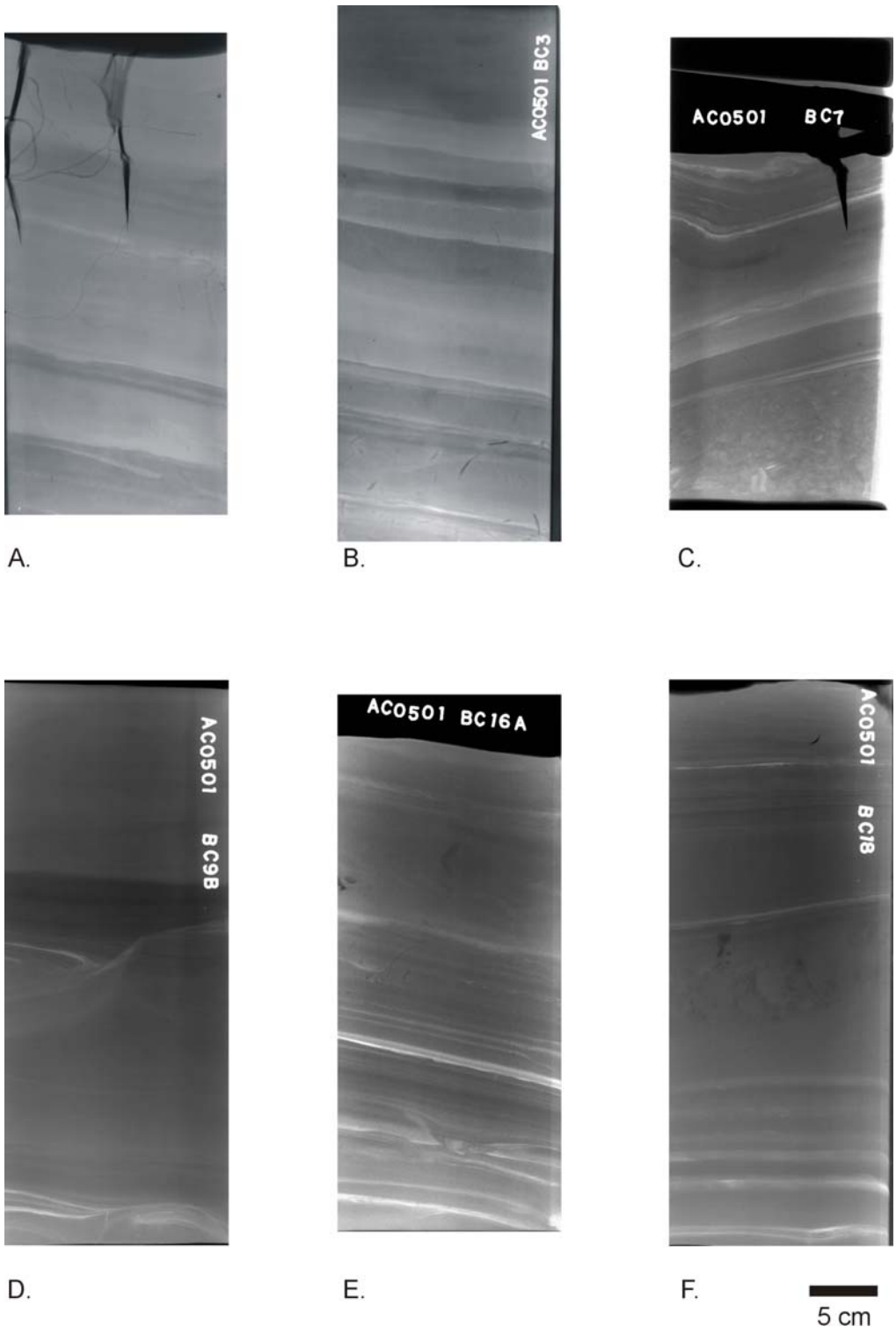

Figure 14. X-radiographs for cores (A) AC0501 BC2; (B) AC0501 BC3; (C) AC0501 BC7; (D) AC0501 BC9; (E) AC0501 BC 16; (F) AC0501 BC18.

and non-parallel layers (*e.g.* BC4, BC7, BC14, BC18; Figs. 9, 14C, 12, 14F). Convoluted or rippled silt layers are also evident in some cores. For example, core BC1 (Fig. 8), between 13 and 24 cm, has two packages of mm-thick silt/mud laminae, some convoluted silt layers, with sharp upper and lower bounds.

Radioisotopic Analysis

Profiles of ^{7}Be activity show relatively high (1.3 – 2.5 dpm g^{-1}) and uniform activities (Figs. 8-12), becoming undetectable at depths of 10-26 cm. Since the profiles do not exhibit logarithmic decay with depth, accumulation rates were not determined using the advection-decay equation. It is assumed that the depth to which ^{7}Be penetrates is the amount of sediment deposited within the past few months (< 2 half-life). The maximum depth of ^{7}Be penetration is generally coincident with the depth of the first significant silty layer visible in the X-radiographs.

Activities of ^{7}Be were below detection in core BC21 (Fig. 13), which was collected from the easternmost station in this survey. The BC21 X-radiograph showed coarser material at the seabed, and grain size analysis confirmed that this core contained more silt and less clay (~ 20% and 80%, respectively) than the other core sites. Regional ^{7}Be inventories range from 1.6-10.8 dpm cm^{-2} (Fig. 15) with the maximum located in a depocenter around site BC4, about 6 km southwest of FWB canal outlet. Measurements of excess ^{210}Pb activities show subsurface maxima near the base of the ^{7}Be-laden layer (Figs. 8-12).

Geoacoustic Surveys

Geoacoustic surveys (Fig. 16) were conducted in May 2001 using both chirp and sidescan sonar (Roberts et al., 2002). These surveys confirm the presence of a depocenter, landward of the 5 m isobath, 95-110 km west of the mouth of the Atchafalaya River. The depocenter appears in the sidescan mosaics (Figs. 16 and 17) and chirp subbottom profiles (Figs. 16 and 18) as a

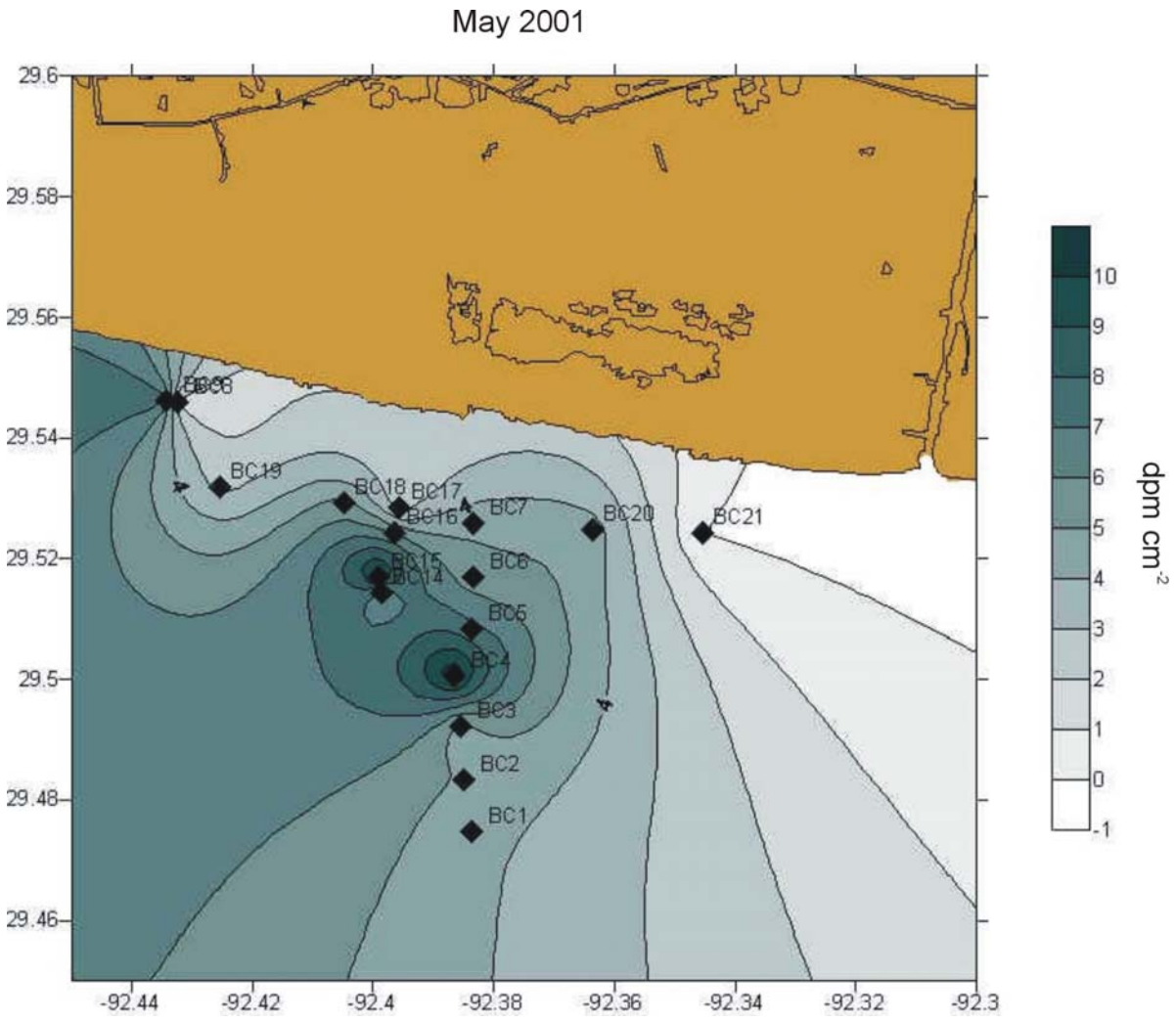

Figure 15. Map of ^{7}Be inventory in dpm cm^{-2} of study area in May 2001. See Figure 7 for locations with reference to Freshwater Bayou Canal. The diamonds represent the sampling sites. The maximum inventory is 10.8 dpm cm^{-2}.

sediment lobe with ~1 m relief above the surrounding seafloor extending seaward from the shoreface and ending in a region characterized by an irregular reflector overlain by acoustically transparent sediment in water depths ~2 m. Sidescan mosaics (Fig. 18, Line A) nearshore in water < 1 m deep show a smooth, featureless seabed, while further offshore (Fig. 18, Line B, Line C west and Line C east), the seaward edge of the lobe has irregular scalloped edges and troughs, which are filled with acoustically transparent sediment (Roberts et al., 2002; Bentley et al., 2003). The seabed slope is ~0.75 m/km over ~3 km.

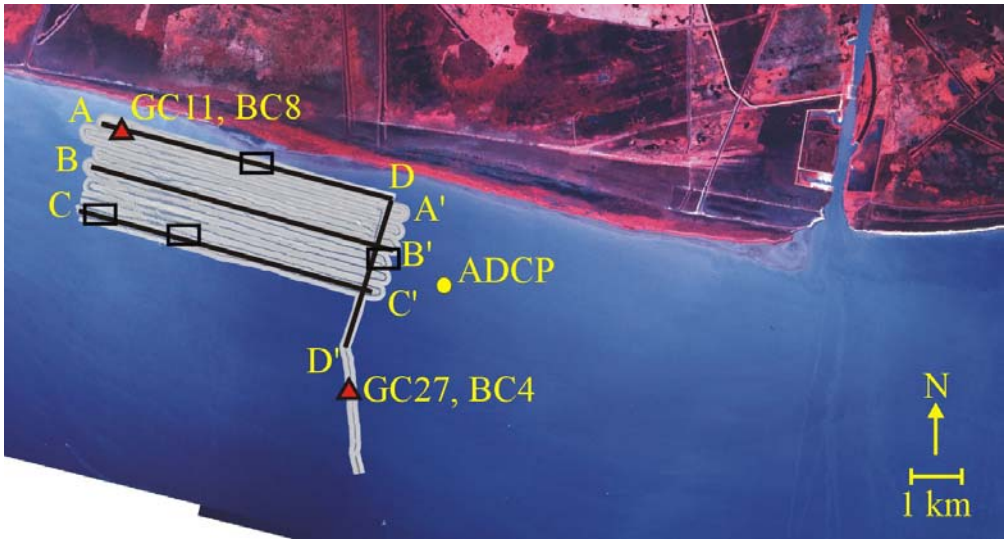

Figure 16. Infrared false-color image of the study area, taken by NASA remote sensing aircraft, showing the location of Freshwater Bayou (FWB) canal, ADCP location (circle), chirp survey lines, and sidescan mosaics (black boxes).

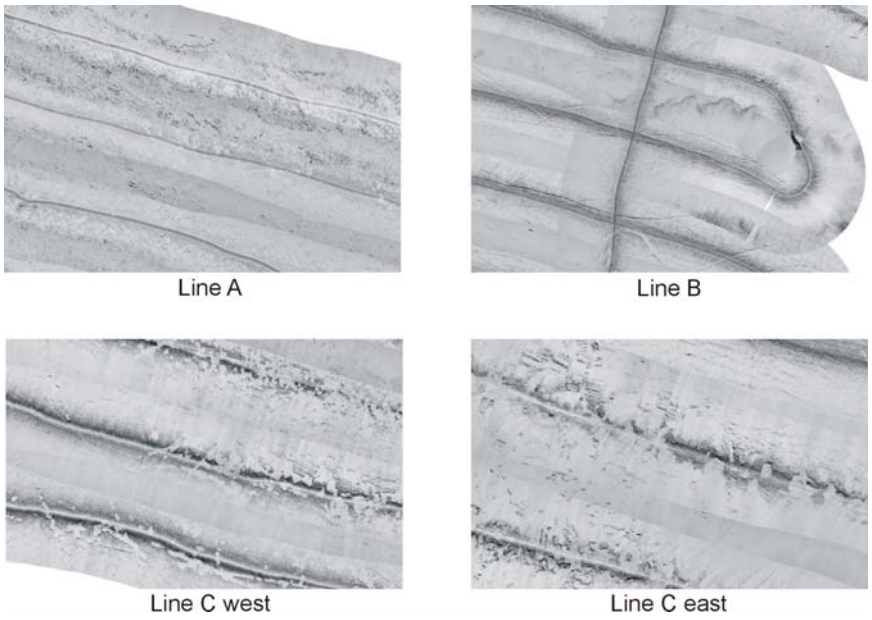

Figure 17. 690 m by 465 m sidescan mosaics. The line A mosaic shows the smooth, featureless seabed along the line furthest inshore. The mosaics from Lines B and C along the seaward edge of the depositional lobe have irregular scalloped edges, as well as areas of ponded acoustically transparent sediment in troughs cut into highly reflective sediment. The location of all mosaics is shown as black boxes in Figure 16.

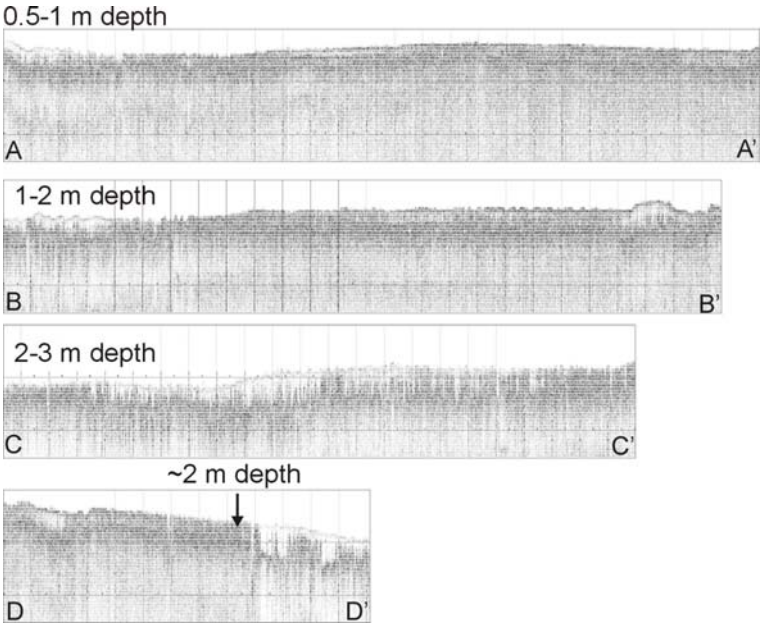

Figure 18. Chirp sonar profiles (A-C shore parallel, D shore normal). The landward most profile (A-A') has a smooth surface. Seaward, the profiles show increasingly irregular reflective sediment with acoustically transparent sediment deposited on top (B-B', C-C', D-D'). Line A-A' is 6.1 km long; the profiles are 5 m tall, with gridlines at 2 and 4 m bsf. Location of profiles shown in Figure 16.

Wind and Wave Data

Wind data from CSI 3 ocean observation station recorded two separate cold front passages through the study region during May 20-25, simultaneous with ADCP deployment. The cold fronts are recognized by shifts in wind direction from strong southerly winds to northerly winds and back to southerly winds (Fig. 19A). Wave heights peaked during southerly winds (due to longer fetch) (Fig. 19B) but current speeds were similar for both eastward and westward flow (Figs. 19D and 19F). Backscatter measurements from the ADCP (Fig. 19G) show changes in signal strength as related to suspended sediment concentration. Exact concentrations are unknown but at least three periods of high-suspended sediment concentration (ssc) are recorded in the bottom boundary layer during the deployment period in May 2001. The first high ssc period occurred during net southward and eastward flow in the bottom boundary

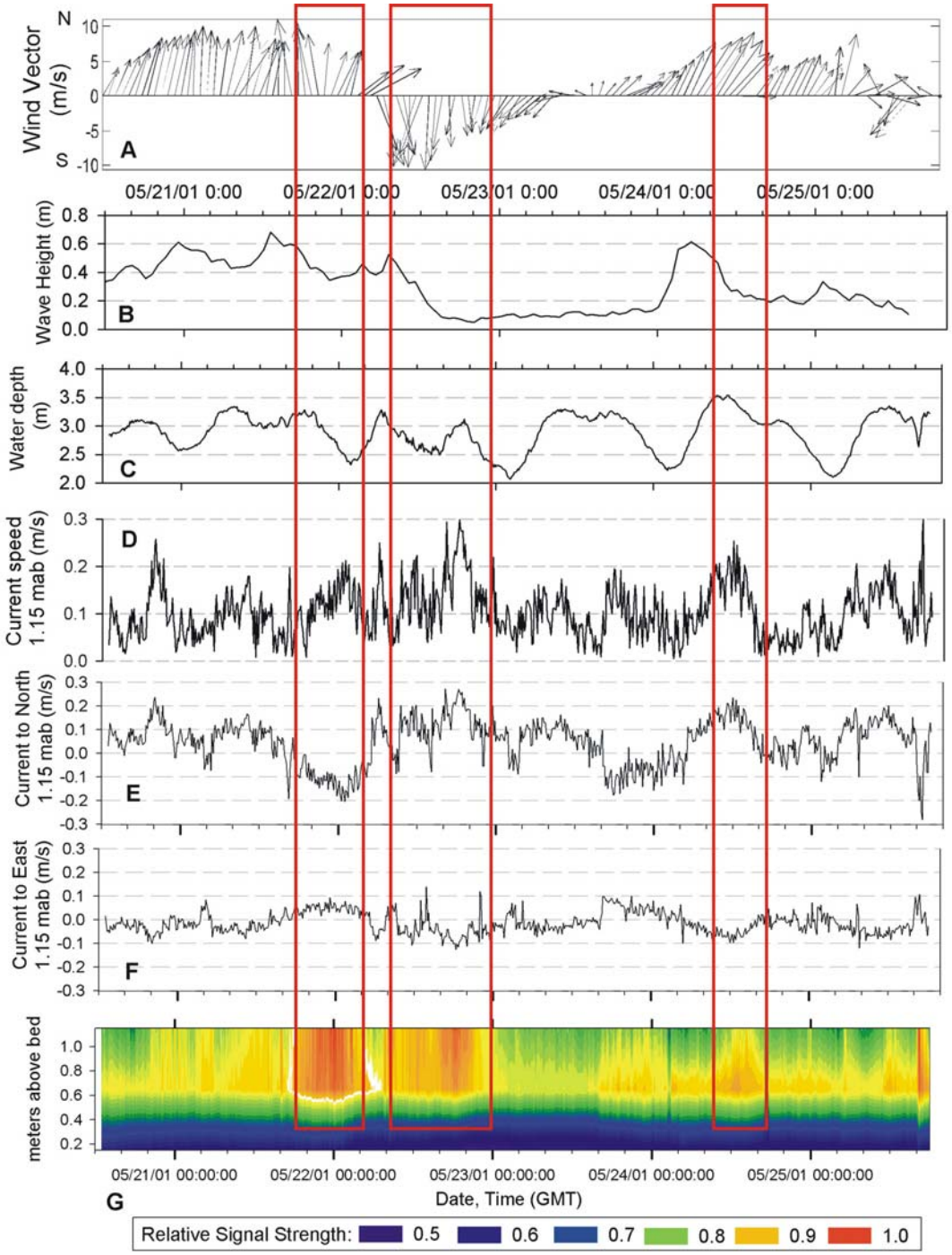

Figure 19. Dynamical data collected from WAVCIS station CSI-3 and ADCP deployment. See Figures 2 and 16 for instrument locations. (A) Wind vectors from CSI-3; (B) Wave height from CSI-3; (C) Water depth at ADCP location; (D) Current speed at 1.15 m above the seabed from ADCP; (E) Current speeds to the north, from ADCP; (F) Current speeds to the east, from ADCP; (G) Relative backscatter signal strength of the lower meter of the water column; Higher signal indicates a higher suspended sediment concentration. The periods of high-suspended sediment concentration outlined with the red box are discussed within the text.

layer, coincident with southerly winds recorded by the CSI 3 WAVCIS station, thus marking the beginning of a cold front passage. The second two high concentration periods are coincident with periods of both net northward and westward flow in the bottom boundary layer. The second high ssc period occurs during northerly winds associated with the passage of a cold front. The third high ssc period occurs during strong southerly winds, and represents the beginning of another cold front passage. All high ssc events occur during periods of relaxing wave heights, a characteristic similar to what has been observed on the eastern Louisiana shelf by Wright et al. (2001), as well as the Amazon (Kineke et al., 1996) and Eel (Traykovski et al., 2000) shelves.

Sediment samples were collected to determine the total suspended load over a three-day period during the passage of a cold front (N. Walker and S. Welsh, unpublished data). The samples were collected within the same time frame as the ADCP and WAVCIS hydrodynamic data discussed above. On May 20th 2001, during southerly winds, the average secchi depths were 169 cm (σ = 105.4, n = 13) and ssc were 16 mg l^{-1} (σ = 27.8, n = 14), although most sites were located further offshore from the study region. On May 21 and 22, sampling sites were located proximal to the coastline in the study region. On May 21st, under higher wind speeds but still southerly winds (speed ~ 17 knots), the average secchi depth was 20 cm (σ = 10.6, n = 18) and ssc was 132 mg l^{-1}(σ = 65.2, n = 18), with a maximum of 265 mg l^{-1} (Fig. 20). On May 22nd, the wind direction shifted to northerly winds with the passage of the cold front. Average wind speed was ~20 knots. The average secchi depth during this time was 12 cm (σ = 8.3, n = 27), with an ssc of 350 mg l^{-1}(σ = 292.7, n = 27). The maximum ssc was 1225 mg l^{-1}, which occurred inshore near site BC20 (Fig. 20). Though the highest suspended sediment concentration was located inshore, the percent increase of ssc during the passage of the cold front was higher further offshore near the depocenter region (Fig. 21).

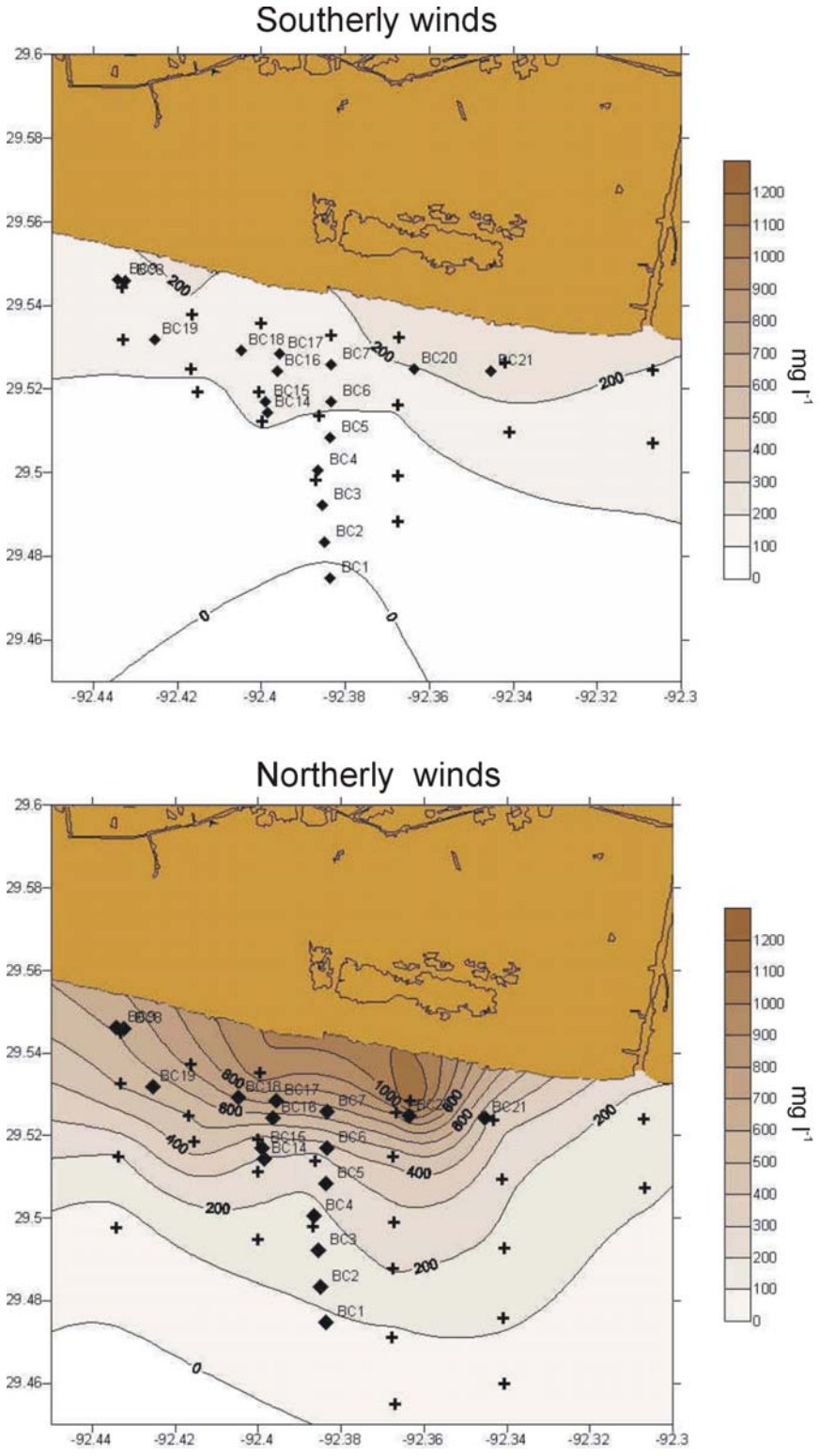

Figure 20. Contour maps showing the suspended sediment concentration (ssc) in mg l^{-1} of the study region during strong southerly winds just prior to a cold front and during northerly winds during the passage of the front. The diamonds represent core locations previously described. The plus (+) signs mark the location of ssc samples.

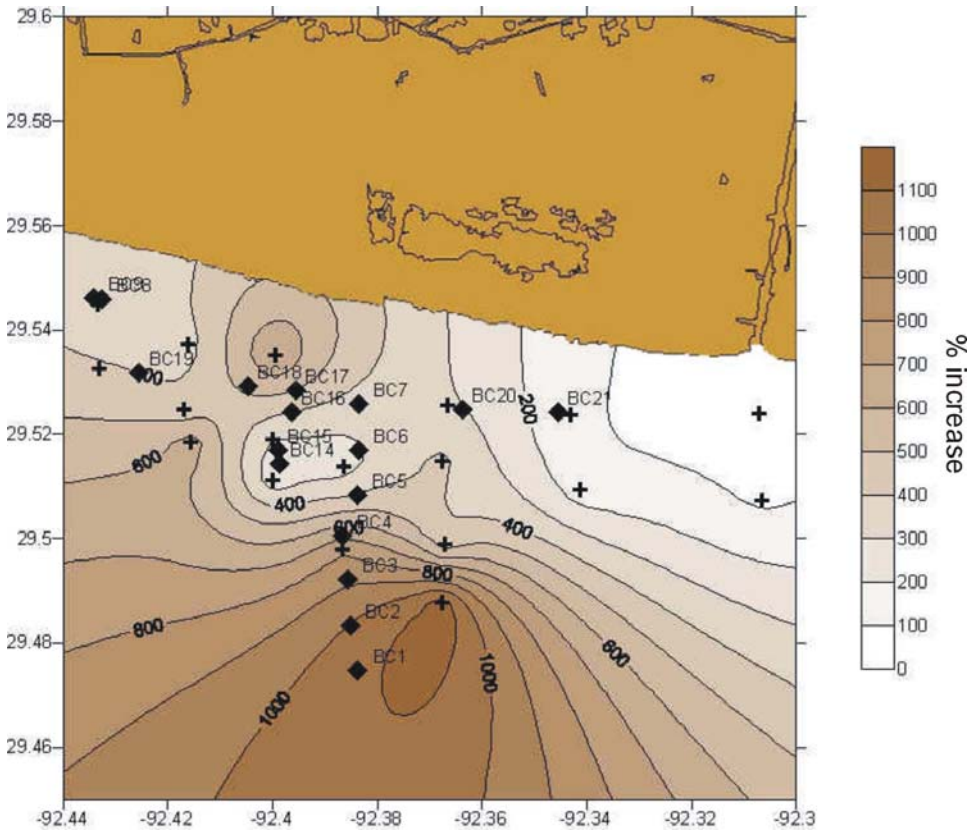

Figure 21. Contour map showing the percentage by which ssc increases during the cold front passage.

Gravity Cores – Sedimentary Facies and Accumulation Rates

Gravity cores (Fig. 22) were collected to show a longer-term time scale of depositional processes. Visual inspections of split gravity cores did not reveal any obvious features other than the downcore increase in sediment consolidation. Analyses conducted using the multi-sensor core logger show the cores consist of alternating zones of relatively low bulk density sediment interlayered with thin beds of higher density sediment, suggesting a series of stacked depositional units of low density muds, each basally bound by thin layer of higher density coarser sediment (Figs. 23-26). X-radiographs of the gravity cores confirm these depositional units, as do grain size analyses, which show that the high bulk density layers consist of mud with higher concentration of silts, and the low bulk density sediments are predominantly mud.

Gamma density logs for all cores indicate an increase in grain size at ~100 cm depth, also evident in the X-radiographs by the increased presence of bright, higher-density layers downcore (Figs. 23-26).

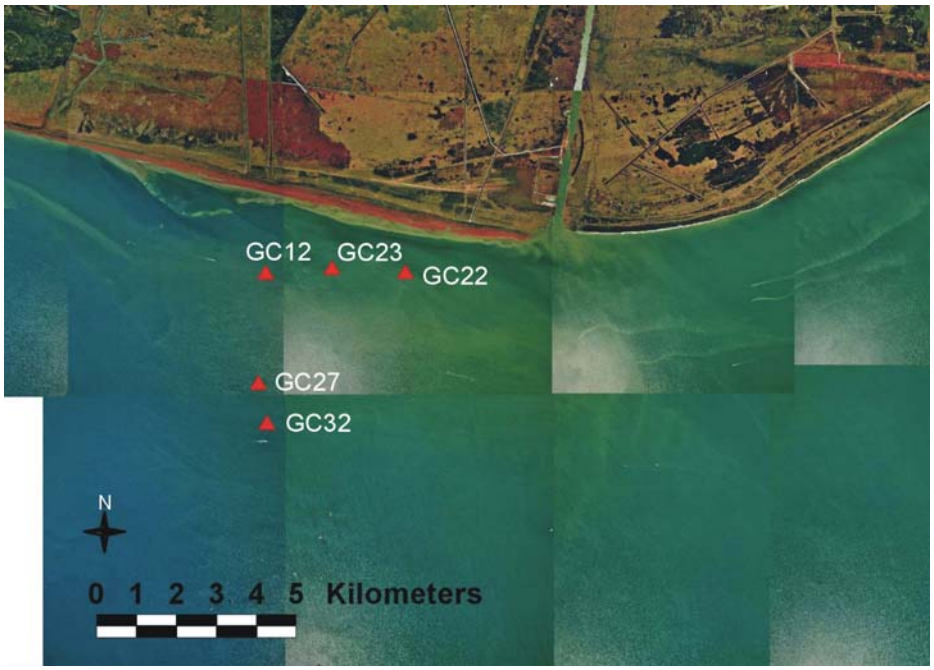

Figure 22. Location map of gravity core sites, collected in May 2001.

Accumulation rates of the gravity cores were determined using ^{137}Cs on cores GC12, GC22, GC23 (inshore), GC27, GC32 (offshore) (Figs. 22, 23-26; Table 1). Detectable ^{137}Cs penetrated to the bottom of all but one gravity core, so only minimum accumulation rates could be determined at most sites. Minimum accumulation rates determined using 1954 (the first anthropogenic introduction of ^{137}Cs into the atmosphere) as a time marker range from 3.2-4.1 cm y^{-1}. The ^{137}Cs profile of gravity core GC23 was the only core to show a subsurface maximum near the bottom of the core (Fig. 25). This peak represents the ^{137}Cs maxima in the atmosphere that has been dated to 1963. Using this peak as a time marker, the accumulation rate at this site is 3.8 cm y^{-1}. At site GC22, ^{137}Cs penetrated to 178 cm, establishing an accumulation rate of 3.6 cm y^{-1} at this site.

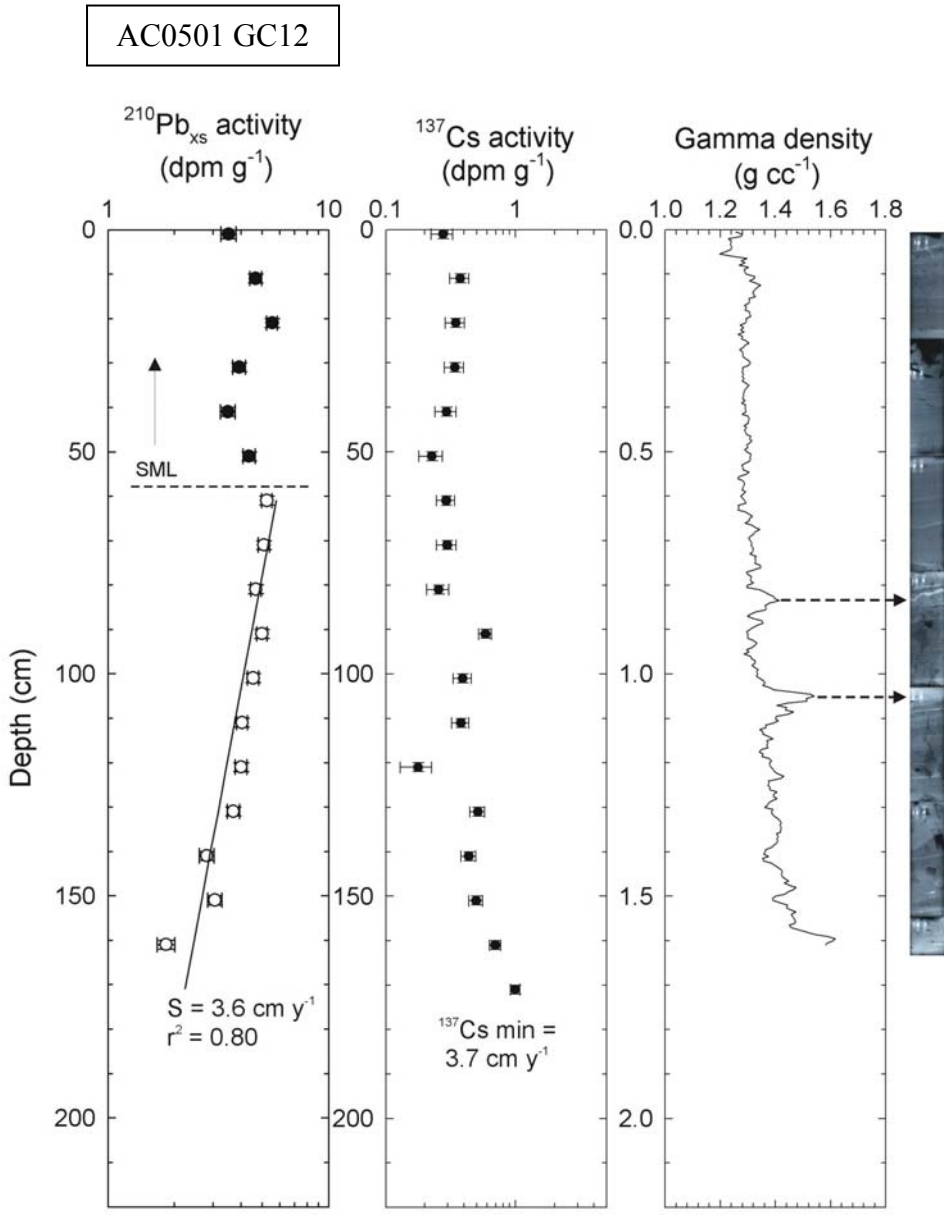

Figure 23. Excess Pb-210 activity, ^{137}Cs activity, gamma density, and X-radiograph for gravity core GC12.

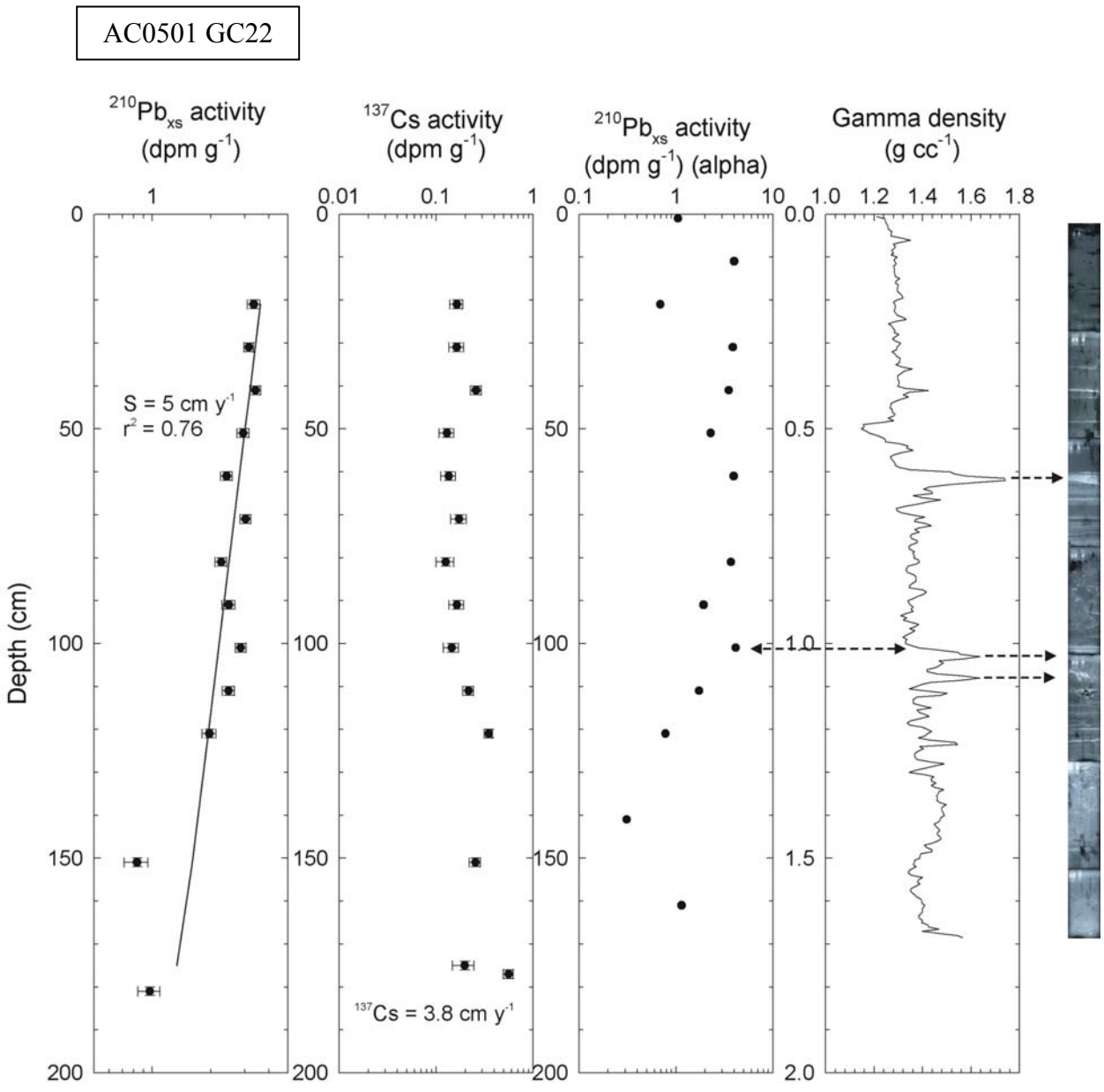

Figure 24. Excess Pb-210 activity, ^{137}Cs activity, gamma density, and X-radiograph for gravity core GC22.

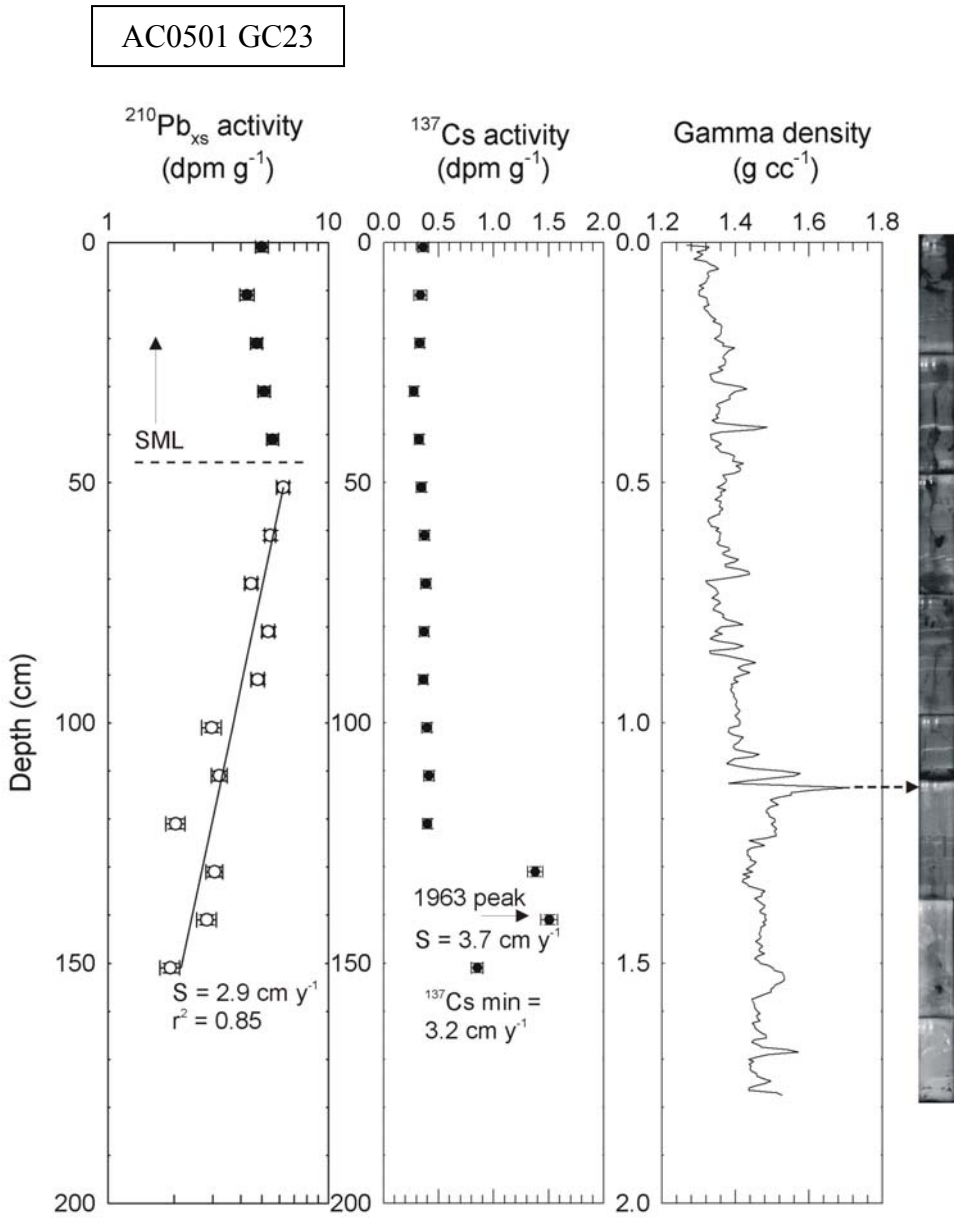

Figure 25. Excess Pb-210 activity, ^{137}Cs activity, gamma density, and X-radiograph for gravity core GC23.

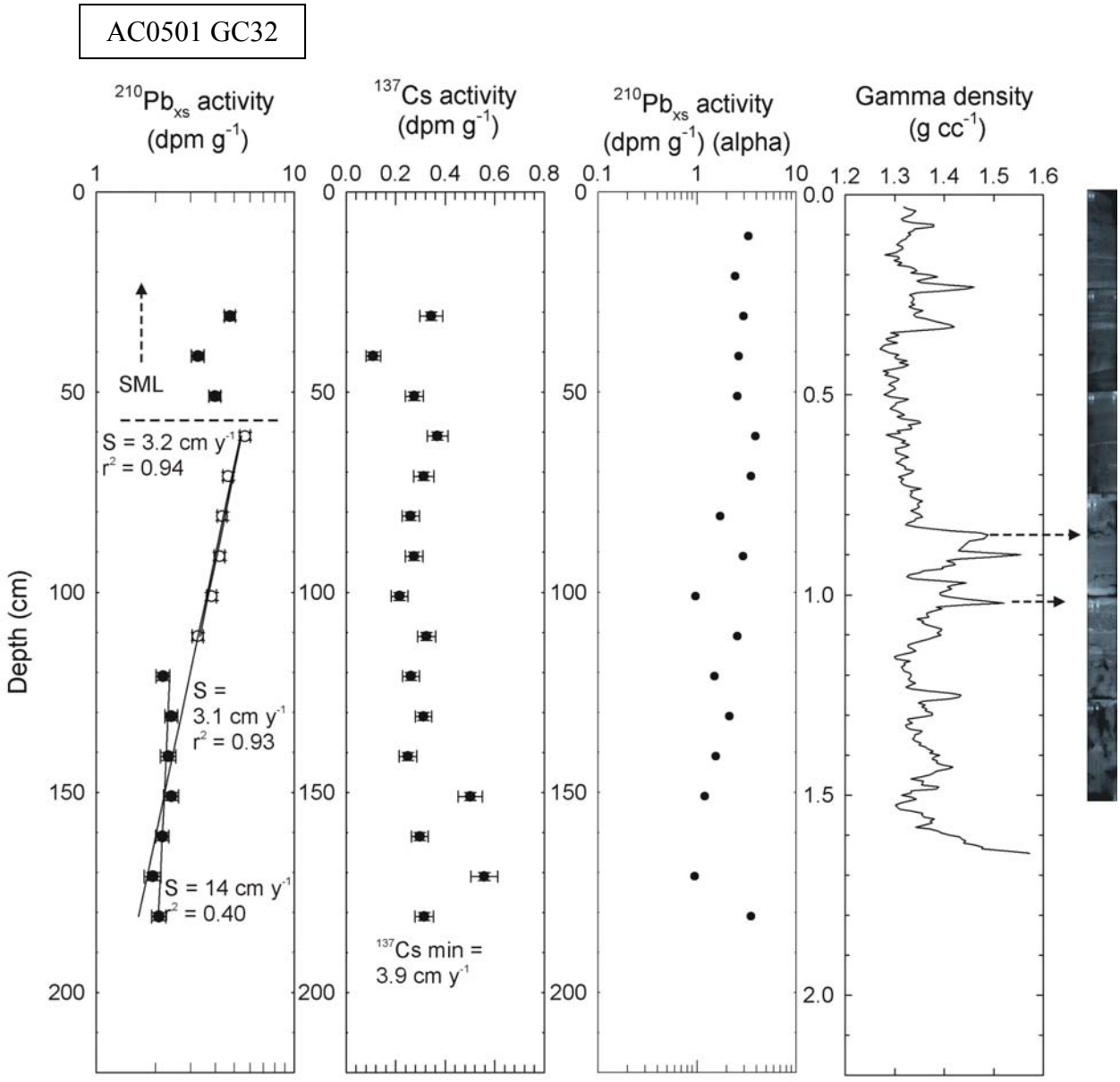

Figure 26. Excess Pb-210 activity (gamma detection), ^{137}Cs activity, $^{210}Pb_{xs}$ activity (alpha detection), gamma density, and X-radiograph for gravity core GC32.

Table 1. Gravity core accumulation rates

Gravity core	$^{210}Pb_{xs}$ (gamma)[1]	$^{210}Pb_{xs}$ (alpha)[2]	^{137}Cs[3]	Corresponding Boxcore	^{7}Be penetration depth (cm)
12	3.6	X	3.7	BC7	18
22	5	2.2	3.8	BC21	0
23	2.9	X	3.2	BC20	18
27	X	5.1	4.1	BC4	26
32	3.1, 3.2 (U), 14 (L)	4.3	3.9	BC1	14

[1]Accumulation rates determined by linear regression, as described in Chapter 2.
[2]Accumulation rates determined by substitution into the Advection-decay equation (Eq.1).
[3]Accumulation rates determined using 1953 as a time marker, as described in Chapter 2.

Accumulation rates determined by gamma analysis of $^{210}Pb_{xs}$ ($t_{1/2}$ = 22.3 y) show a surface "mixed layer" present to ~ 50-60 cm below sea floor (bsf) in gravity cores GC12, GC22, GC23 and GC32 (Figs. 23-26). Within this mixed layer, cores GC12 and GC23 both have a maximum at the depth of ^{7}Be penetration in its corresponding box core (~ 20 cm bsf). Both also have a minimum at ~ 40 cm bsf, as does GC32, and another subsurface max the base of this "mixed layer". Below this mixed layer is a region of logarithmic decay with depth. Gravity core GC22 does not exhibit this trend, and the profile only reflects a logarithmic decrease with depth. Accumulation rates determined from the log layer range from 2.9 cm y^{-1} for core GC23, 3.1-3.6 cm y^{-1} for cores GC12 and GC32, to 5 cm y^{-1} for core GC22 (Figs. 23-26; Table 1), with no obvious trend in accumulation rates relative to core location.

Profiles of $^{210}Pb_{xs}$ determined using alpha detection resulted in either relatively uniform profiles throughout the entire depth of the core, such as core GC32 (Fig. 26), or uniform to ~100 cm, such as core GC22 (Fig. 24). Because of variable $^{210}Pb_{xs}$ activities, equation (1) was fitted to selected points only at the top and bottom of the ^{210}Pb profiles. These values range from ~2.2 cm y^{-1} at inshore sites, and 4.3-5.1 cm y^{-1} at offshore sites (Table 1), which compare favorably with

minimum accumulation rates derived from ^{137}Cs profiles. However, since these values are very loosely constrained, we will consider them only estimates.

Time-Series Sites: March and May 2002

In 2002, the study region was expanded to include a shore normal transect on the eastern side of FWB canal, as well as a shore normal transect south of Southwest Pass, the opening between Marsh Island and the coast that allows Vermillion Bay to empty into the Gulf of Mexico (Fig. 27). Only boxcores were taken, sub-sampled for X-radiography, radioisotopes, grain size, and porosity as described previously.

For the purpose of discussion of the comparison between March and May 2002, the study area has been divided into three regions (Fig. 27): West of FWB canal (1 shore normal and 1 shore parallel transect), east of FWB canal (1 shore normal transect) and south of SW Pass (1 shore normal transect across Trinity and Tiger shoals).

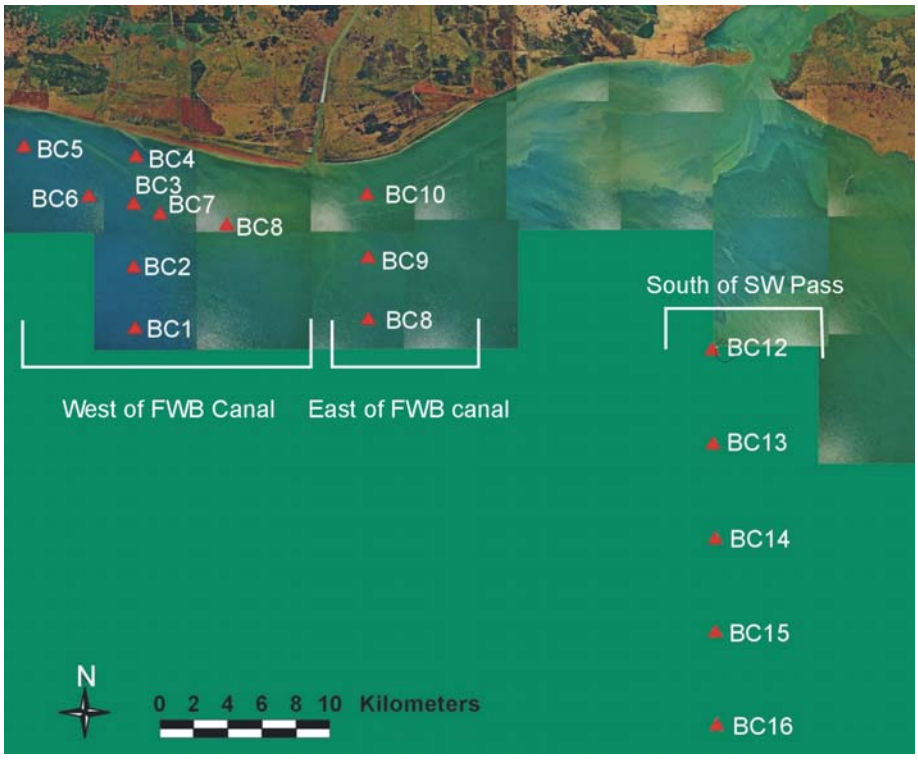

Figure 27. Location map for AC0302 cores collected in March 2002.

March 2002

Sedimentary Facies

Unlike the samples collected in 2001 when the characteristics of all the sites appeared relatively uniform, in 2002, a greater variety in sediment characteristics occurred at all the sites. These variations may be attributed in part to the greater spatial variation of similar processes, but they also appear to be a result of different processes occurring at each site. For the region west of FWB canal, also sampled in 2001, the X-radiographs revealed numerous packages of alternating beds of low-density mud and higher density silts (Figs. 28-31A, 31B, 31C and 31D). The packages may range from 2-6 cm thick throughout the core, with the uppermost mud/silt couplet only 2-4 cm thick. The macrofauna found within the cores include polychaetes and acorn worms (enteropneusts). Core AC0302 BC1 (Fig. 28), located furthest offshore, has nearly horizontal bedding, with numerous silt layers, some with both sharp upper and lower boundaries, and others that may either grade up or down into the surrounding finer grained sediment. At 8 cm, a sharp-based silt layer appears that does not extend across the X-ray but becomes a more diffuse region of silts that joins with the underlying silt layer at 12 cm. Below 16 cm, a transition to lower density sediment occurs, and below 25 cm, the fabric appears massive, with shells visible in the X-radiograph. Grain size analysis confirms a change in the grain size distribution (from average 32% silt, 67% clay, to ~20% silt, 80% clay) at 14-16 cm (Fig. 28). Burrows (mm-scale) were visible throughout the whole depth of the X-radiograph, particularly in the upper 7 cm of the core. Though this core was burrowed, physical stratification was still visible. Moving landward, core AC0302 BC2 (Fig. 29) also exhibited nearly horizontal bedding, with 2-4 cm thick fining upward packages. Throughout the upper 17 cm of the core were mm-scale burrows, mainly concentrated in the upper 7 cm. The surface of this X-radiograph had

AC0302 BC1

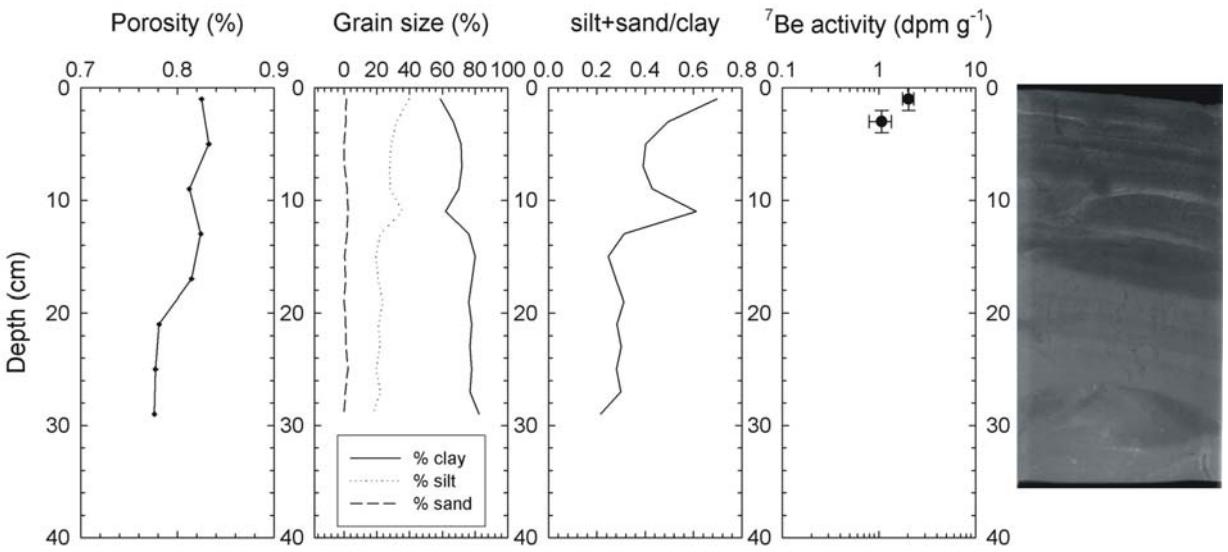

Figure 28. Porosity, grain size, silt+sand/clay ratio, ^{7}Be activity and X-radiograph for core AC0302 BC1.

AC0302 BC2

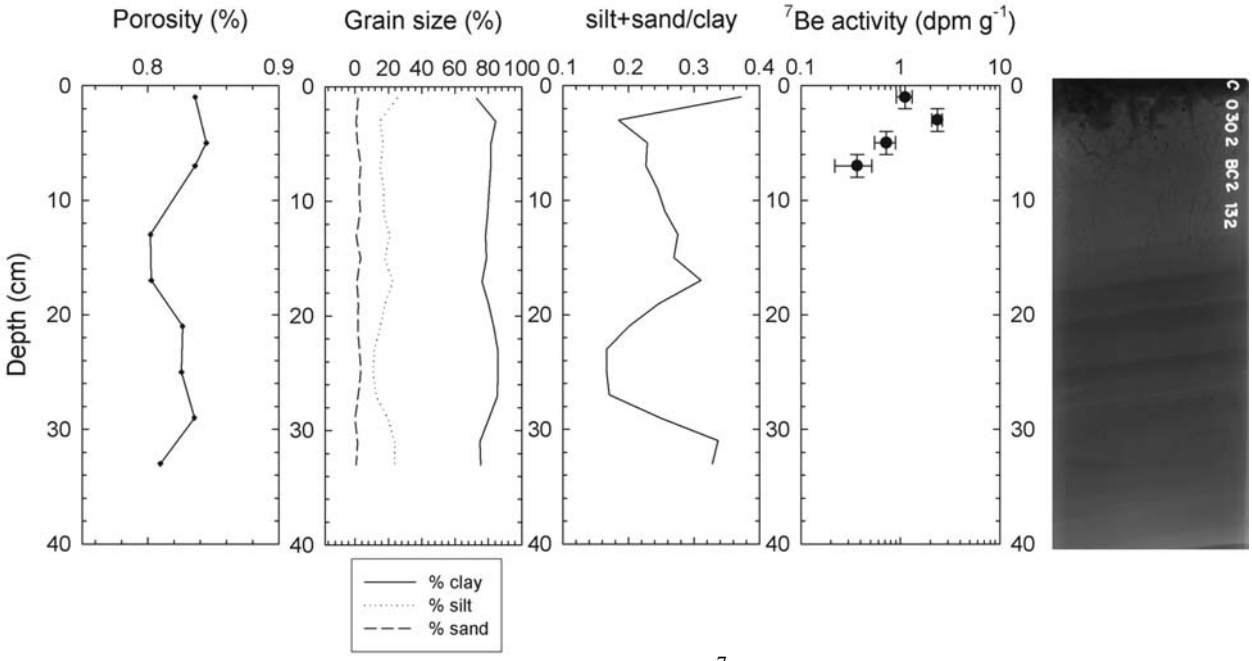

Figure 29. Porosity, grain size, silt+sand/clay ratio, ^{7}Be activity and X-radiograph for core AC0302 BC2.

many visible burrows. Core AC0302 BC3 (Fig. 30) exhibited a pelletized surface, nearly horizontal bedding, sharp-based silty layers and no visible macrofauna burrows. The silty layers within this core appear to grade upward into the overlying finer sediment. Cores AC0302 BC4 and BC4A (Figs. 31A and 31B, respectively) were collected at the landward most sites along this transect. Core AC0302 BC4 also has very few burrows visible in the X-radiograph, but nearly horizontal bedding, erosional contacts, and convoluted silty layers that are sharply based, but with either gradational or sharp upper bounds. Core AC0302 BC4A, taken in approximately the same location, also had few visible burrows, nearly horizontal layering of silty layers, with sharp upper and lower bounds, and an erosional contact at ~20 cm.

Core AC0302 BC5 (Fig. 31C), located furthest west, penetrated the seabed at an angle. The lower half of the core, bounded by a shell layer at ~19 cm, exhibits horizontal layering of

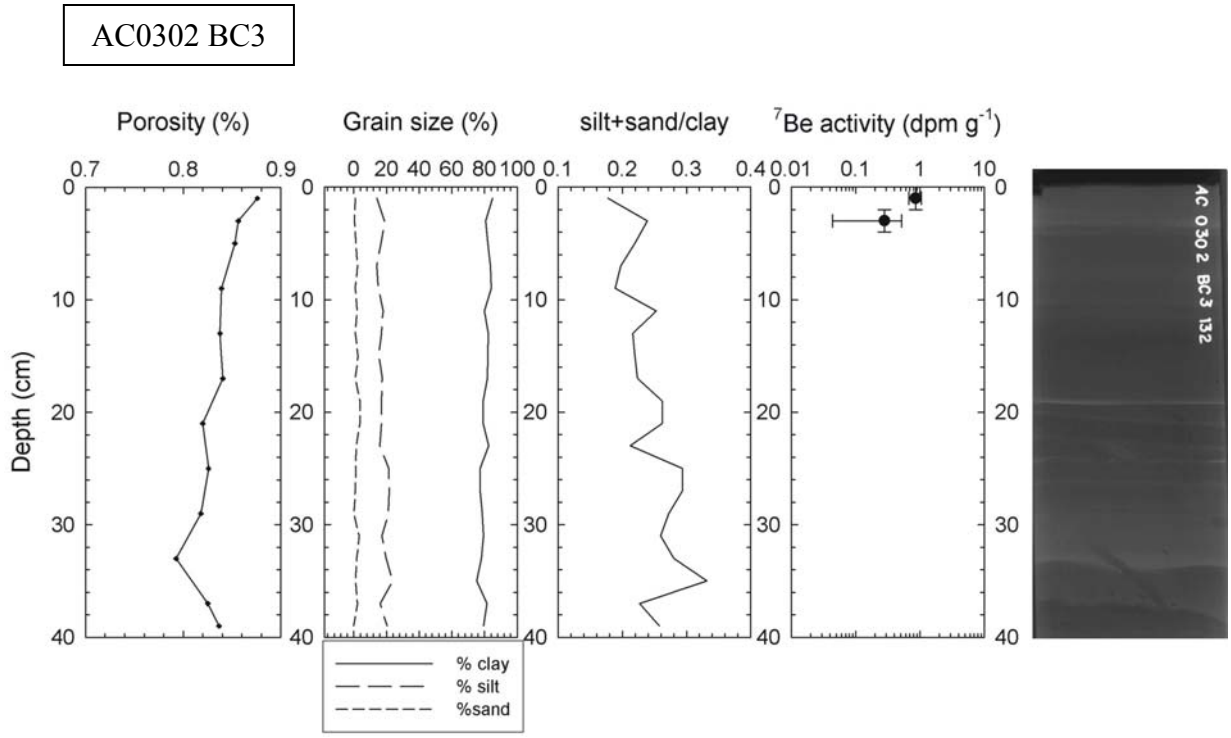

Figure 30. Porosity, grain size, silt+sand/clay ratio, ^{7}Be activity and X-radiograph for core AC0302 BC3.

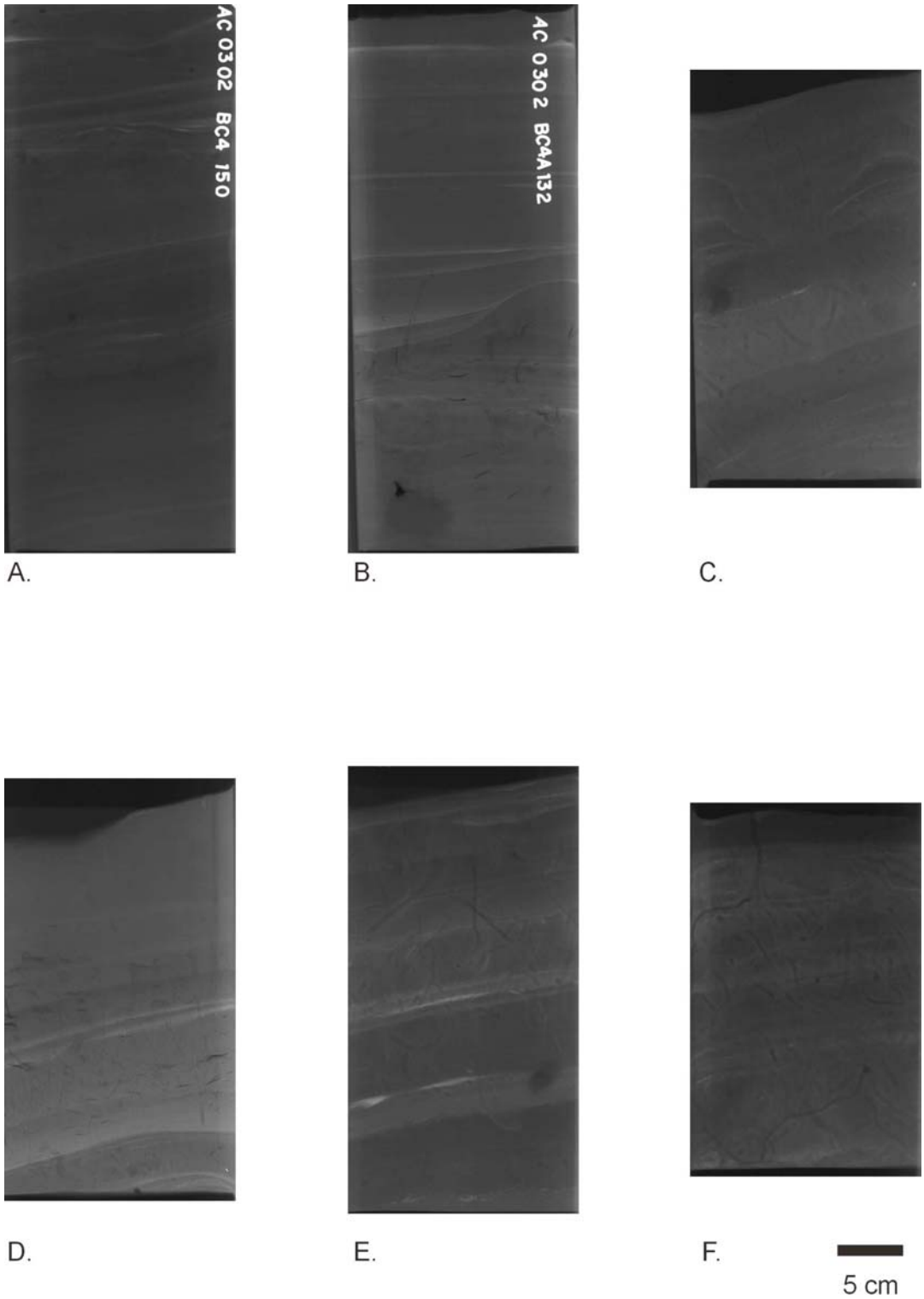

Figure 31. X-radiographs for cores (A) AC0302 BC4; (B) AC0302 BC4A; (C) AC0302 BC5; (D) AC0302 BC8; (E) AC0302 BC9; (F) AC0302 BC11.

mud and silty packages and <0.5 cm diameter burrows. Above this is a region of mud and silt that may have been stratified, but has been scoured with new deposition exhibiting physical stratification and fewer burrows deposited on top.

The transect east of FWB canal (Fig. 27) consisted of three sites (AC0302 BC10; Fig. 32, AC0302 BC9; Fig. 31E, and AC0302 BC11; Fig. 31F), with all X-radiographs also showing horizontal layering of mud/silt couplets. The silty layers are generally well defined, with sharp lower bounds, though the upper contact may range from sharp to gradational. The X-radiographs of these cores become increasingly visibly burrowed, with 2-mm diameter burrows, and the discrete silt layers become more diffuse seaward. Core AC0302 BC10 had few burrows visible in the upper 15-20 cm, but within the core were acorn worms ~ 25 cm and open, oxidized burrows to 30 cm. Erosional contact is visible in the X-radiograph at this depth as well. Macrofauna within all three cores included acorn worms (probably genus *Schizochardium*) and lesser numbers of polychaetes.

The transect south of SW Pass consisted of 5 stations, with core AC0302 BC13 located on Tiger Shoal and core AC0302 BC15 on Trinity Shoal (Fig. 27). The two northernmost sites (AC0302 BC12; Fig. 33 and AC0302 BC13; Fig 34) were the muddiest and had the best core recovery. The X-radiograph for core AC0302 BC12 had a much higher concentration of silts, shells and sands than the westward cores, visible by the high number of high-density layers in the X-radiograph, as well as the grain size data (Fig. 33). The upper 4 cm of the core consists of layered mud with little visible burrowing, though numerous burrows were visible throughout the rest of the X-ray. Core AC0302 BC13 also had an upper 4 cm layer of mud, overlying a sandy layer, with mottled shelly silts below (Fig 34). Continuing offshore, the sites become mainly dark brown stiff shelly mud nearly impenetrable to the boxcore; only surface samples were

AC0302 BC10

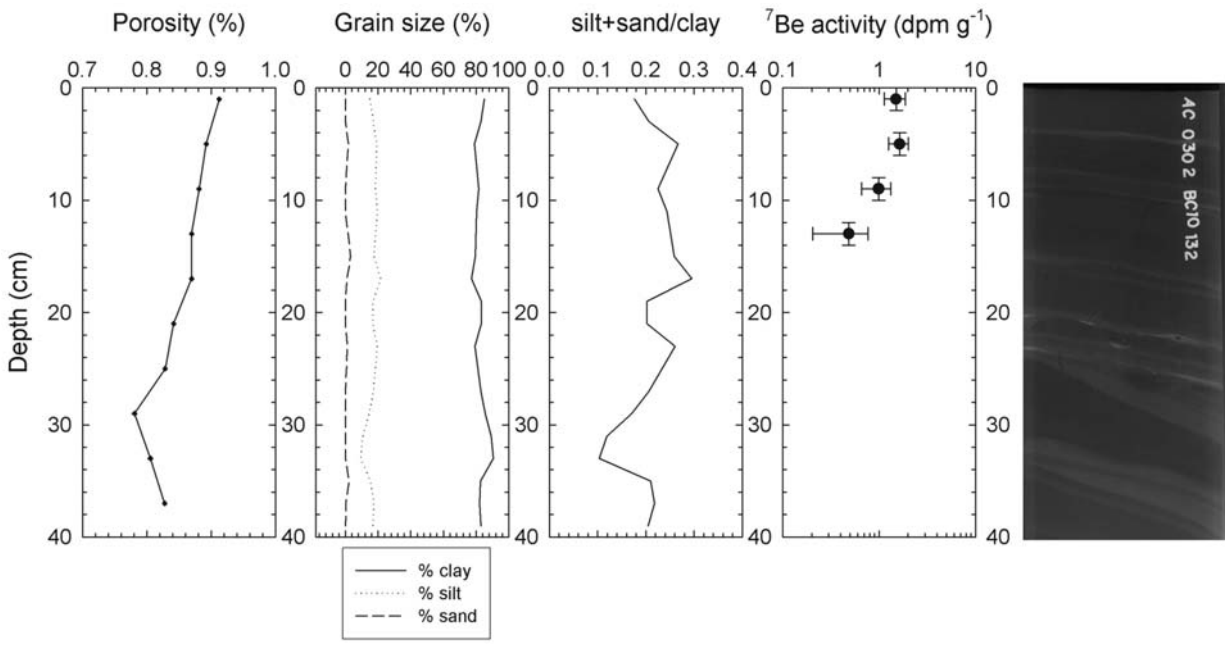

Figure 32. Porosity, grain size, silt+sand/clay ratio, ^{7}Be activity and X-radiograph for core AC0302 BC10.

AC0302 BC12

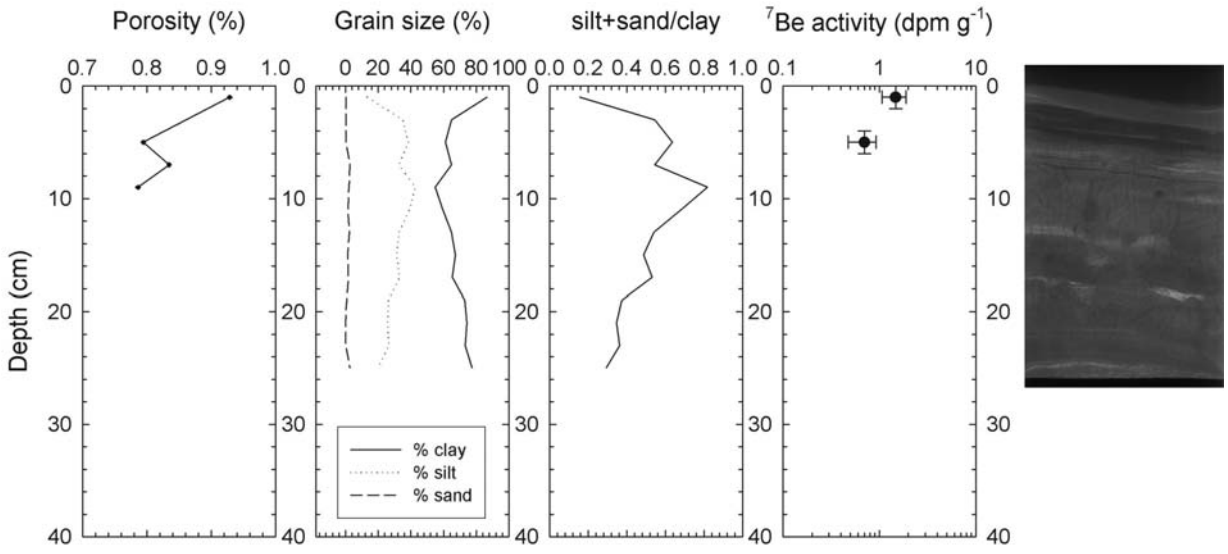

Figure 33. Porosity, grain size, silt+sand/clay ratio, ^{7}Be activity and X-radiograph for core AC0302 BC12.

AC0302 BC13

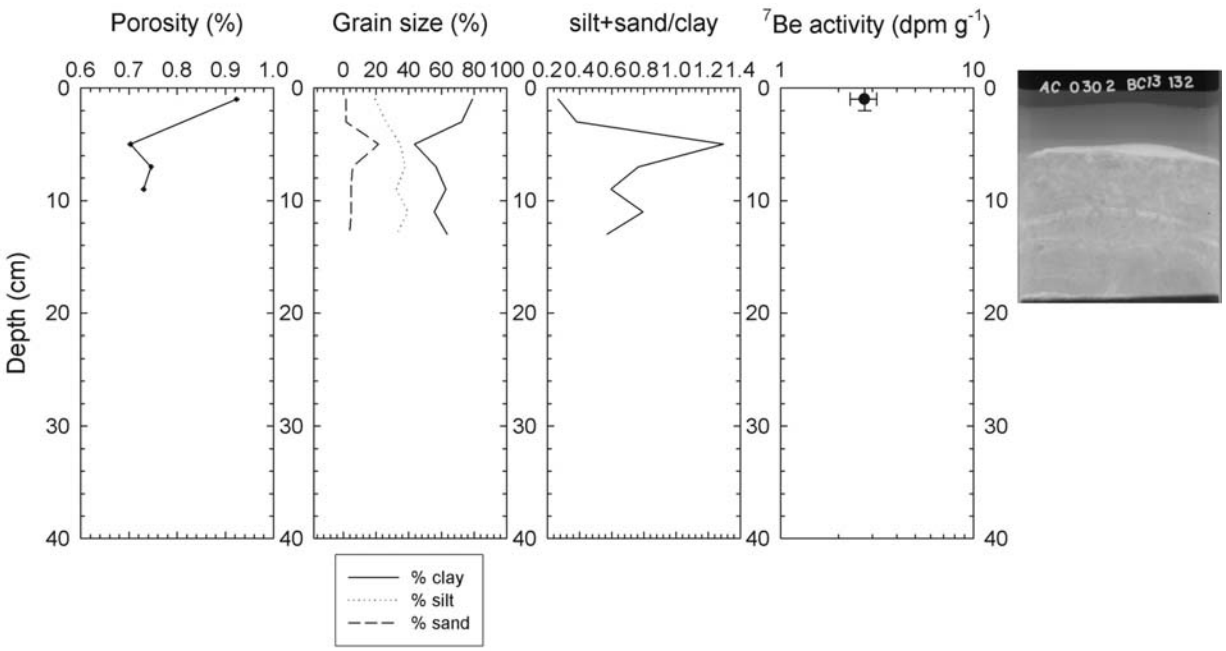

Figure 34. Porosity, grain size, silt+sand/clay ratio, ^{7}Be activity and X-radiograph for core AC0302 BC13.

recovered. A thin (<0.5 – 1 cm) layer of light brown fluid mud occurred overlying stiff shelly mud at all the sites, except on Trinity shoal (site AC0302 BC15), a local bathymetric high.

Radioisotopic Analysis

The ^{7}Be surface activities were highest at the furthest offshore site AC0302 BC1 (2.8 dpm g^{-1}) and relatively low (0.2 - 0.5 dpm g^{-1}) or not detectable at the inshore stations (Fig. 27, 28-30). Where ^{7}Be is present in the core deeper than the surface layer, the ^{7}Be profiles show a logarithmic decrease with depth (Figs. 28 and 30). The maximum inventory (2.8 dpm cm^{-2}) is much lower than the previous year and occurs in a depocenter located approximately at the same longitude as the 2001 depocenter, but ~6 km farther offshore (site AC0302 BC1) (Fig. 35). The penetration depth of ^{7}Be in this core is 4 cm and is bound by a basal silt layer. Cores AC0302 BC2 and AC0302 BC3 had ^{7}Be present deeper in the core (6 cm) but overall lower inventories.

On the eastern side of FWB canal, Core AC0302 BC10, collected from the most shoreward location along the transect, had relatively high ^{7}Be inventory (2.5 dpm cm^{-2}; Fig. 35). Beryllium-7 penetrated to 14 cm in this core, the deepest of all the sites. The ^{7}Be profile for core AC0302 BC10 (Fig. 32) showed two gradients: (1) a surface "mixed" layer to 6 cm (which may be due to either seabed mixing or rapid deposition of sediment) with relatively uniform profiles; and (2) a lower layer of more rapid logarithmic decay with depth. These two regions may be separated by a silt layer**,** and the total ^{7}Be interval is generally bound by a basal silt layer (Fig 32). The seaward cores (AC0302 BC9 and AC0302 BC11) did not contain any detectable ^{7}Be.

Along the transect south of SW Pass (Fig. 27), ^{7}Be inventories (Fig. 35) were highest at the most shoreward site (AC0302 BC12, where ^{7}Be penetrates to 6 cm) and decreased offshore

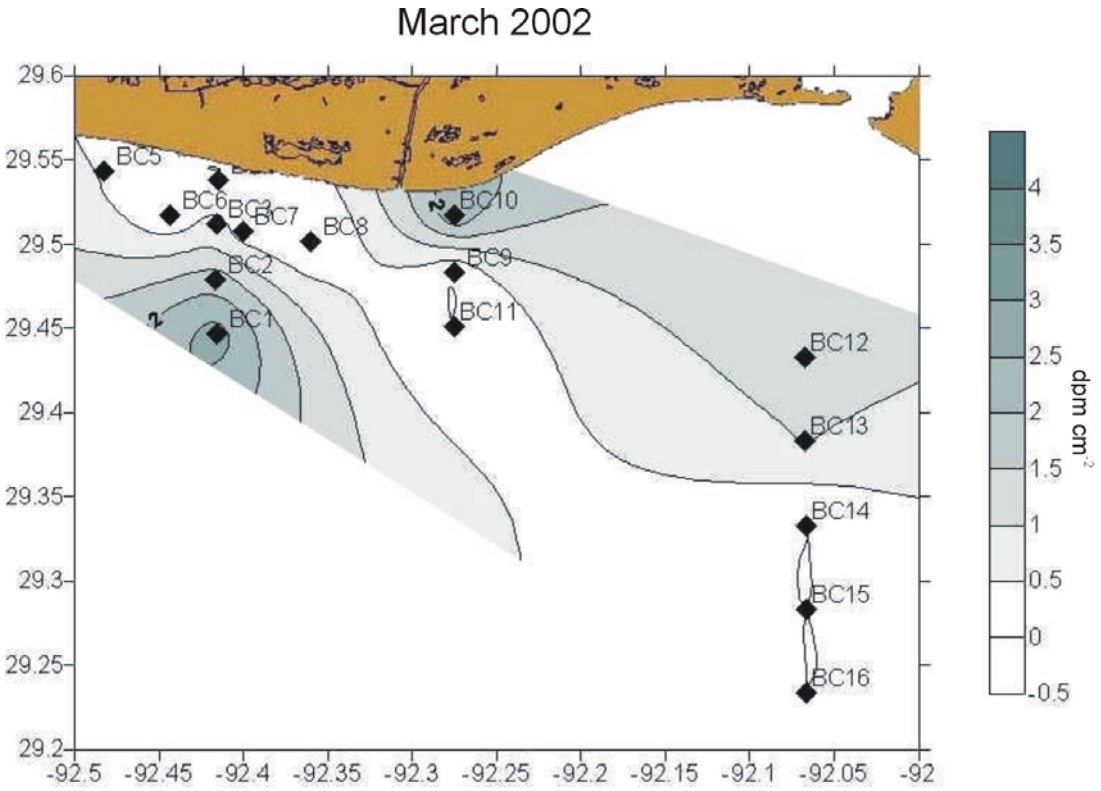

Figure 35. Beryllium-7 inventory map showing the location of maximum deposition in March 2002. The maximum inventory is 2.8 dpm cm^{-2}. The diamonds represent the sampling sites.

to undetectable levels at AC0302 BC14 to AC0302 BC16. The ^{7}Be profiles for the sites that contain ^{7}Be deeper than the surface layer (AC0302 BC12 and AC0302 BC13, Figs. 33 and 34) show a pronounced logarithmic decrease in activity with depth.

May 2002

Sedimentary Facies

Cores AC0502 BC1, BC2, BC3/BC8, and BC4B/BC5 are located along a shore-normal transect (Fig. 36), that define a time-series with AC0302 cores BC1, 2, 3, and 4B (Fig. 27). These cores all exhibit nearly horizontal bedding downcore, with the exception of core AC0502 BC1 (Figs. 37-40). Core AC0502 BC1 (Fig. 37), located furthest offshore, consisted of nearly horizontal bedding only in the upper 8 cm, and below 26 cm. Between 8 and 26 cm, the X-radiograph shows the core becomes mottled, and grain size analysis indicates decreased clay content (from 80 to 60%) and an increase in silts to 40%. This core has burrows throughout the

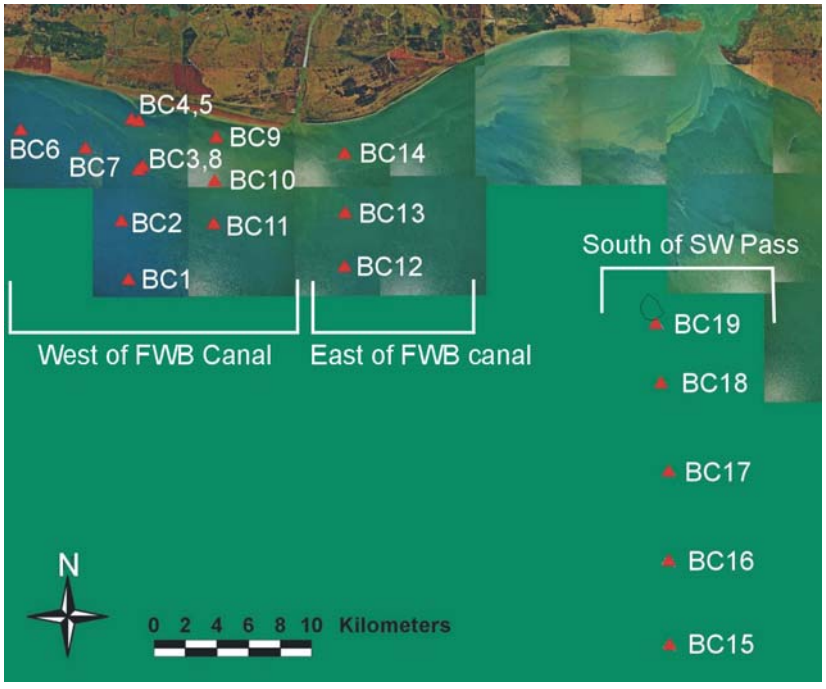

Figure 36. Location map of AC0502 cores, collected May 2002.

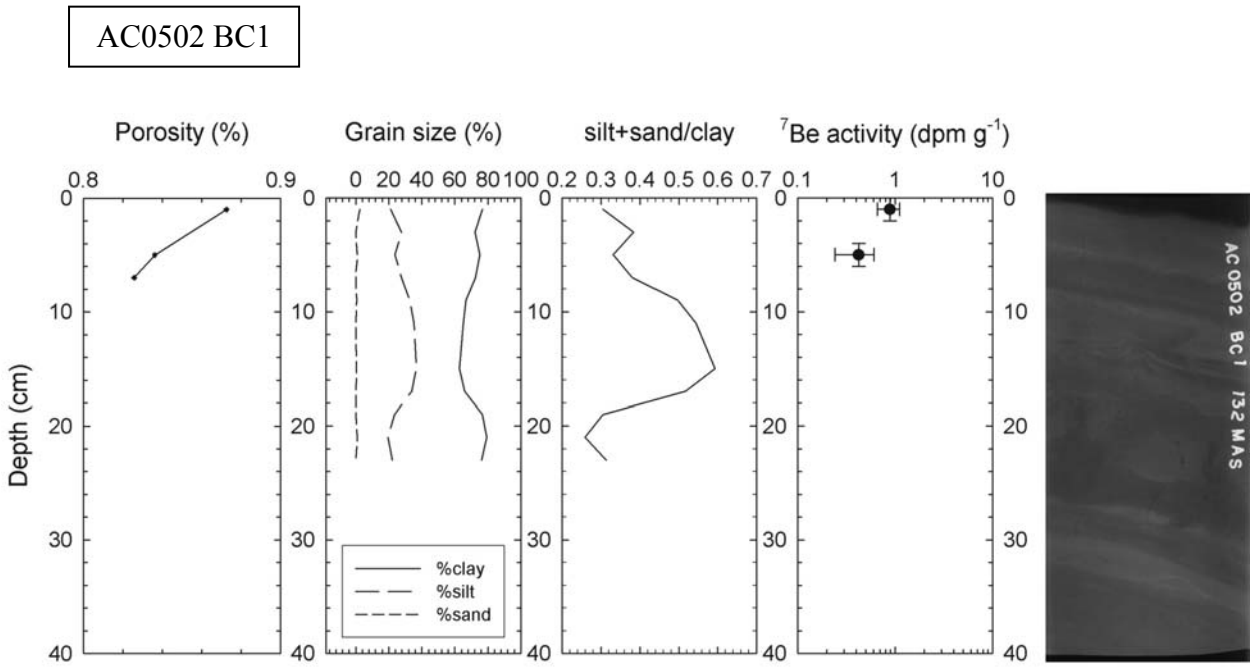

Figure 37. Porosity, grain size, silt+sand/clay ratio, ^{7}Be activity and X-radiograph for core AC0502 BC1.

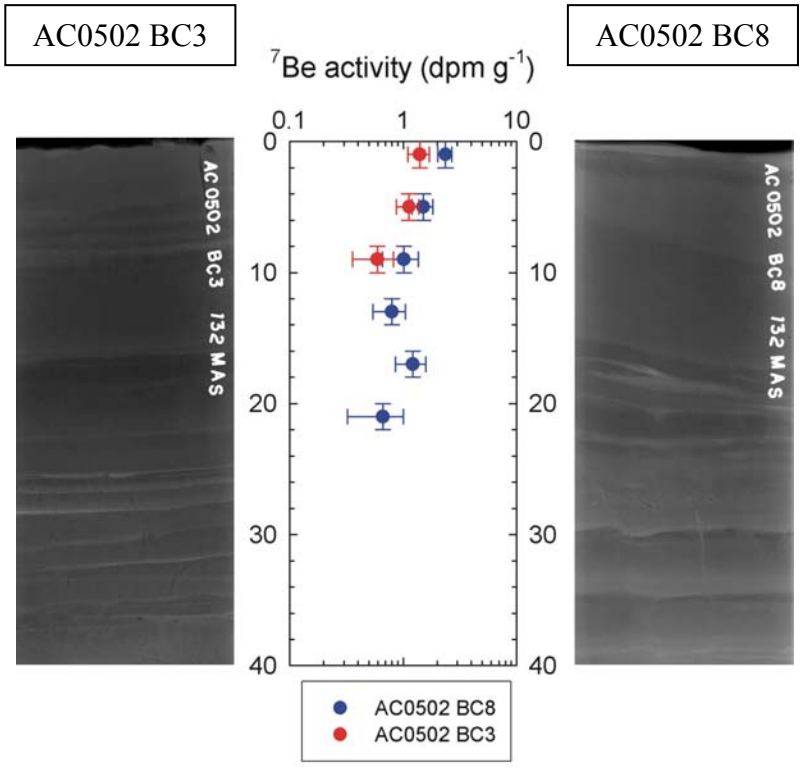

Figure 38. X-radiographs and ^{7}Be activity for cores AC0502 BC3 and BC8, location at approximately the same region.

AC0502 BC4B

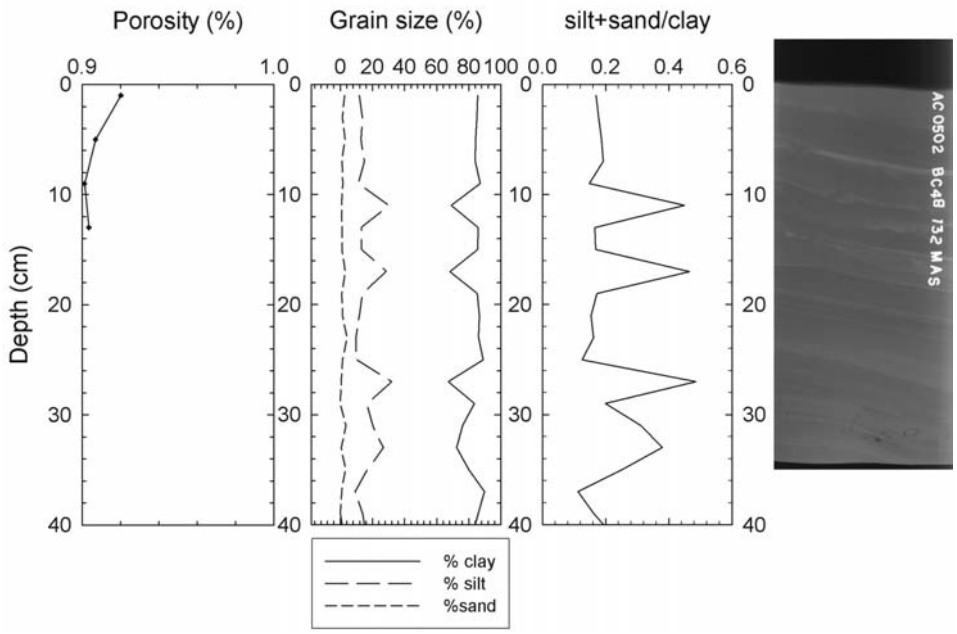

Figure 39. Porosity, grain size, silt+sand/clay ratio and X-radiograph for core AC0502 BC4B.

AC0502 BC5

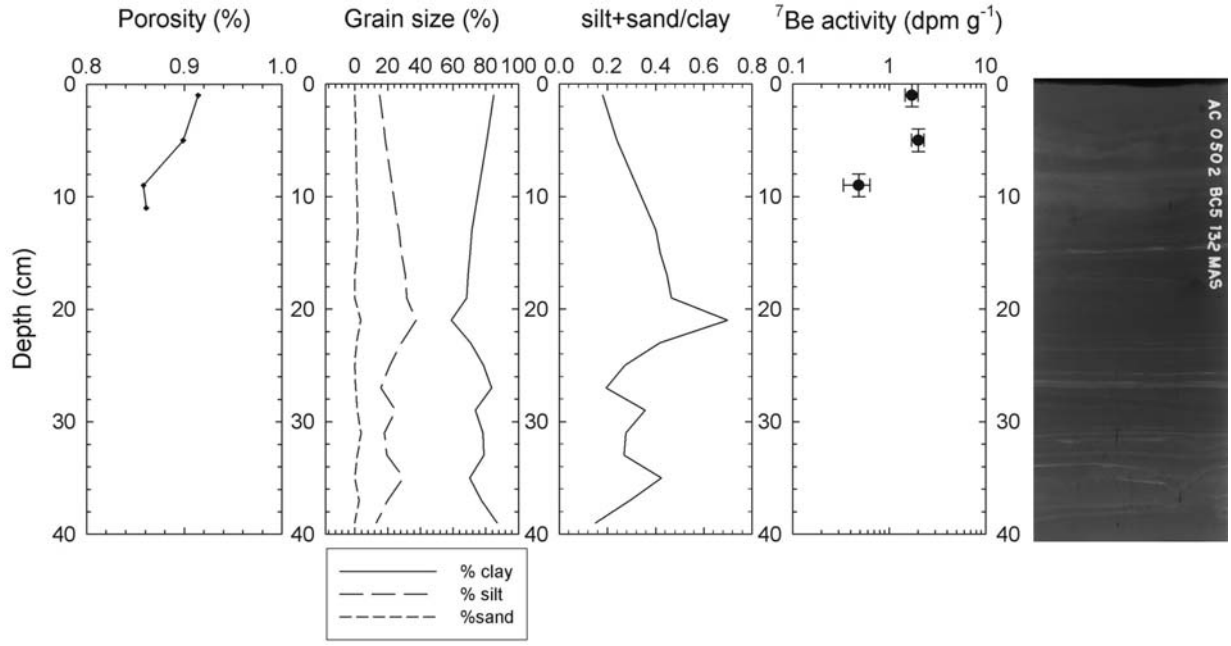

Figure 40. Porosity, grain size, silt+sand/clay ratio, ^{7}Be activity and X-radiograph for core AC0502 BC5.

entire depth of the core. The X-radiographs for cores AC0502 BC3 and AC0502 BC8 (Fig. 38), taken from nearly the same location, both have few visible burrows, and none within the upper, most recently deposited sediment. Both cores are physically stratified, and have sharply based silty layers and erosional contacts below 24 cm in core BC3, and below 16 cm in BC8. Most of the silty layers grade upward into the finer sediment. The landward most cores collected along this transect, sites AC0502 BC4B (Fig. 39) and AC0502 BC5 (Fig. 40), were collected on opposing sides of a platform. Both have few burrows > 1 mm, and mud/silt couplets occurring frequently throughout the cores. The silts appear as discrete layers, with both sharp upper and lower contacts. The bedding in the upper 10 cm of core AC0502 BC5, collected from the eastern side of the platform, does not appear as distinct as core AC0502 BC4B.

The westernmost sites (AC0502 BC6 and AC0502 BC7; Fig. 41) were hard shelly mud bottoms with seabed surfaces that appeared scoured. Their irregular surfaces are visible in the X-radiographs. Mud and silt stratification is visible throughout both cores, with the base of each layer appearing as an irregular contact. Grain size data shows that the surface of these cores may contain up to ~30% silt and ~ 70% clay (Fig. 41) and shells are visible on the surface of core AC0502 BC6.

Cores AC0502 BC9 (Fig. 42), AC0502 BC10 (Fig. 43A) and AC0502 BC11 (Fig. 43B), the easternmost sites on the west side of FWB canal, are characterized by clay-rich sediments with multiple silty layers. The number of mm-scale burrows in the cores increases seaward, with core AC0502 BC11 having abundant burrows throughout the entire depth of the core. No macrofauna were found in the biological core samples.

East of FWB canal (Fig. 36), cores AC0502 BC14 (Fig. 44), AC0502 BC13 (Fig. 45), and AC0502 BC12 (Fig. 43C) define a third N-S transect. These cores are predominantly mud

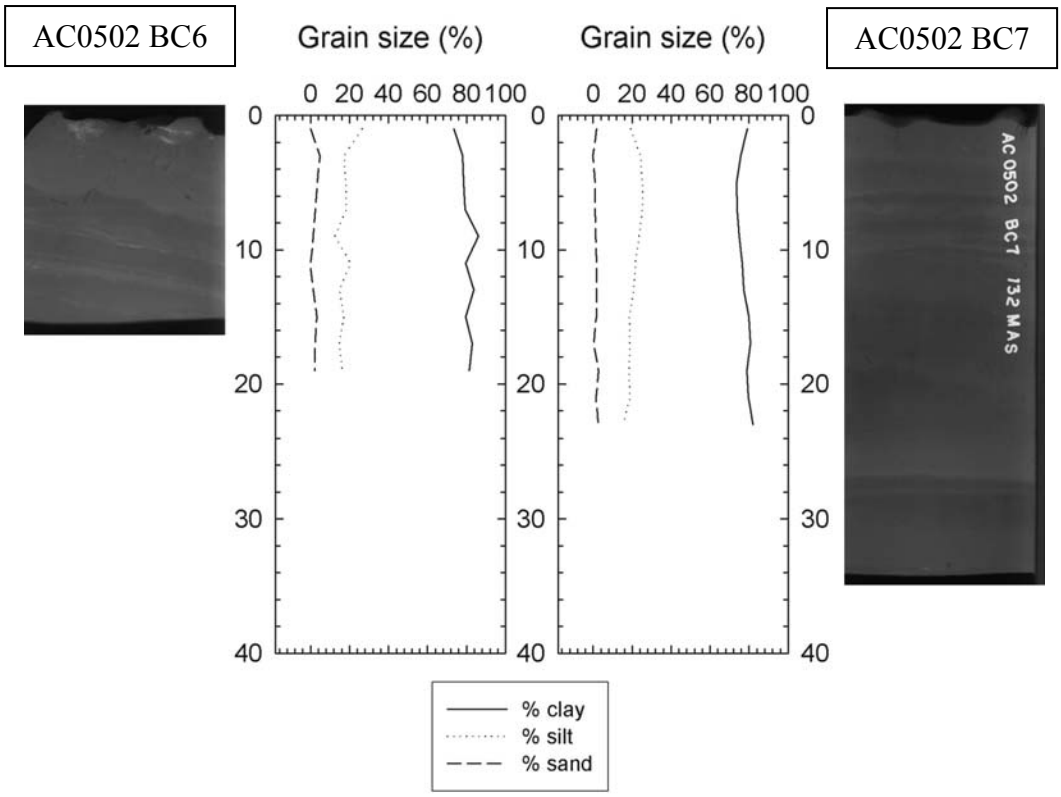

Figure 41. X-radiographs and grain size data for cores AC0502 BC6 and AC0502 BC7, the westernmost cores of the study area.

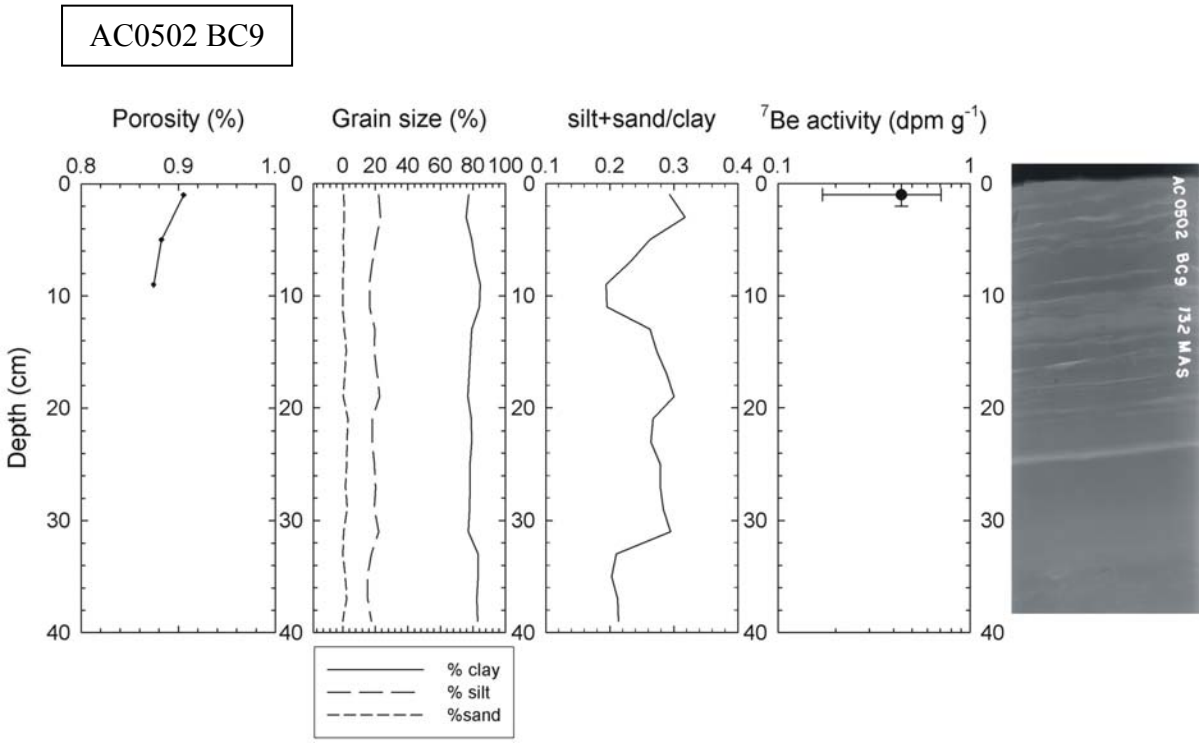

Figure 42. Porosity, grain size, silt+sand/clay ratio, ^{7}Be activity and X-radiograph for core AC0502 BC9.

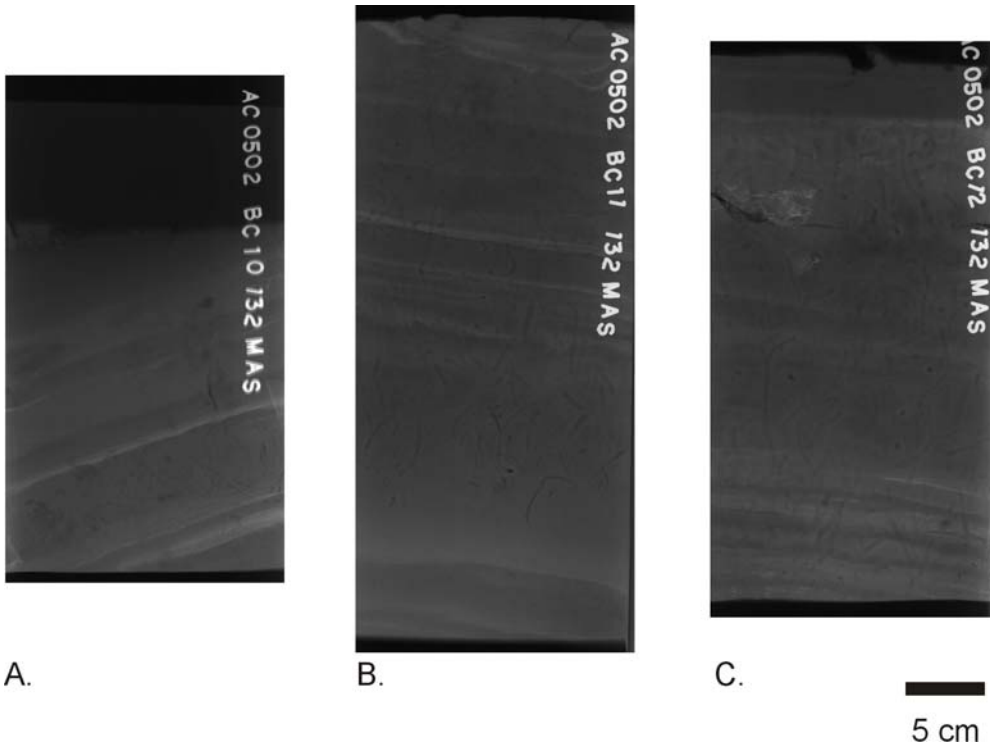

Figure 43. X-radiographs for cores (A) AC0502 BC10; (B) AC0502 BC11; (C) AC0502 BC12.

AC0502 BC14

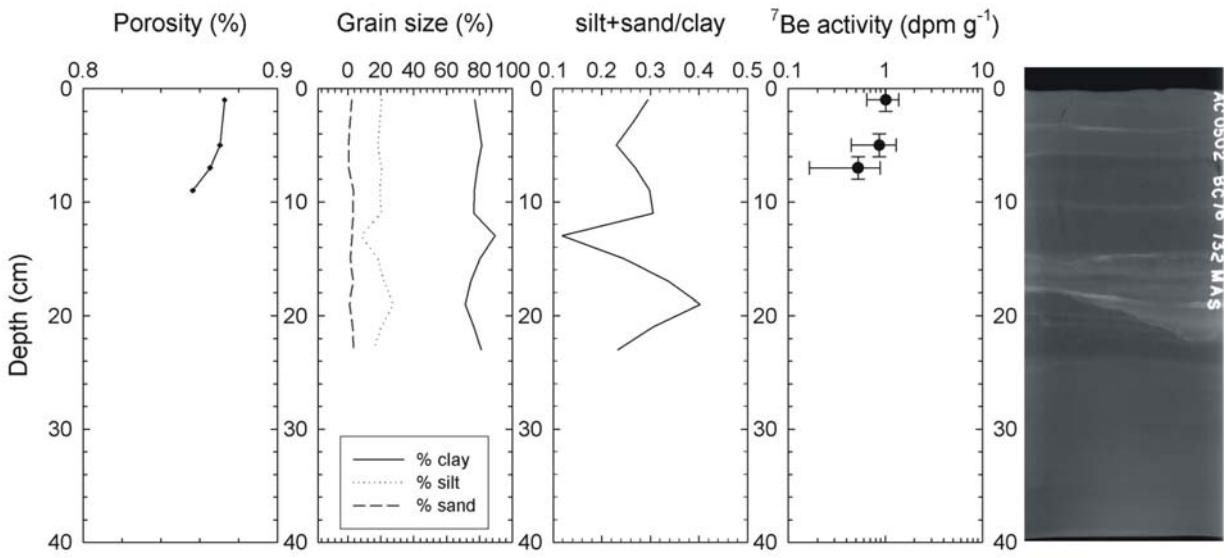

Figure 44. Porosity, grain size, silt+sand/clay ratio, ^{7}Be activity and X-radiograph for core AC0502 BC14.

AC0502 BC13

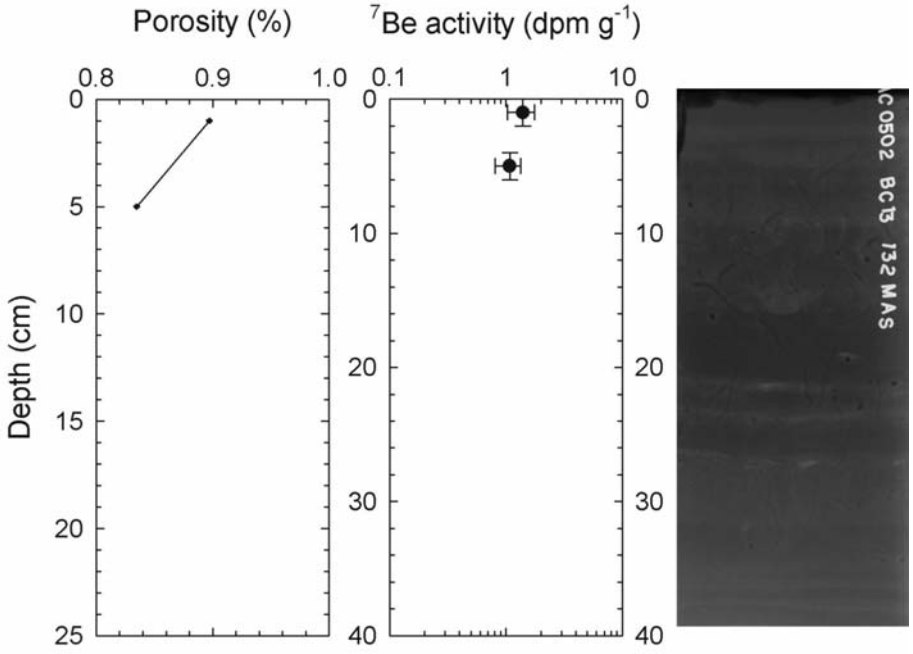

Figure 45. Porosity, ^{7}Be activity and X-radiograph for core AC0502 BC13.

with multiple silt layers, but with a scoured irregular surface. The scoured surface of the cores is visible in the X-radiographs. The X-radiograph for Core BC14 contains no visible burrows, and grain size analysis shows a high concentration of silts at 16-20 cm. The basal silt layer of this interval is erosional, crosscutting the underlying nearly horizontal layers. Above this erosional surface, there is no other evidence of erosion throughout the X-radiograph. Cores AC0502 BC13 and AC0502 BC12 have numerous burrows and shells visible in the X-radiographs, although primary depositional fabric is still partially preserved. Acorn worms and polychaetes were found in both core samples. Overlying the burrowed sediment of both cores AC0502 BC13 and AC0502 BC12 is a mud layer ~ 2-4 cm thick, that does not appear burrowed.

The sites south of SW Pass (Fig. 36) across the shoals have hard shelly/sandy bottoms. Only the most northward site (AC0502 BC19, Fig. 46) was muddy enough for a boxcore to penetrate deep enough to retrieve more than a surface sample. This site had ~4 cm of mud overlying a shelly layer. Moving south, site AC0502 BC18 also had a muddy surface (~2 cm) overlying a sandy bottom. The remainder of the transect sites had hard shelly/sandy bottoms, with no evidence of recent mud deposition.

Radioisotopic Analysis

Cores AC0502 BC1 and AC0502 BC2, where the highest deposition occurred in March 2002, now have low ^{7}Be inventories (0.9 dpm cm^{-2} and below detection, respectively; Fig. 47). The highest ^{7}Be inventory (Fig. 47) occurred at site AC0502 BC8 (5.1 dpm cm^{-2}). Site AC0502 BC3, located in approximately the same location, had an inventory of 0.7 dpm cm^{-2}. Core AC0502 BC5, on the eastern side of the platform, had a ^{7}Be inventory of 2.2 dpm cm^{-2}, while core AC0502 BC4B, on the western side of the platform, had no detectable ^{7}Be. The ^{7}Be profiles for all these cores show logarithmic decay with depth (Figs. 37, 38 and 40). Unlike the

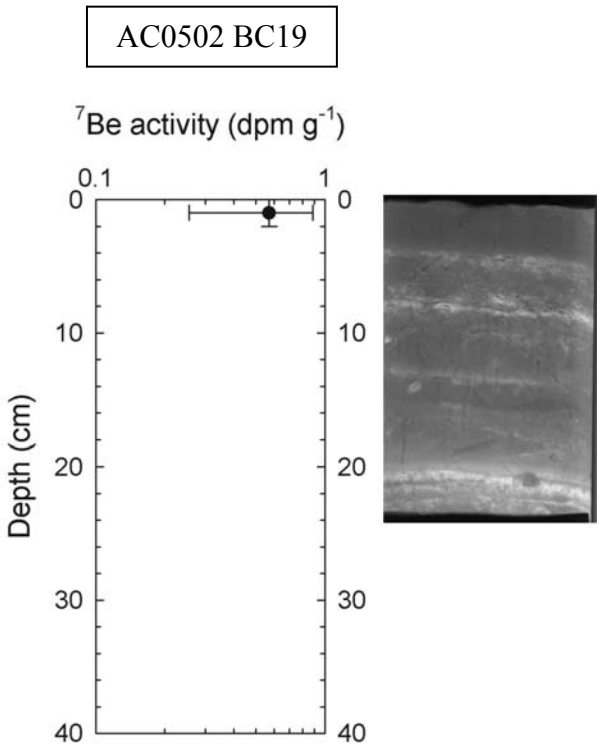

Figure 46. Beryllium-7 activity and X-radiograph for core AC0502 BC19.

May 2001 cores, multiple silt layers occurred throughout the ^{7}Be-laden interval. Some of these ^{7}Be profiles (AC0502 BC3, AC0502 BC5 and AC0502 BC8; Figs. 38 and 40) exhibit two gradients, a surface "mixed" layer and a region of logarithmic decrease with depth, that are often separated by a silt layer.

The westernmost cores AC0502 BC6 and AC0502 BC7 did not contain ^{7}Be above detection limits, nor did cores AC0502 BC9, AC0502 BC10 and AC0502 BC11, located on the eastern side of the AC0502 BC1-5, BC8 transect (Fig. 47).

On the eastern side of FWB canal (AC0502 BC14, AC0502 BC13, and AC0502 BC12), ^{7}Be activities and inventories decrease seaward, with ^{7}Be penetration depths ranging from 8 cm inshore to 2 cm offshore (Figs 44, 45 and 47). Beryllium-7 is present within the surface mud layer, basally bound by a silt layer in core AC0502 BC14, and by highly bioturbated and shelly

sediment in cores AC0502 BC13 and AC0502 BC12. The ^{7}Be inventory for core AC0502 BC14 is 1.6 dpm cm^{-2}, 1.7 dpm cm^{-2} for core AC0502 BC13, and 0.6 dpm cm^{-2} for core AC0502 BC12. The ^{7}Be profile for core BC14 (Fig. 44) shows two gradients, with a surface mixed layer to 6 cm

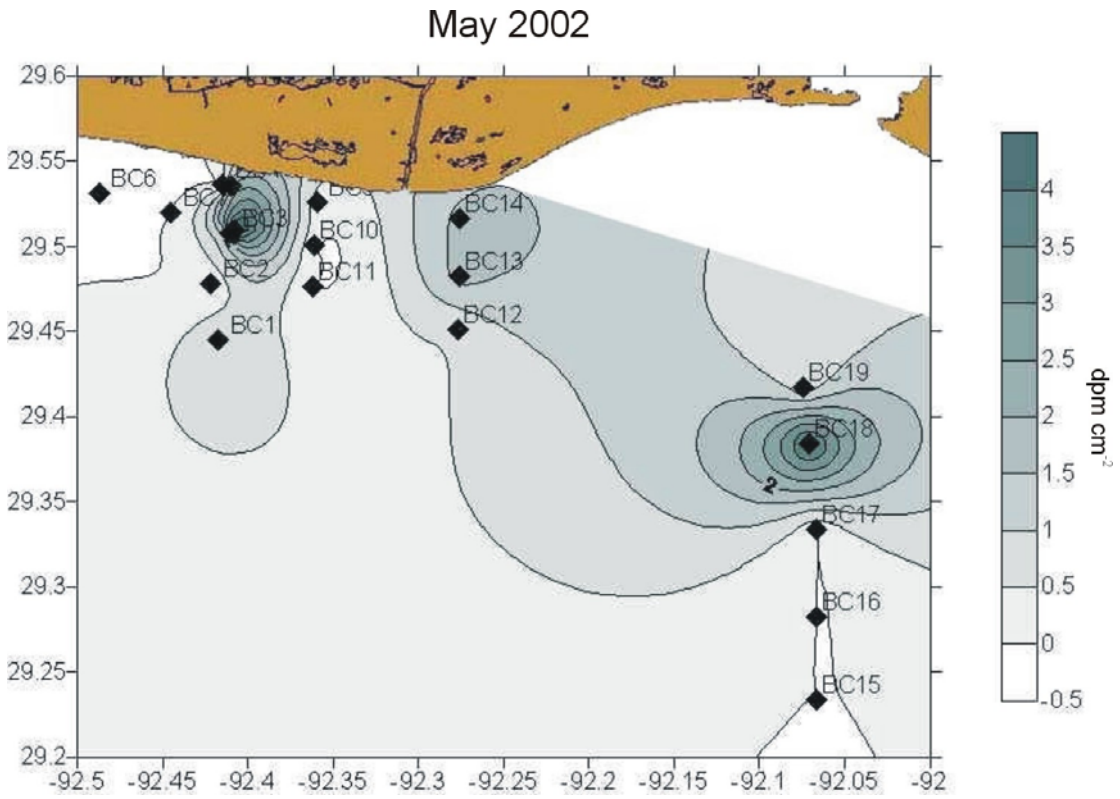

Figure 47. Beryllium-7 inventory map showing the location of maximum deposition in May 2002. The maximum inventory is 5.1 dpm cm^{-2}. The diamonds represent the sampling sites.

and a region of logarithmic decrease with depth to 8 cm. This gradient change is marked by a silt layer at 6 cm bsf. The ^{7}Be profile for AC0502 BC13 (Fig. 45) is relatively uniform, showing a slight decrease with depth. Core AC0502 BC12 only has ^{7}Be present in the surface layer.

Along the transect south of SW Pass (Fig. 47), core AC0502 BC19 (Fig. 46) has ^{7}Be present only in the upper 2 cm, with an inventory of 0.5 dpm cm^{-2}. Core AC0502 BC18, further seaward, had ^{7}Be present to 6 cm, with an inventory of 4.3 dpm cm^{-2}. Seaward of these sites ^{7}Be was not detectable.

The total ^{7}Be inventory for the time-series sites in March and May were divided into two components: (1) Residual inventory, which is the inventory of the March sampling period decay-corrected to the date of May sampling; and (2) New inventory, which is the total inventory for May minus the residual inventory. This model assumes that ^{7}Be delivery and removal processes only occur in association with particulate matter. Results for each core are shown in Table 2. In some cases, the total inventory exceeds residual inventory, indicating deposition at that site (positive new inventory). In others, residual inventory is greater than the total inventory (negative new inventory), indicating erosion at that site. At the sites where the new and residual inventory difference is zero, no net change was presumed (Canuel et al., 1990). These values show that between March and May 2002, deposition occurred in the depocenter region west of FWB canal (sites BC3, BC5, BC8), as well along the transect directly east of FWB canal (sites BC13, BC14, BC12) and a single site seaward of SW Pass (site BC18). For most of the sites surrounding these regions no net change was found, except for the seaward sites BC1 and BC2, and the westernmost site BC6, where net erosion occurred.

Table 2. ^{7}Be inventory net change for time-series sites March and May 2002

March 2002 core	March 2002 Inventory (dpm cm^{-2})	Residual Inventory (March-decay corrected to May date)	May 2002 Inventory (dpm cm^{-2})	Difference	Net change
BC1	2.83(0.48)*	1.21(0.48)	0.95(0.30)	-0.26(0.37)	erosion
BC2	1.83(0.42)	0.78(0.41)	0	-0.78(0.18)	erosion
BC3	0.76(0.29)	0.32(0.29)	1.71(0.45)	1.38(0.47)	deposition
BC4	0	0, 2.18(0.39)	0, 2.19(0.39)	0, 2.19(0.39)	none, deposition
BC5	0.48(0.11)	0.20(0.11)	0	-0.20(0.05)	erosion
BC6	0	0	0	0	none
BC7	0.22(0.11)	0.09(0.11)	5.07(1.38)	4.98(1.38)	deposition
BC8	0	0	0	0	none
BC9	0	0	1.67(0.43)	1.67(0.43)	deposition
BC10	2.54(0.74)	1.07(0.74)	1.62(0.77)	0.55(0.84)	deposition
BC11	0	0	0.57(0.16)	0.58(0.16)	deposition
BC12	1.30(0.38)	0.54(0.38)	0.54(0.30)	-0.01(0.34)	same
BC13	1.08(0.16)	0.46(0.16)	4.32(0.98)	3.87(0.98)	deposition
BC14	0	0	0	0	none
BC15	0	0	0	0	none
BC16	0	0	0	0	none

*values in parentheses represent inventory error

DISCUSSION

River Discharge and Ephemeral Mud Deposition

Using ^{7}Be to Track River Sediment

As described in Chapter 2, the cosmogenic radionuclide ^{7}Be ($t_{1/2}$=52 days) is an excellent tracer of fluvial sediment in marine systems (Sommerfield et al., 1999). The presence of ^{7}Be in the upper layers of the boxcores indicates that the sediment has been recently deposited (<4 half-lives) from a fluvial source.

The cores collected in May 2001 lack evidence of bioturbation and exhibit only primary physical stratification, so isotopic profiles predominantly reflect physical depositional processes (Figs. 8-12). The presence and uniformity of the ^{7}Be profile suggest rapid deposition of the sediment derived (at least in part) from a fluvial source within a few months prior to core collection. Therefore, the surficial sediment containing ^{7}Be is probably a seasonal deposit of flood sediment from the Atchafalaya that is transported along the shelf by wind-wave currents associated with cold front passages. Measurements of $^{210}Pb_{xs}$ activities from the boxcores show subsurface maxima near the base of the ^{7}Be-laden layer, which also indicates the base of the most recent event layer (Figs. 8-12). The $^{210}Pb_{xs}$ signature of a flood deposit is characterized by low activities (Sommerfield et al., 1999). Since ^{210}Pb is produced in the water column and is scavenged on sediments, when a large amount of sediment is deposited at once, the sediment supply depletes the ^{210}Pb signal.

The multiple silty layers common to each clay enriched core do not contain detectable ^{7}Be and may be basal units formed during event layer deposition, by processes similar to those described by Stow and Bowen (1980), as explained previously. This process, in which increased bottom shear stress erodes the seabed, generally forms sharply based silt layers that grade

upward into finer sediment (Fig. 48) (*e.g.* AC0501 BC1 @ 22 cm; Fig. 8). However, not all silt layers observed in the X-radiographs exhibit this characteristic; often they have both sharp upper and lower contacts (*e.g.* AC0501 BC1 @ 14cm; Fig. 8). Sharp upper contacts may indicate resuspension or erosion of the overlying fine sediment, leaving a sharp or irregular surface.

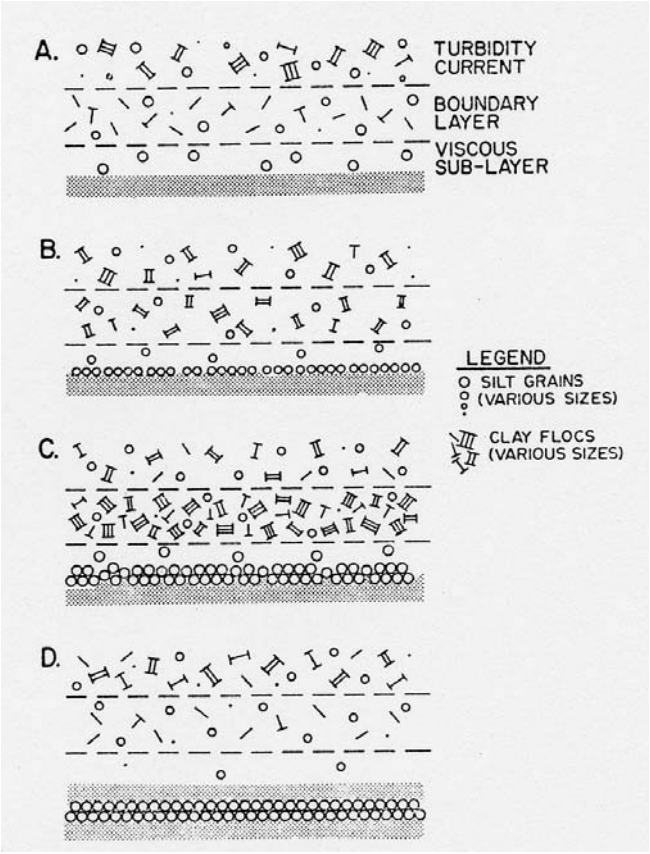

Figure 48. Schematic of the stages of silt and mud deposition due to shear sorting in the bottom boundary layer. (A) Silt grains settle through the viscous sublayer; (B) Silt lamina deposited with a sharp lower boundary; (C) Mud concentration increases at the top of the boundary layer, and flocculation can occur; (D) High enough concentration allows clays to overcome shear and rapidly deposit over the silt laminae. This may be repeated several times for successively finer grain sizes, grading into clay (after Stow and Bowen, 1980).

Beryllium-7 inventories show that in 2001, the distribution of ^{7}Be is relatively uniform throughout the study region, but tends to be focused on a depocenter located on the west side of the FWB canal (Fig. 15). The lack of macrofauna and obvious burrows from the cores, as well

as the ^{7}Be activity profiles, indicates that the sediment was deposited as a single, recent event. The cores collected in March and May 2002 differ from 2001 in that numerous macrofauna, including polychaetes and acorn worms, were present in the biological subcores and the X-radiographs showed evidence of bioturbation (Figs. 28-34, 37-46). For both March and May 2002 sites that had ^{7}Be present deeper than the surface layer, profiles show a logarithmic decrease with depth (Figs. 28-30, 32, 33, 36, 38, 40). Because only slight bioturbation is evident in X-radiographs, the gradients observed in ^{7}Be profiles suggest that sedimentation produced the decreasing profile. The presence of multiple silty layers throughout the ^{7}Be sediment interval indicates that there were multiple events that deposited sediment, with ^{7}Be decaying between events, as well as possibly eroding or mixing the sediment, within the past few months. When comparing the time-series sites from 2002, there was a general increase in inventory from March to May (Figs. 35 and 47), with sediment accumulating in the same general depocenter area west of Freshwater Bayou Canal as 2001. The depocenter occurred closer to the coastline in May than in March. This factor, combined with the changes of ^{7}Be inventories and profiles from 2001 to 2002, suggest that it is a dynamic feature on a seasonal time scale. Sediment containing ^{7}Be also seems to accumulate at the landward most sites along transects east of FWB Canal and south of SW Pass, with low amounts of ^{7}Be throughout the rest of the area. A number of sites that do not contain detectable ^{7}Be are located within the Atchafalaya River plume (Fig. 2), and the lack of ^{7}Be may be due to resuspension and transport occurring at those sites after initial sediment deposition. Beryllium-7 is not detectable at the seaward sites south of SW Pass (Figs. 35 and 47), which may be attributed to the sedimentology of the sites; these sites are sandy shoals and are local bathymetric highs. Although the sampling in 2001 occurred over a smaller area than 2002, the overall patchy distribution in 2002 differs from the distribution from May

2001, which shows much higher overall inventories and a thick ^{7}Be laden mud layer covering the entire region.

The 2001 sampling period took place after a large peak in river discharge (Fig. 6). The 2002 results were obtained during a different discharge regime of the river. Instead of one large peak, the shorter-lived pulses of river discharge allowed less water and sediment to be discharged at once, even if the total discharge of the year was more than 2001. As a result, with cold fronts and storms constantly reworking the area during the spring during periods of low river discharge (Fig. 49), previously deposited sediment could then be reworked before another pulse of discharge reached the study area.

An example of erosion occurring between March and May is time-series site BC10/14. At this site, the X-radiographs (Figs. 32 and 44) have horizontal silt laminations with evidence of erosional contacts. In March 2002, there were a number of acorn worms within the core, although the fabric did not appear disturbed. Beryllium-7 activities decreased with depth and penetrated to 14 cm. At the same site in May, there were no macrofauna, and the core had a scoured, eroded surface (Fig. 50). The scoured seabed is not unique to this particular site, as the sites furthest west also had a scoured, rippled seabed. Beryllium-7 penetrated only to 8 cm, and the overall inventory is lower in May than in March. Calculating the residual inventory at this site in May (Table 2), we found that the overall inventory is slightly higher than the residual inventory, which could indicate that net deposition did occur at this site. However, with the high error value, combined with the physical features of the core, there appears to be a loss of sediment from the seabed due to erosion.

In contrast to the erosion occurring at site BC 10/14, from March to May, time-series site BC3 shows net deposition. In March 2002 (Fig. 30), the X-radiographs showed horizontal

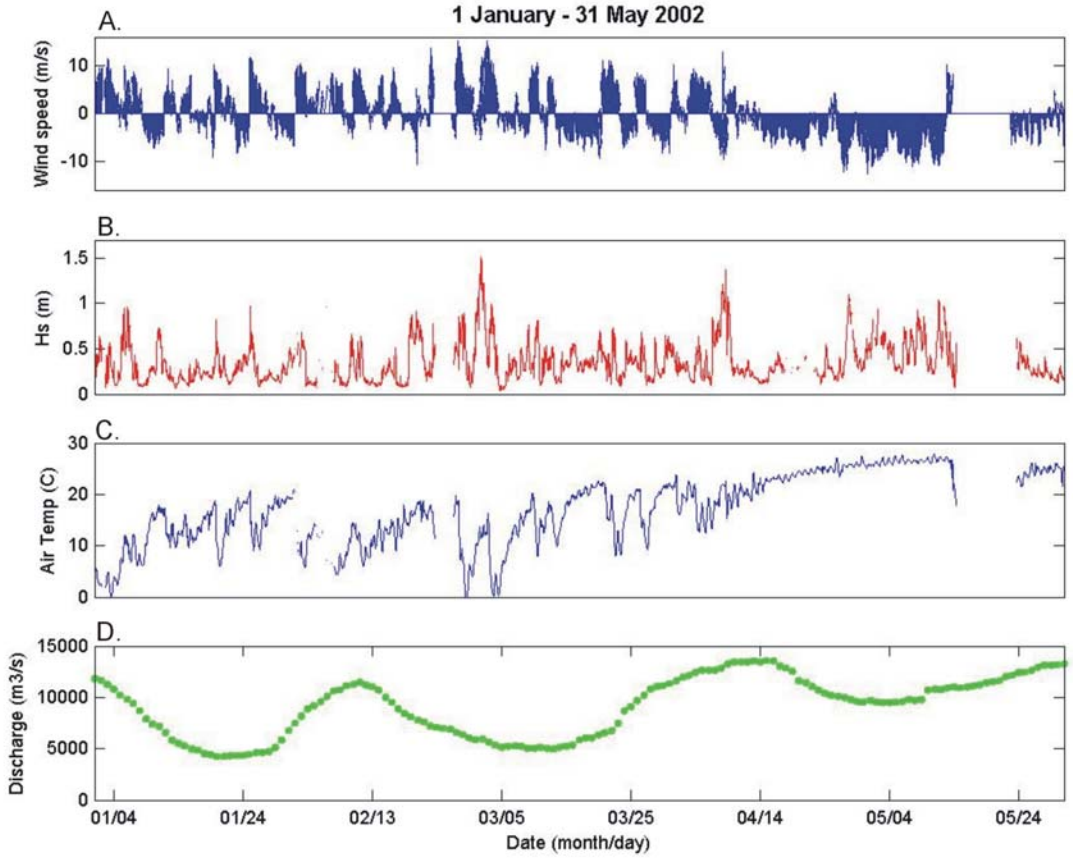

Figure 49. (A) Wind speed (m s^{-1}) and direction measured from the WAVCIS CSI-3 station; (B) Wave height (m) measured from CSI-3; (C) Air temperature (ºC) measured from CSI-3; (D) Atchafalaya River discharge hydrograph (m^3 s^{-1}), measured at Simmesport, LA (USACE). Increased wave heights generally coincident with strong southerly winds, and sharp drops in air temperature coincident with the switch to northerly winds indicate cold front passages. Cold fronts pass through the region every 3-7 days during both high and low river discharge.

laminations with little evidence of bioturbation. In the biological subsamples for this core, there were many polychaetes, although the X-radiograph showed little evidence of bioturbation. The surface of the core was pelletized, indicating that there was recent biological activity in the upper portion of the core. No stratified fluid mud was present on the surface, suggesting that no recent sedimentation had occurred at this site. The ^{7}Be activity decreased with depth, due to both biological mixing and radioactive decay. By comparison, at this site in May 2002 (Fig. 38), the upper layer of the core was muddy, physically layered and only a few small polychaetes were

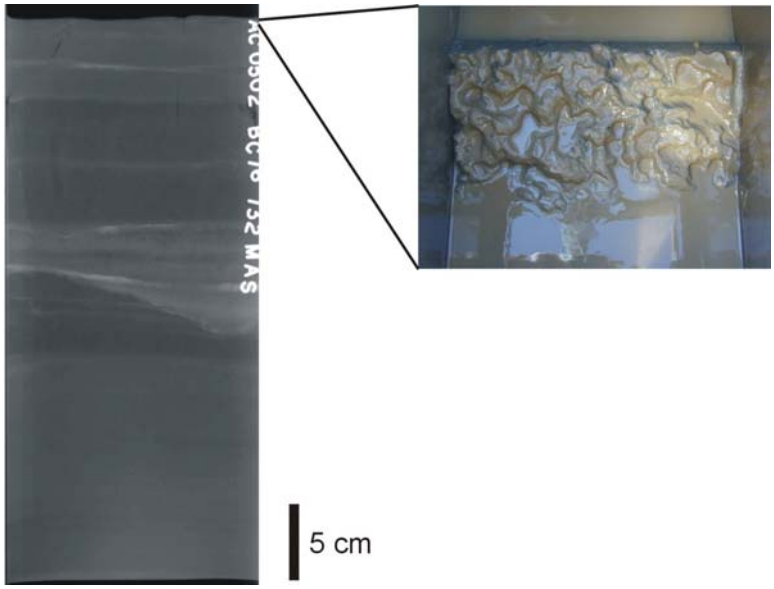

Figure 50. X-radiograph and surficial photograph of core AC0502 BC14. The photograph shows the scoured surface characteristic of wave erosion.

found in the core. Beryllium-7 activities also decrease with depth, but the overall activity is higher than in March, and ^{7}Be penetrates to a deeper depth. Since both the ^{7}Be activities and inventory are higher, and the new inventory is higher than the residual inventory (Table 2), there must be deposition of new sediment at this site between March and May 2002.

By quantifying the change in ^{7}Be inventories for the 2002 time-series sites (Table 2), we are able to determine that net erosion occurred west and south of the depocenter, while net deposition occurred in the May depocenter between March and May. This indicates a convergence of flux in this region along the coastline, allowing deposition to occur, although the exact mechanisms are still not well understood.

Gamma density logs and X-radiography of 2-3 m gravity cores show multiple mud/silt couplets downcore, exhibiting the same stratigraphic patterns seen in recent inner shelf deposits. The similar stratigraphy implies that the same processes creating beds evident in boxcores are creating strata preserved in gravity cores. X-radiography of the accumulating coastal mudflats

also shows the same stratigraphic features (*i.e.* mud/silt couplets) (Fig. 51), suggesting that the recent accumulation of seasonal flood layers is linked to the mudflat progradation on the Chenier Plain, as well as the longer-term sedimentary record on the inner shelf.

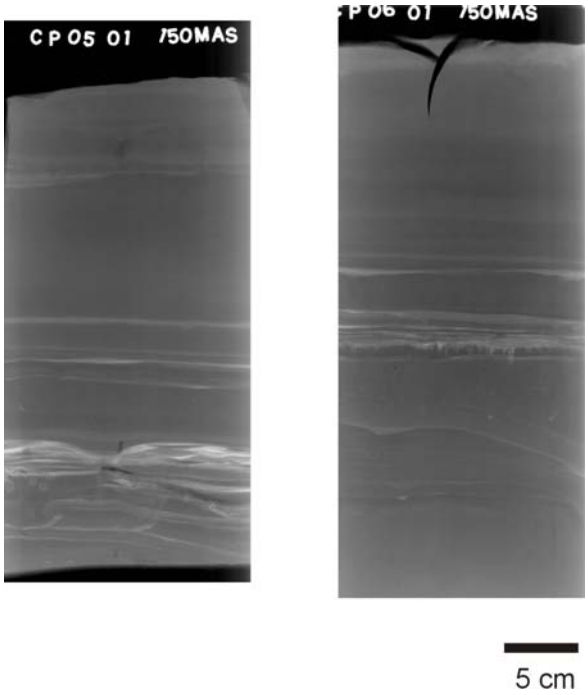

Figure 51. X-radiographs of cores CP0501 and CP0601, collected from the coastal mudflats of the western Louisiana Chenier Plain coast.

The increase in bulk density at ~ 100 cm is consistent within all the gravity cores (Figs 23-26). Using an average accumulation rate (determined by gamma analysis of gravity cores, Table 1) of 3.65 cm y^{-1}, we can date the grain size change to ~ 1974, which coincides with increased fine sediment supply from the Atchafalaya River, and associated mudflat progradation, that occurred after the 1973 flood.

Short-term accumulation rates determined in 2001 for the region can range from 10-25 cm y^{-1} during a year of high river discharge (Table 1). Long-term accumulation rates determined using ^{137}Cs and ^{210}Pb are consistent with each other and range from 2.9-4.1 cm y^{-1}, an order of magnitude lower than the short-term rates of seasonal accumulation estimated from ^{7}Be data. To

compensate for this, there must be a redistribution of the seasonally deposited sediment. Wright and Nittrouer (1995) recognize at least five stages in the dispersal of sediment once it leaves the river mouth (Fig. 52). Stage I is the initial deposition of bedload and flocculated sediments at the mouth of a river. Stage II (a, b) is the supply of sediment via buoyant plumes (either positive or negative) and stage III is the initial deposition of the sediment on the shelf. It is this stage that we are most likely seeing in the springtime deposition of thick fluid mud layers. Stage IV is resuspension (by waves, currents, or slope failure mechanisms) and further transport of the recently deposited sediment, either in the water column (IVa) or as a gravity-driven flow (IVb). It is this stage that is responsible for the discrepancy between short- and long-term accumulation rates of the region. Stage IV may occur a number of times before finally arriving at stage V: long-term net accumulation of sediment. Along the Chenier Plain coast, long-term accumulation may occur as mudflats along the coastline (Fig. 3), a phenomenon that has been well documented for the past half a century, or deposits on the shelf, which may be in the form of clinoform development consisting of the mud/silt couplets described from the X-radiographs. Clinoforms are sigmoidal-shaped sedimentary deposits consisting of a topset, foreset (which has the highest accumulation rates and appear to form in response to events of rapid sediment influx), and bottomset bed. Along the Fly River in the Gulf of Papua, New Guinea, clinoforms on the inner shelf result from fluid mud deposition during the annual trade-wind season (Walsh et al., in press).

Sidescan mosaics and chirp profiles (Figs. 17 and 18) showed the presence of a sediment lobe, and a smooth featureless seabed that seaward graded into a highly irregular seabed with acoustically transparent mud deposited on top (Roberts et al., 2002). The seabed bathymetry is gentle and arcuate, with the gradient becoming steeper seaward. The seaward edge has scarps

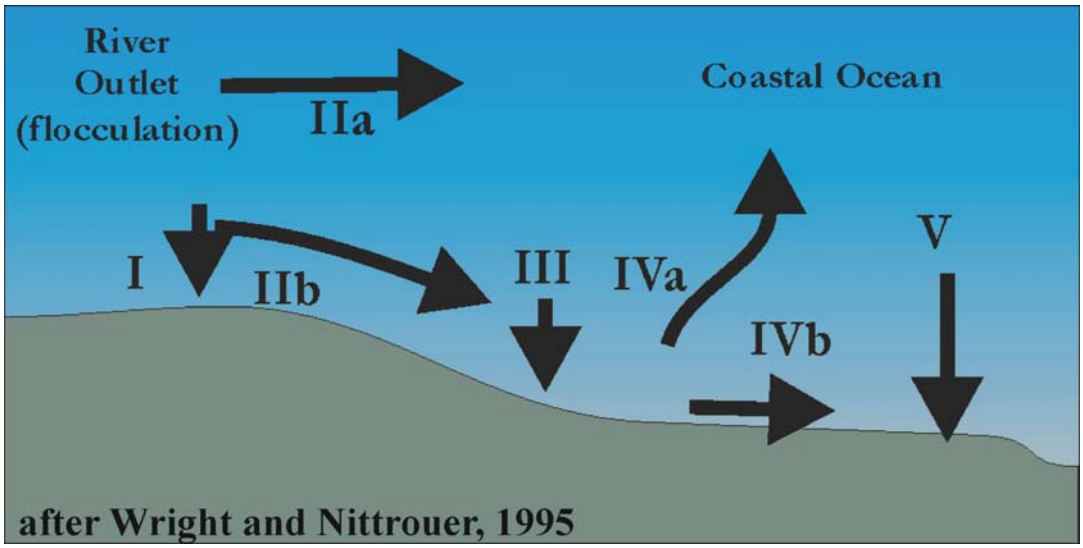

Figure 52. Schematic showing the patterns and processes of sediment dispersal over the continental shelf. The different stages of sediment dispersal, represented by roman numerals, are described within the text (after Wright and Nittrouer, 1995).

indicative of slope failure and appears locally eroded by wave action. While some of these irregular features may be a result of extensive trawling of the region, others are clearly a result of sediment failure or erosion. The irregular surface layer appears to be high-water-content mud that is related to, and perhaps constitutes the high-porosity event layers deposited in the spring. Chirp subbottom profiles (Fig. 18) show the formation of mud clinoforms extending to at least the ~5 m isobath**,** with a smooth surface landward, and progressively seaward, becoming more irregular with transparent muds (0.2-1 m thick) deposited on top.

Gravity-driven Transport on the Continental Shelf – A Hypothesis

Seabed and dynamical observations from the past two decades have shown that shelf-sediment dispersal mechanisms, particularly the rapid and widespread transport of fine sediment across continental shelves in dense, hyperpycnal flows (such as fluid muds) appear to be of global significance, rather than being a rare and special case. New technological developments that have allowed observations within the bottom boundary layer have only recently made it

possible to observe the dynamics of thin fluid mud layer *in situ*, and it is likely that gravity-driven transport of fluid mud may be more common than previously thought. For example, gravity-driven, down slope transport of fluid mud has been documented off the mouths of rivers such as the Zaire, Yellow, Amazon, and Eel (Wright et al., 2001).

The most widely recognized type of gravity-driven transport occurs on the continental slope, where the seabed slopes at angles greater than 0.7°, sufficient for downslope flow to occur (Fig. 53A). Turbulence due to bottom drag resuspends sediment, maintaining an auto-suspending gravity flow. If sufficient turbulence is not generated to maintain auto-suspension (*e.g.*, due to decreasing gradient, as on the continental slope-rise transition), the flow becomes depositional and stops moving. However, most continental shelves slope too gently to generate auto-suspending turbidity currents and sediment suspension by externally forced currents is required to maintain gravity currents (Wright et al., 2001). On a seabed that slopes at an angle less than 0.7°, gravity-driven flows can occur as long as there are waves or currents in the bottom-boundary layer to provide sufficient turbulence for sustained sediment suspension (Fig. 53B). In addition, enough easily suspended sediment is needed to exceed the resuspension capacity of the ambient currents. If there is not an adequate sediment supply, turbulence generated by ambient currents will increase bottom drag until a gravity flow can not occur. The amount of sediment an ambient current can carry is determined by the gradient Richardson number, *Ri*. The gradient Richardson number for the wave boundary layer is expressed by:

$$Ri \cong g s \frac{(\delta c' / \delta z)}{(\delta u / \delta z)^2} \quad \text{.....(3)}$$

where g is acceleration due to gravity, s is the submerged weight of the sediment relative to seawater, c is the suspended sediment concentration (ssc) within the wave boundary layer, z is

the elevation above the seabed, and u is the horizontal velocity. The gradient Richardson number compares the relative influence of buoyancy and shear on the generation of turbulence by shear instabilities within the wave boundary layer. For $Ri < ¼$, the turbulence associated with elevated shear instability increases ssc, thus increasing *Ri*, while for $Ri > ¼$, decreased shear instabilities reduce turbulence, allowing sediment to be deposited. This mechanism creates a negative feedback loop, maintaining $Ri \sim ¼$. Near this critical value, enough sediment remains in suspension to reduce shear, but turbulence maintains sediment in suspension as a fluid mud layer that can flow (Wright et al., 2001). This model demonstrates that gravity-driven flux of suspended mud is important on shelves where waves and currents provide the turbulence required to sustain a gravity driven flow. Much of the pioneering work on wave-enhanced gravity-driven flows has been conducted on the Eel River in northern California as a part of the ONR-sponsored STRATFORM program (Nittrouer, 1999).

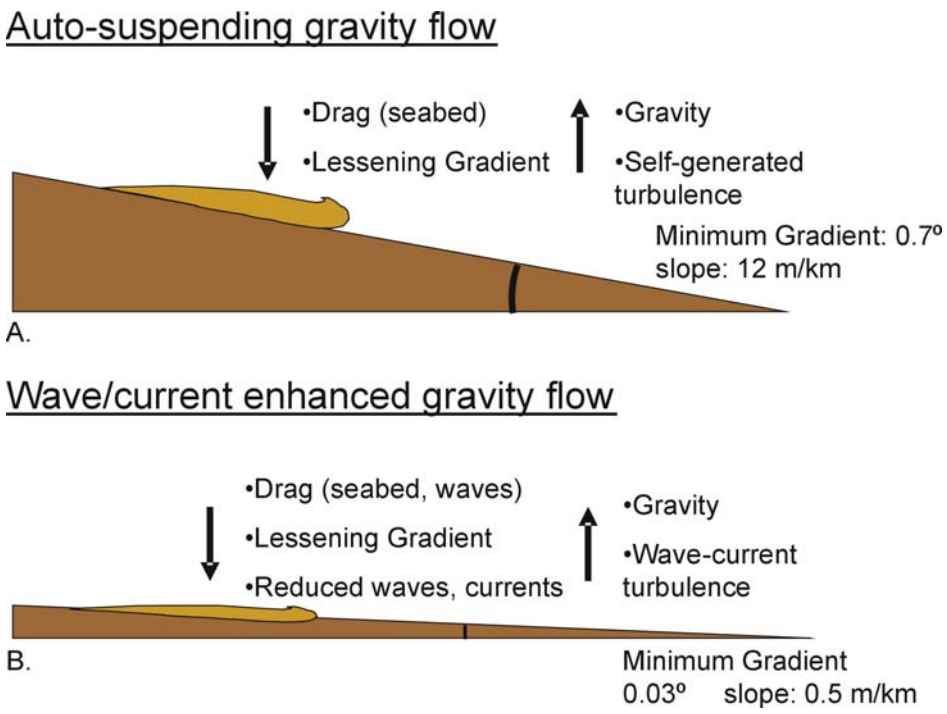

Figure 53. Schematic showing the different types of gravity-driven flows. (A). Auto-suspending gravity flow; (B) Wave-current enhanced gravity-driven flow.

The clinoform morphology of the inner shelf visible in the chirp profiles can be analyzed using an analytical model developed by Friedrichs and Wright (2003) as an equilibrium depositional profile under the influence of high sediment flux combined with wave shoaling and gravity-driven hyperpycnal flow.

Using the model for wave-enhanced gravity flow developed by Wright et al. (2001), Friedrichs and Wright (2003) developed an analytical model for equilibrium bathymetric profiles off river mouths associated with the shoreward, convex-upward portion of subaqueous deltas and clinoforms. This model serves as an explanation for the stratigraphic architecture seen on shelves dominated by wave-enhanced gravity-driven transport. Their analytical solution predicts specific depositional morphologies resulting from dynamic forcing. The model assumes that the equilibrium profile represents the balance between the supply of river sediment to the coast and the downslope bypassing of sediment to deep water within the wave-enhanced hyperpycnal flows. As a hyperpycnal flow moves downslope, it may deposit sediment due to either a decrease in bottom orbital velocity, bed slope, or both. This will form the convex upward portion of the front of a prograding clinoform. However, if the slope is steep enough and/or the wave-current induced resuspension is sufficiently intense to prevent deposition, then net bypassing will occur, resulting in a flat, non-depositional inner shelf (Friedrichs and Wright, 2003).

The model, using the key parameters of root-mean-squared wave height and river sediment discharge, predicts that the equilibrium profile increases with increased water depth and sediment supply (due to decreased orbital velocity), and decreases with increased wave height and wave period (due to increased orbital velocity). Thus, clinoform morphology changes with variations in wave climate and sediment flux. With high sediment supply and intense wave

reworking during cold fronts, westward and onshore sediment flux seen on the Atchafalaya shelf results in the inshore attenuation of wave-current energy and the formation of steep clinoforms (Fig. 54A). During periods of low sediment supply and intense wave reworking (such as during cold fronts or tropical systems that do not coincide with high river discharge), wave energy erodes the seabed and initiates downslope flow of fluid muds. This produces a lower gradient equilibrium profile with erosional remnants (Fig. 54B). Friedrichs and Wright (2003) have tested the model on the shelf profiles of the Eel (California), Waiapu (New Zealand), Po (Italy), Rhone (France) and Ganges (Bangladesh) rivers, and found that it successfully offered a first-order explanation of their stratigraphic architecture.

This model provides a hypothesis for the processes acting along the Atchafalaya shelf. The erosional features visible in the sidescan and chirp and the scoured seabed surfaces observed in box cores may have been formed during periods of low sediment supply from the river, but high wave activity. When maximum river discharge coincides with the high-energy cold front season, onshore sediment flux and inshore wave attenuation cause deposition of high-porosity (>85%, Figs. 8-12) beds on relatively steep clinoform fronts. Then during periods of cold front passage or storms that do not coincide with high river discharge, intense wave reworking causes erosion, leaving the scours and cavities visible in the sonar imagery. Hydrodynamic data collected across the western Louisiana inner shelf documents these wave-current resuspension events produced by the cold front passages (Fig. 19). Also, the total suspended sediment data collected before and after a cold front passage also indicates that sediment is resuspended due to the cold front passage, with increased resuspension occurring at the offshore stations (Fig. 21) where the erosional features are visible in the chirp data (Fig. 18 D-D'). After the sediment is resuspended, it may be moved across the shelf as a wave-enhanced gravity flow, thereby

decreasing the gradient of the clinoform front. If this process occurs soon after ^{7}Be-laden sediment is deposited in the depocenter region, it may result in the location of that depocenter moving seaward (*e.g.* seaward location of the March 2002 depocenter, Fig. 35). When the next period of high river discharge occurs, acoustically-transparent high-porosity mud is deposited on top of the previously eroded seabed, demonstrated in chirp sonar profile D-D' (Fig. 18).

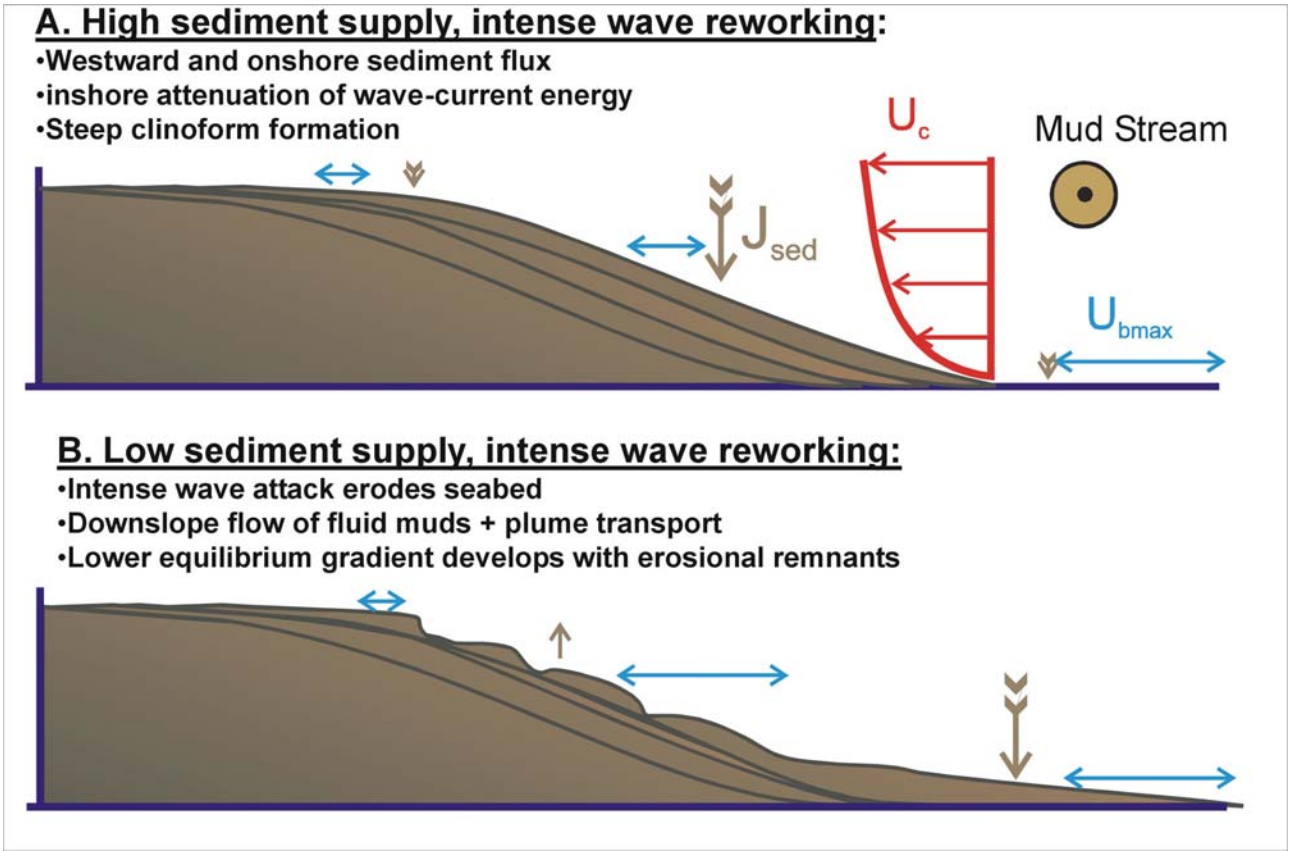

Figure 54. Schematic outlining the processes that occur to develop an equilibrium clinoform profile in the continental shelf. The vertical arrows depict either deposition or erosion with the arrow size indicating magnitude. The horizontal arrows depict U_{bmax}, with arrow size depicting magnitude of wave orbital velocity. (A) Westward and onshore sediment flux from the Atchafalaya mud stream. Progressive nearshore attenuation of waves decreases wave orbital velocities, resulting in deposition on the clinoform front; (B) With a low sediment supply but high wave energy, wave orbital velocities resuspend sediment on the clinoform front, causing wave-enhanced gravity-driven flow across the shelf and leaving erosional remnants on the clinoform front.

CONCLUSIONS

During the spring months, X-radiography, sedimentology, and radiochemistry indicate that there may be 2-25 cm of mud deposited along the Chenier plain coast, landward of the 10 m isobath, within 100 days following the high discharge period of the Atchafalaya River. These deposits, composed mainly of mud with basal silt laminae, can be ephemeral features on a seasonal scale. The stratigraphy of the event deposits is comparable to that observed in inner shelf gravity core and coastal mudflats, indicating formation by similar processes. The long-term sediment record obtained by gravity cores may show evidence of a major river flooding event, and the subsequent increase in fine sediment deposition along the Chenier Plain coast. Erosional features visible in X-radiographs and chirp data, as well as suspended sediment data, provide evidence for resuspension occurring due to the cold fronts that make passages through the region every 3-7 days from October to April. Long-term accumulation rates may be up to an order of magnitude lower than the short-term deposition of event beds, also indicating that some sediment is eroded and redistributed along or across the shelf.

The dispersal of fluvial sediments on the continental shelf is affected by a number of processes, with wave-enhanced gravity flows being the least understood, but possibly one of the most common. In the presence of high wave or current activity, fine sediment can be widely dispersed as a gravity-driven flow, even on low gradient shelves. This occurrence has been documented using bottom boundary layer instrumentation, seabed stratigraphy and geochronology in a number of regions, including the Eel, Amazon, and Fly rivers. Observations on the low-gradient western Louisiana inner shelf also indicate that these processes are active. Mud/silt couplets that comprise the fine-scale stratigraphy of the region, ephemeral ^{7}Be deposits, and clinoform morphology exhibiting erosional features in sidescan and chirp data all suggest

that wave-enhanced gravity flows may be an important mechanism for sediment dispersal, though more work is needed to quantify this phenomenon. Longer-term bottom boundary layer dynamical measurements and the fine scale study of the relationship between mud and silt layers should be examined for a better understanding of this process along the western Louisiana coastline.

REFERENCES

Allison, M.A., Kineke, G.C., Gordon, E.S., Goni, M.A., 2000. Development and reworking of a seasonal flood deposit on the inner continental shelf off the Atchafalaya River. Continental Shelf Research 20, 2267-2294.

Appleby, P.G., Oldfield, F., 1978. The calculation of ^{210}Pb dates assuming a constant rate of supply of unsupported ^{210}Pb to the sediment. Cantena 5, 1-8.

Bentley, S.J., 2003. Wave-current dispersal of fine-grained fluvial sediments across continental shelves: the significance of hyperpycnal plumes. In: Scott, E.K, Bouma, A.H., and Bryant, W.R. (Eds.), Depositional Processes and Characteristics of Siltstones, Mudstones and Shales. SEPM, Tulsa, pp. 35-48.

Bentley, S.J., Nittrouer, C.A., 1999. Physical and biological influences on the formation of sedimentary fabric in an oxygen-restricted depositional environment: Eckernforde Bay, Southwestern Baltic Sea. Palaios 14, 585-600.

Bentley, S.J., Nittrouer, C.A., 2003. Emplacement, modification and preservation of event strata on a flood-dominated continental shelf: Eel shelf, Northern California. Continental Shelf Research 23, 1465-1493.

Bentley, S.J., Rotondo, K.A., Roberts, H.H., Stone, G.W., Chan, S., 2003. Inner shelf clinoform development from fluid-mud deposition: Chenier Plain coast of Louisiana, USA.Geological Society of America National Meeting, Seattle, WA, November 2003.

Canuel, E.A., Martens, C.S., Benninger, L.K., 1990. Seasonal variations in ^{7}Be activity in the sediments of Cape Lookout Bight, North Carolina. Geochimica et Cosmochimica Acta 54, 237-245.

Coakley, J.P., Syvitski, J.P.M., 1991. Sedigraph technique: In: Syvitski, J.P.M. (Ed.), Principles, Methods, and Application of Particle Size Analysis. Cambridge, Cambridge University Press, 368 pp.

Cutshall, N.H., Larsen, I.L., Olsen, C.R., 1983. Direct analysis of ^{210}Pb in sediment samples: Self-absorption corrections. Nuclear Instrumentation Methods 206, 309-312.

Draut, A.E., 2003. Fine-grained sedimentation on the Chenier plain coast and inner continental shelf, Northern Gulf of Mexico: PhD dissertation, WHOI-MIT Joint Program, Boston, 369 pp.

Dukat, D.A., Kuehl, S.A., 1995. Non-steady-state ^{210}Pb flux and the use of ^{228}Ra/^{226}Ra as a geochronometer on the Amazon continental shelf. Marine Geology 125, 329-350.

Einstein, H.A., 1941. The viscosity of highly concentrated underflows and its influence on mixing. American Geophysical Union Transactions Hydrology Section, 597-603.

Fisk, H.N., 1952. Geological investigations of the Atchafalaya basin and the problem of Mississippi River diversion. U.S. Army Corps of Engineers, Mississippi River Commision, Vicksburg, Mississippi 1, 145 pp.

Fisk, H.N., McFarlan, E. Jr., 1955. Late Quaternary deltaic deposits of the Mississippi River. Geological Society of America Special Paper 62, 279-302.

Frazier, D.E., 1967. Recent deposits of the Mississippi River, their development and chronology. Transactions, Gulf Coast Association of Geological Societies 17, 287-315.

Friedrichs, C.T., Wright, L.D., 2003. Gravity-driven sediment transport on the continental shelf: Implications for equilibrium profiles near river mouths, in press.

Goldberg, E.D., 1963. Geochronology with ^{210}Pb. Radioactive Dating, Conference Proceedings, November 19-23, 1962, Athens, IAEA, 121-131.

Gould, H.R., McFarlan, E., Jr., 1959. Geologic history of the chenier plain, southwestern Louisiana. Transactions, Gulf Coast Association of Geological Societies 9, 237-270.

Howe, H.V., Russell, R.J., McGuirt, J.H., 1935. Physiography of coastal southwest Louisiana. Department of Conservation, Louisiana Geological Survey, New Orleans, Louisiana, Bulletin 6, 1-68.

Huh, O.K., Walker, N.D., Moeller, C., 2001. Sedimentation along the eastern chenier coast: Down drift impact of a delta complex shift. Journal of Coastal Research, 17, 72-81.

Kemp, G.P., 1986. Mud deposition at the shoreface: Wave and sediment dynamics on the Chenier Plain of Louisiana. PhD dissertation, Louisiana State University, Baton Rouge, 146 pp.

Kineke, G.C., Sternberg, R.W., 1995. Distribution of fluid muds on the Amazon continental shelf. Marine Geology 125, 193-233.

Kineke, G.C., Sternberg, R.W., Trowbridge, J.H., Geyer, W.R., 1996. Fluid-mud processes on the Amazon continental shelf. Continental Shelf Research 16, 667-696.

Kirby, R., 2002. Distinguishing accretion from erosion-dominated muddy coasts. In: Healy, T., Wang, Y. and Healy, J. (Eds.), Muddy Coasts of the World: Processes, Deposits and Functions Elsevier Science, pp. 61-81.

Kuehl, S.A., Pacioni, T.D., Rine, J.M., 1995. Seabed dynamics of the inner Amazon continental shelf: temporal and spatial variability of surficial strata. Marine Geology 125, 283-302.

Mehta, A.J., 1991. Understanding fluid mud in a dynamic environment. Geo-Marine Letters 11, 113-118.

Morgan, J.P., 1959. Coastal morphological changes resulting from Hurricane Audrey. Proceedings of the Salt Marsh Conference, University of Georgia Marine Institute, Sapelo Island Georgia, April 1959.

Morgan, J.P., Van Lopik, J.R., Nicholas, J.G., 1953. Occurrences and development of mudflats along the western Louisiana coast. Louisiana State University, Coastal Studies Institute, Technical Report 2, 34 pp.

Nittrouer, C.A., 1999. STRATAFORM, Overview of its design and synthesis of its results. Marine Geology 154, 3-12.

Nittrouer, C.A., DeMaster, D.J., McKee, B.A., Cutshall, N.H., Larsen, N.H., 1984. The effect of sediment mixing on ^{210}Pb accumulation rates for the Washington continental shelf. Marine Geology 54, 201-221.

Nittrouer, C.A., Sternberg, R.W., Carpenter, R., Bennett, J.T., 1979. The use of ^{210}Pb geochronology as a sedimentological tool: Application to the Washington continental shelf. Marine Geology 31, 297-316.

Ogsten, A.S., Cacchione, D.A., Sternberg, R.W., Kineke, G.C., 2000. Observations of storm and river flood-driven sediment transport on the northern California continental shelf. Continental Shelf Research 20, 2141-2162.

Roberts, H.H. 1997. Dynamic changes of the Holocene Mississippi River Delta Plain: The Delta Cycle. Journal of Coastal Research 13, 605-627.

Roberts, H.H., 1998. Delta switching: Early responses to the Atchafalaya River Diversion. Journal of Coastal Research 14, 882-899.

Roberts, H.H., Adams, R.D., Cunningham, R.H.W., 1980. Evolution of sand-dominant subaerial phase, Atchafalaya Delta, Louisiana. Association of Petroleum Geologists Bulletin 64, 264-279.

Roberts, H.H., Bentley, S.J., Coleman, J.M., Hsu, S.A., Huh, O.K., Rotondo, K.A., Inoue, M., Rouse, L.J., Jr., Sheremet, A., Stone, G., Walker, N., Welsh, S., Wiseman, W.J., Jr., 2002. Geological framework and sedimentology of recent mud deposition on the eastern Chenier Plain coast and adjacent inner shelf, western Louisiana: Transactions, Gulf Coast Association of Geological Societies 52, 849-859.

Roberts, H.H., Huh, O.K., Hsu, S.A., Rouse, L.J., Rickman, D.A., 1989. Winter storm impacts on the chenier plain coast of southwestern Louisiana. Transactions, Gulf Coast Association of Geological Societies 34, 515-522.

Russell, R.J., Howe, H.V., 1935. Cheniers of southwestern Louisiana. Geographic Reviews 25, 449-461.

Sommerfield, C.K., Nittrouer, C.A., Alexander, C.R., 1999. ^{7}Be as a tracer of flood sedimentation on the northern California continental margin. Continental Shelf research 19, 335-361.

Stone, G.W., Zhang, X.P., 2002. WAVCIS Main Page, http://wavcis.csi.lsu.edu/default.asp, draft March 6, 2002.

Stow, D.A., Bowen, A.J., 1980. A physical model for the transport and sorting of fine-grained sediment by turbidity currents. Sedimentology 27, 31-46.

Traykovski, P., Geyer, W.R., Irish, J.D., Lynch, J.F., 2000. The role of wave-induced density-driven fluid mud flows for cross-shelf transport on the Eel River continental shelf. Continental Shelf Research 20, 2113-2140.

Walker, N.D., Hammack, A.B., 2000. Impacts of winter storms on circulation and sediment transport: Atchafalaya-Vermilion Bay region, Louisiana, USA. Journal of Coastal Research, 16, 996-1010.

Walsh, J.P., Nittrouer, C.A., Palinkas, C.M., Ogston, A.S., Sternberg, R.W., Brunskill, G.J., 2003. Clinoform mechanics in the Gulf of Papua, New Guinea, in press.

Wang, Y., Healy, T. and Members of the SCOR Working Group 106: Augustinus, P., Baba, M., Bao, C., Flemming, B., Fortes, M., Han, M., Marone, E., Mehta, A., Ke, X., Kirby, T., Kjerfve, B., Schaefer-Novelli, Y., Wolanski, E., 2002. Research issues of muddy coasts. In: Healy, T., Wang, Y. and Healy, J. (Eds.), Muddy Coasts of the World: Processes, Deposits and Functions Elsevier Science, pp. 1-8.

Wells, J.T., Coleman, J.M., 1977. Nearshore suspended sediment variations, Central Surinam coast. Marine Geology 24, M47-M54.

Wells, J.T., Coleman, J.M., 1981. Physical processes and fine-grained sediment dynamics, coast of Surinam, South America. Journal of Sedimentary Petrology 51, 1053-1063.

Wells, J.T., Kemp, G.P.,1981. Atchafalaya mud stream and recent mudflat progradation: Louisiana Chenier Plain: Transactions, Gulf Coast Association of Geological Sciences 31, 409-416.

Wells, J.T., Roberts, H.H., 1981. Fluid mud dynamics and shoreline stabilization: Louisiana chenier plain. Proceedings of the Coastal Engineering Conference 17, 1382-1401.

Wright, L.D., Nittrouer, C.A.,1995. Dispersal of river sediments in coastal seas: Six contrasting cases. Estuaries 18, 494-508.

Wright, L.D., Friedrichs, C.T., Kim, S.C., Scully, M.E., 2001. Effects of ambient currents and waves on gravity-driven sediment transport on continental shelves. Marine Geology 175, 25-45.

APPENDIX A

MAY 2001 BOXCORE DATA

AC0501 BC1		(-92.38, 29.47)	
Depth interval (cm)	Porosity	^{7}Be activity (dpm g^{-1})	^{210}Pb$_{xs}$ activity (dpm g^{-1})
0-2	0.89	1.77 ± 0.24	5.97 ± 0.38
4-6	0.85	1.43 ± 0.22	5.00 ± 0.35
8-10	0.84	1.30 ± 0.21	5.42 ± 0.33
12-14	0.82	1.26 ± 0.21	6.22 ± 0.32
16-18			4.98 ± 0.30
20-22	0.81	ND*	4.57 ± 0.31
24-26	0.81		4.46 ± 0.36

AC0501 BC4		(-92.39, 29.50)				
Depth interval (cm)	Porosity	^{7}Be activity (dpm g^{-1})	^{210}Pb$_{xs}$ activity (dpm g^{-1})	% clay	% silt	% sand
0-2	0.93	2.28 ± 0.31	6.28 ± 0.47	93.6	3.9	2.5
2-4				90.2	7.2	2.6
4-6	0.87	2.35 ± 0.29	6.71 ± 0.34	90.2	9.5	0.3
6-8				90	6.6	3.4
8-10	0.87	1.96 ± 0.27	6.96 ± 0.42			
10-12				89.4	8.5	2.1
12-14	0.86	2.19 ± 0.30	6.13 ± 0.44	89.9	8.9	1.2
16-18	0.86	2.36 ± 0.26	7.49 ± 0.41	89.7	8.9	1.4
18-20				78.1	20.1	1.8
20-22	0.85	2.81 ± 0.32	7.07 ± 0.40	90.2	8.7	1.1
22-24				90	10	0
24-26	0.86	2.00 ± 0.64	6.52 ± 0.79			
26-28	0.84	ND	7.91 ± 0.43			
30-32	0.84		7.26 ± 0.40			
34-36	0.82		4.79 ± 0.37			
38-40	0.83		6.70 ± 0.40			

* ND = not detectable

AC0501 BC5		(-92.38, 29.51)	
Depth interval (cm)	Porosity	^{7}Be activity (dpm g^{-1})	$^{210}Pb_{xs}$ activity (dpm g^{-1})
4-6	0.92	1.82 ± 0.44	4.82 ± 0.34
8-10	0.92	2.13 ± 0.38	5.25 ± 0.30
12-14	0.89	2.97 ± 0.47	5.39 ± 0.27
16-18	0.90	2.42 ± 0.51	5.14 ± 0.33
20-22	0.88	1.50 ± 0.39	5.23 ± 0.30
24-26	0.88	2.57 ± 0.50	5.43 ± 0.30
28-30	0.86	ND	6.24 ± 0.38
32-34	0.88		5.80 ± 0.30
36-38	0.84		6.25 ± 0.31
40-42			5.23 ± 0.33

AC0501 BC6		(-92.38, 29.52)	
Depth interval (cm)	Porosity	^{7}Be activity (dpm g^{-1})	$^{210}Pb_{xs}$ activity (dpm g^{-1})
0-2	0.93	0.53 ± 0.35	5.86 ± 0.34
4-6	0.87	1.59 ± 0.38	6.81 ± 0.33
8-10	0.87	0.86 ± 0.45	6.51 ± 0.36
12-14	0.86	1.31 ± 0.41	5.93 ± 0.33
16-18	0.88	1.78 ± 0.52	7.33 ± 0.39
20-22	0.85	1.12 ± 0.40	6.60 ± 0.36
24-26	0.84	0.80 ± 0.34	6.00 ± 0.34
28-30	0.85	ND	5.65 ± 0.29
32-34	0.85		4.77 ± 0.31
36-38	0.83		4.80 ± 0.31
40-42	0.83		4.93 ± 0.29

AC0501 BC7		(-92.38, 29.53)	
Depth interval (cm)	Porosity	^{7}Be activity (dpm g^{-1})	$^{210}Pb_{xs}$ activity (dpm g^{-1})
0-2			4.34 ± 0.30
4-6	0.88	2.09 ± 0.64	4.97 ± 0.27
8-10	0.89	1.71 ± 0.48	6.09 ± 0.30
10-12			4.96 ± 0.29
12-14	0.84	1.80 ± 0.62	
16-18	0.85	1.30 ± 0.52	5.81 ± 0.33
20-22	0.85	ND	5.80 ± 0.30
24-26	0.84		5.65 ± 0.30
28-30	0.85		
32-34	0.86		5.87 ± 0.32

AC0501 BC8		(-92.43, 29.55)				
Depth interval (cm)	Porosity	^{7}Be activity (dpm g^{-1})	$^{210}Pb_{xs}$ activity (dpm g^{-1})	% clay	% silt	% sand
0-2	0.93	1.32 ± 0.42	7.76 ± 0.43	88.7	11.9	0
2-4				89.8	9.2	1
4-6	0.92	1.15 ± 0.31	6.32 ± 0.41	87.6	11.3	1.1
6-8				87	10.6	2.4
8-10	0.88	1.07 ± 0.28	6.18 ± 0.36	83.8	16.2	0
10-12	0.88	ND	6.65 ± 0.39	83.7	15.8	0.5
12-14				91.4	7.4	1.2
14-16				85.8	14.2	0
16-18	0.85		6.18 ± 0.36	78.5	18	3.5
18-20				79.6	19.1	1.3
20-22	0.82		4.52 ± 0.38	75.6	23.4	1
22-24				85.3	10.6	4.1
24-26	0.84		5.75 ± 0.36	85	11.6	3.4
26-28				83.5	16.5	0
28-30	0.83			85.7	12	2.3
30-32	0.83		5.23 ± 0.30	86.2	13.6	0.2

AC0501 BC9		(-92.43, 29.55)	
Depth interval (cm)	Porosity	^{7}Be activity (dpm g^{-1})	^{210}Pb$_{xs}$ activity (dpm g^{-1})
0-2	0.93	1.58 ± 0.38	4.90 ± 0.33
4-6	0.88	1.82 ± 0.47	4.94 ± 0.33
8-10	0.88	0.85 ± 0.46	4.88 ± 0.31
12-14	0.88	1.74 ± 0.41	5.00 ± 0.27
16-18	0.88	1.97 ± 0.47	5.10 ± 0.32
20-22	0.91	2.76 ± 0.58	5.34 ± 0.38
24-26	0.88	2.36 ± 0.61	4.37 ± 0.36
28-30	0.87	ND	6.41 ± 0.32
32-34	0.87		6.58 ± 0.43
36-38	0.87		7.01 ± 0.39
40-42	0.87		6.04 ± 0.33
44-46	0.85		4.80 ± 0.32
48-50	0.84		5.35 ± 0.32
50-52	0.81		5.25 ± 0.29

AC0501 BC14		(-92.40, 29.51)				
Depth interval (cm)	Porosity	^{7}Be activity (dpm g^{-1})	^{210}Pb$_{xs}$ activity (dpm g^{-1})	% clay	% silt	% sand
0-2	0.90	1.31 ± 0.29	7.17 ± 0.43	92	7	1
2-4				91.9	5.6	2.5
4-6	0.89	2.09 ± 0.36	7.42 ± 0.40	89.6	8.7	1.7
6-8				88	11.5	0.5
8-10	0.86	2.31 ± 0.32	7.24 ± 0.44	88.1	11.9	0
10-12				86.9	13.1	0
12-14	0.86	2.39 ± 0.33	7.25 ± 0.37			
14-16				86.4	13.6	0
16-18	0.85	0.43 ± 0.24	6.91 ± 0.42	84.6	14.2	1.2
18-20				86.4	13	0.6
20-22	0.85	0.56 ± 0.25	7.04 ± 0.40			
22-24				84.9	14.3	0.8
24-26	0.84	ND	3.80 ± 0.25			
26-28				88.1	11.2	0.7
28-30	0.83		6.50 ± 0.42	85.8	12.7	1.5
30-32				86.1	13.9	0
32-34	0.84		4.66 ± 0.27	88.2	11.1	0.7
34-36				86.9	10.5	2.6
36-38	0.82		3.40 ± 0.22	86.8	11.7	1.5
38-40				86.8	11.7	1.5
40-42			4.77 ± 0.31			

AC0501 BC15		(-92.40, 29.52)				
Depth interval (cm)	Porosity	^{7}Be activity (dpm g^{-1})	^{210}Pb$_{xs}$ activity (dpm g^{-1})	% clay	% silt	% sand
0-2	0.95	1.52 ± 0.37	6.47 ± 0.39	93.8	5.4	0.8
2-4				87.6	11	1.4
4-6	0.89	2.78 ± 0.37	6.06 ± 0.33	88.5	9	2.5
6-8				85.8	12.1	2.1
8-10	0.89	1.94 ± 0.38	7.21 ± 0.47	85.6	11.2	3.2
10-12				87.3	10	2.7
12-14	0.88	1.94 ± 0.35	6.59 ± 0.41	87.3	11.9	0.8
16-18	0.88	2.38 ± 0.39	6.29 ± 0.48	87.1	12.9	0
18-20				86.5	13.5	0
20-22	0.88	2.08 ± 0.46	6.15 ± 0.39	86.2	13.8	0
22-24				82	18	0
24-26	0.89	4.40 ± 0.88	6.61 ± 0.35	86.2	13.3	0.5
28-30				84.7	14.1	1.2
30-32	0.88	1.82 ± 0.54	6.15 ± 0.39	88.6	9.1	2.3
32-24				87.3	11.9	0.8
36-38				87.2	11.3	1.5
40-42	0.87	ND	4.94 ± 0.25	87.3	11.3	1.2
44-46				83.9	15	1.1
46-48	0.85		5.64 ± 0.32			
48-50				84	14.3	1.7
50-52	0.86		5.01 ± 0.26			
52-54				82.7	16.6	0.7
54-56	0.86					
56-58				84.6	15.8	0
58-60	0.84					

AC0501 BC16		(-92.40, 29.52)	
Depth interval (cm)	Porosity	^{7}Be activity (dpm g^{-1})	$^{210}Pb_{xs}$ activity (dpm g^{-1})
0-2	0.92	2.13 ± 0.37	4.95 ± 0.31
4-6	0.89	1.71 ± 0.30	4.78 ± 0.33
8-10	0.88	1.98 ± 0.41	5.97 ± 0.43
12-14	0.86	1.87 ± 0.55	4.63 ± 0.51
16-18	0.85	1.39 ± 0.32	5.13 ± 0.28
20-22	0.86	0.84 ± 0.30	5.41 ± 0.31
24-26	0.82	ND	4.92 ± 0.34
28-30	0.86		
32-34	0.84		

AC0501 BC17		(-92.40, 29.53)	
Depth interval (cm)	Porosity	^{7}Be activity (dpm g^{-1})	$^{210}Pb_{xs}$ activity (dpm g^{-1})
0-2	0.92	1.16 ± 0.66	4.18 ± 0.28
4-6	0.88	0.68 ± 0.58	3.72 ± 0.26
8-10	0.87	1.13 ± 0.48	4.34 ± 0.25
12-14	0.86	1.05 ± 0.64	4.83 ± 0.27
20-22	0.85	ND	4.60 ± 0.24

AC0501 BC18		(-92.41, 29.53)	
Depth interval (cm)	Porosity	^{7}Be activity (dpm g^{-1})	$^{210}Pb_{xs}$ activity (dpm g^{-1})
0-2	0.93	1.51 ± 0.37	6.10 ± 0.36
4-6	0.88	2.06 ± 0.43	6.47 ± 0.35
8-10	0.86	0.90 ± 0.36	7.39 ± 0.37
12-14	0.86	2.08 ± 0.40	6.47 ± 0.40
16-18	0.86	0.83 ± 0.37	6.31 ± 0.36
20-22	0.85	0.81 ± 0.50	6.84 ± 0.40
24-26	0.85	ND	5.06 ± 0.28
28-30	0.84		4.24 ± 0.29

AC0501 BC19		(-92.43, 29.53)				
Depth interval (cm)	Porosity	^{7}Be activity (dpm g^{-1})	^{210}Pb$_{xs}$ activity (dpm g^{-1})	% clay	% silt	% sand
0-2	0.91	1.99 ± 0.31	5.12 ± 0.28	77.2	22	22.8
2-4				89	9.3	11
4-6	0.89	1.88 ± 0.32	4.53 ± 0.25	89.6	8.7	10.4
6-8				89.4	10.4	10.6
8-10	0.87	1.08 ± 0.24	4.86 ± 0.28			
10-12				87.0	13.0	0
12-14	0.86	ND	4.30 ± 0.26	86	12.9	14
14-16				85.9	12.6	14.1
16-18	0.84		4.27 ± 0.23	86.7	11.8	13.3
18-20				84.3	13.3	15.7
20-22	0.83		4.69 ± 0.26	85.2	12.4	14.8
22-24				85.2	11.5	14.8
24-26	0.83		4.67 ± 0.31	84.5	15.5	0
26-28				86.2	13.2	13.8
28-30	0.83		5.52 ± 0.34	87.7	10.9	12.3
30-32				86.9	12.6	13.1
32-34	0.84		5.04 ± 0.30	87.6	9.1	12.4
34-36				86.8	11.9	13.2
36-38	0.82		5.30 ± 0.33	87.4	11.4	12.6
38-40	0.82		5.08 ± 0.29	84.5	15.5	0

AC0501 BC20		(-92.36, 29.49)				
Depth interval (cm)	Porosity	^{7}Be activity (dpm g^{-1})	^{210}Pb$_{xs}$ activity (dpm g^{-1})	% clay	% silt	% sand
0-2	0.89	0.60 ± 0.29	3.13 ± 0.19	75.8	23.3	0.9
2-4				70.4	28.4	1.2
4-6	0.86	1.06 ± 0.32	3.27 ± 0.23	75.6	24.4	0
6-8				76.3	22.4	1.3
8-10	0.88	2.54 ± 0.43	4.22 ± 0.23	87.9	9.2	2.9
10-12				75.3	21.5	3.2
12-14	0.87	1.32 ± 0.29	4.05 ± 0.22	84.7	15.3	0
14-16				83.1	16.7	0.2
16-18	0.84	1.15 ± 0.36	3.37 ± 0.23	83.8	13.4	2.8
18-20	0.82	ND	3.30 ± 0.20	71.8	28.2	0
22-24	0.85		5.22 ± 0.28	80.7	19.3	0
24-26				65.2	34.7	0.1
26-28	0.85		4.66 ± 0.29	66.9	33.1	0
28-30				82.3	17.7	0
30-32	0.84		4.77 ± 0.29	80.7	18.8	0.5
32-34				82.9	16.8	0.3
34-36	0.82		4.78 ± 0.29	79.5	20.2	0.3
36-38				80.3	19.7	0
38-40	0.82		4.33 ± 0.29	81.3	18.7	0

AC0501 BC21		(-92.35, 29.52)				
Depth interval (cm)	Porosity	^{7}Be activity (dpm g^{-1})	^{210}Pb$_{xs}$ activity (dpm g^{-1})	% clay	% silt	% sand
0-2	0.87	ND	3.96 ± 0.26	78.3	18.7	3
2-4				78.6	21.4	0
4-6	0.87		4.36 ± 0.28	78.8	19.5	1.7
6-8				78.7	20.7	0.6
8-10	0.84		4.49 ± 0.28	79.2	20.2	0.6
10-12				81.7	16.7	1.6
12-14	0.85		5.65 ± 0.31	84.9	14.1	1
14-16				83.4	15.7	0.9
16-18	0.84		4.59 ± 0.28	80.5	19.2	0.3
18-20				84.4	13	2.6
20-22	0.85		5.23 ± 0.20	84.7	14.3	1
22-24				83.7	15.8	0.5
24-26	0.84		14.73 ± 0.54			
26-28				79.5	20.1	0.4
30-32				88.0	12.0	0
32-34	0.84		4.81 ± 0.28			
34-36				85.6	13.1	1.3
36-37	0.83		5.55 ± 0.30			

APPENDIX B

MAY 2001 GRAVITY CORE DATA

AC0501 GC12		(-92.38, 29.53)	
Depth interval (cm)	$^{210}Pb_{xs}$ activity (dpm g^{-1}) γ	^{137}Cs activity (dpm g^{-1})	$^{210}Pb_{xs}$ activity (dpm g^{-1}) α
10-12			3.31
20-22			2.43
30-32	4.74 ± 0.30	0.34 ± 0.05	2.97
40-42	3.27 ± 0.24	0.11 ± 0.03	2.64
50-52	3.98 ± 0.27	0.27 ± 0.04	2.56
60-62	5.63 ± 0.34	0.37 ± 0.04	3.89
70-72	4.64 ± 0.27	0.31 ± 0.04	3.51
80-82	4.34 ± 0.25	0.26 ± 0.03	1.71
90-92	4.20 ± 0.26	0.27 ± 0.04	2.93
100-102	3.83 ± 0.22	0.22 ± 0.03	0.97
110-112	3.26 ± 0.20	0.33 ± 0.04	2.57
120-122	2.18 ± 0.17	0.26 ± 0.03	1.51
130-132	2.40 ± 0.18	0.31 ± 0.03	2.12
140-142	2.32 ± 0.20	0.25 ± 0.04	1.55
150-152	2.40 ± 0.21	0.50 ± 0.05	1.20
160-162	2.16 ± 0.17	0.30 ± 0.03	
170-172	1.93 ± 0.18	0.56 ± 0.05	0.95
180-182	2.07 ± 0.17	0.32 ± 0.04	3.50

AC0501 GC22		(-92.35, 29.53)	
Depth interval (cm)	$^{210}Pb_{xs}$ activity (dpm g^{-1}) γ	^{137}Cs activity (dpm g^{-1})	$^{210}Pb_{xs}$ activity (dpm g^{-1}) α
0-2			1.05
10-12			3.99
20-22	3.34 ± 0.24	0.16 ± 0.03	0.69
30-32	3.15 ± 0.18	0.16 ± 0.03	3.88
40-42	3.41 ± 0.21	0.26 ± 0.03	3.51
50-52	2.94 ± 0.22	0.13 ± 0.02	2.29
60-62	2.42 ± 0.17	0.14 ± 0.02	3.95
70-72	3.03 ± 0.20	0.17 ± 0.03	
80-82	2.27 ± 0.16	0.13 ± 0.03	3.71
90-92	2.48 ± 0.19	0.16 ± 0.03	1.92
100-102	2.86 ± 0.18	0.15 ± 0.03	4.14
110-112	2.47 ± 0.18	0.22 ± 0.03	1.74
120-122	1.97 ± 0.16	0.35 ± 0.03	0.78
130-132			
140-142			0.31
150-152	0.83 ± 0.12	0.25 ± 0.03	
160-162			1.15
174-176		0.20 ± 0.05	
176-178		0.56 ± 0.07	
180-182	0.97 ± 0.13	ND*	

* ND = not detectable

AC0501 GC23		(-92.37, 29.53)
Depth interval (cm)	$^{210}Pb_{xs}$ activity (dpm g^{-1}) γ	^{137}Cs activity (dpm g^{-1})
0-2	5.00 ± 0.33	0.36 ± 0.05
10-12	4.29 ± 0.32	0.34 ± 0.06
20-22	4.73 ± 0.29	0.33 ± 0.04
30-32	5.12 ± 0.32	0.28 ± 0.04
40-42	5.59 ± 0.34	0.32 ± 0.04
50-52	6.25 ± 0.42	0.34 ± 0.04
60-62	5.46 ± 0.31	0.37 ± 0.05
70-72	4.47 ± 0.29	0.39 ± 0.04
80-82	5.35 ± 0.35	0.37 ± 0.04
90-92	4.79 ± 0.33	0.36 ± 0.04
100-102	2.96 ± 0.30	0.40 ± 0.05
110-112	3.21 ± 0.26	0.41 ± 0.05
120-122	2.03 ± 0.20	0.40 ± 0.04
130-132	3.05 ± 0.27	1.38 ± 0.07
140-142	2.81 ± 0.29	1.51 ± 0.07
150-152	1.92 ± 0.19	0.85 ± 0.05

AC0501 GC27	(-92.39, 29.5)
Depth interval (cm)	$^{210}Pb_{xs}$ activity (dpm g^{-1}) α
10-12	2.22
20-22	3.29
30-32	2.71
40-42	2.33
50-52	2.53
60-62	3.87
70-72	2.81
80-82	2.20
90-92	2.35
100-102	1.39
110-112	1.01
120-122	0.81
130-132	1.19
140-142	1.40
150-152	0.60
160-162	0.93
170-172	0.79
180-182	0.74
190-192	4.04

AC0501 GC32		(-92.38, 29.49)	
Depth interval (cm)	$^{210}Pb_{xs}$ activity (dpm g^{-1}) γ	^{137}Cs activity (dpm g^{-1})	$^{210}Pb_{xs}$ activity (dpm g^{-1}) α
10-12			3.31
20-22			2.43
30-32	4.74 ± 0.30	0.34 ± 0.05	2.97
40-42	3.27 ± 0.24	0.11 ± 0.03	2.64
50-52	3.98 ± 0.27	0.28 ± 0.04	2.56
60-62	5.64 ± 0.34	0.37 ± 0.04	3.89
70-72	4.64 ± 0.27	0.31 ± 0.04	3.51
80-82	4.34 ± 0.25	0.26 ± 0.03	1.71
90-92	4.20 ± 0.26	0.27 ± 0.04	2.93
100-102	3.83 ± 0.22	0.22 ± 0.03	0.97
110-112	3.26 ± 0.20	0.33 ± 0.04	2.57
120-122	2.18 ± 0.17	0.26 ± 0.03	1.51
130-132	2.40 ± 0.18	0.31 ± 0.03	2.12
140-142	2.32 ± 0.20	0.25 ± 0.04	1.55
150-152	2.40 ± 0.21	0.50 ± 0.05	1.20
160-162	2.16 ± 0.17	0.30 ± 0.03	
170-172			0.95
174-176	1.93 ± 0.18	0.56 ± 0.05	
176-178	2.07 ± 0.17	0.32 ± 0.04	
180-182			3.50

APPENDIX C

MARCH 2002 BOXCORE DATA

AC0302 BC1		(-92.42, 29.45)			
Depth interval (cm)	Porosity	^{7}Be activity (dpm g^{-1})	% clay	% silt	% sand
0-2	0.8249583	2.03 ± 0.27	58.9	39.7	1.4
2-4		1.07 ± 0.28	66.8	32.1	1.1
4-6	0.8325854	ND*	71.3	28.7	0
6-8			71.8	27.9	0.3
8-10	0.8123874		70	28.1	1.9
10-12			62	35.7	2.3
12-14	0.8241925		76.1	22.1	1.8
14-16			80.1	19.5	0.4
16-18	0.8146266		78.2	20.8	1
18-20			76.2	23.7	0.1
20-22	0.7811599		77.9	21.1	1

*ND = not detectable

AC0302 BC2		(-92.42, 29.48)			
Depth interval (cm)	Porosity	^{7}Be activity (dpm g^{-1})	% clay	% silt	% sand
0-2	0.8361989	1.11 ± 0.20	72.9	25.2	1.9
2-4		2.35 ± 0.29	84.4	14.9	0.7
4-6	0.8447353	0.72 ± 0.17	81.4	17	1.6
6-8	0.8360564	0.37 ± 0.15	81.5	15.1	3.4
8-10		ND	80.4	17.2	2.4
10-12			79.6	17.2	3.2
12-14	0.8021378		78.4	20.8	0.8
14-16			78.8	17.9	3.3
16-18	0.8027917		76.3	22.6	1.1
18-20			80.2	17.8	2
20-22	0.8265665		83.3	15.1	1.6
22-24			85.7	11.6	2.7

AC0302 BC3		(-92.42, 29.51)			
Depth interval (cm)	Porosity	^{7}Be activity (dpm g^{-1})	% clay	% silt	% sand
0-2	0.8758761	0.86 ± 0.19	84.9	14.1	1
2-4	0.8564423	0.28 ± 0.24	80.7	18.9	0.4
4-6	0.8529098	ND	82	16.6	1.4
6-8			83.5	14.1	2.4
8-10	0.8392019		84.1	15	0.9
10-12			79.8	18	2.2
12-14	0.8376219		82.2	16.9	0.9
14-16			82	15.3	2.7
16-18	0.840711		81.7	17.4	0.9
18-20			79.2	17	3.8
20-22	0.8199212		79.2	17	3.8
22-24			82.5	16	1.5
24-26	0.8258618		77.3	21.4	1.3
26-28			77.3	21.8	0.9
28-30	0.8181044		78.6	21.2	0.2
30-32			79.4	17.3	3.3
32-34	0.7926407		78.1	20	1.9
34-36			75.1	23.8	1.1
36-38	0.8251633		81.5	16.2	2.3
38-40	0.8366797		79.5	20.5	0

AC0302 BC4		(-92.41, 29.54)			
Depth interval (cm)	Porosity	^{7}Be activity (dpm g^{-1})	% clay	% silt	% sand
0-2		ND	79.8	19.2	1
2-4			84	13.5	2.5
4-6			85	13.5	1.5
6-8			85.8	13	1.2
8-10			81.3	18.7	0
10-12			84.7	14.8	0.5
12-14			84.9	13.7	1.4
14-16			82.3	17.7	0
16-18			83.8	16.2	0
18-20			83.1	16.9	0
20-22			81.6	18.4	0
22-24			85.9	11.8	2.3
24-26			87.7	10.3	2
26-28			84	13.7	2.3
28-30			84.5	14.7	0.8
30-32			87.7	9.7	2.6
32-34			87.1	12.9	0
34-36			83.6	15	1.4
36-38			83.6	14.9	1.5
38-40			85.6	10.9	3.5

AC0302 BC5		(-92.48, 29.54)			
Depth interval (cm)	Porosity	^{7}Be activity (dpm g^{-1})	% clay	% silt	% sand
0-2	0.8449761	0.59 ± 0.15	80.1	79.1	19.9
2-4	0.8549694	ND	81.7	78.7	18.3
4-6	0.8365481		84.1	79.1	15.9
6-8			83.4	76.4	16.6
8-10			82.7	73.7	17.3
10-12			82.1	71.1	17.9
12-14			81.5	68.5	18.5
14-16			85	70	15
16-18			87.4	70.4	12.6
18-20			86	67	14

AC0302 BC6		(-92.44, 29.52)			
Depth interval (cm)	Porosity	^{7}Be activity (dpm g^{-1})	% clay	% silt	% sand
0-2	0.8597837	ND	91.2	8.2	0.6
2-4	0.8582135		90.4	9.6	0
4-6	0.8522408		89.7	8.5	1.8
6-8			90.4	9	0.6
8-10			88.1	10.1	1.8
10-12			86.9	12.1	1
12-14			85.6	13.2	1.2
14-16			85.4	13.2	1.4
16-18			89.3	9.7	1
18-20			89.5	9.6	0.9
22-24			88.5	11.2	0.3
24-26			88.4	9.9	1.7
26-28			88.3	10.3	1.4
28-30			88.3	9.7	2

AC0302 BC7		(-92.40, 29.51)			
Depth interval (cm)	Porosity	^{7}Be activity (dpm g^{-1})	% clay	% silt	% sand
0-2	0.8976435	0.41 ± 0.22	87.5	10.7	1.8
2-4	0.8624867	ND	87.9	11.7	0.4
8-10	0.8563999		83.4	14	2.6
10-12	0.8544253		82.3	14.6	3.1
12-14			83.7	15.4	0.9
14-16			83.1	16.4	0.5
16-18			82.6	14.9	2.5
18-20			83.6	16	0.4
20-22			82	14.5	3.5
22-24			79.8	17.1	3.1
24-26			82.3	17.7	0
26-28			81.6	17.3	1.1
28-30			80	18.3	1.7
30-32			79.1	19.8	1.1
32-34			81.6	18.1	0.3
34-36			76	23.7	0.3
36-38			78.3	20.4	1.3
38-40			80.1	18.2	1.7

AC0302 BC8		(-92.36, 29.50)			
Depth interval (cm)	Porosity	^{7}Be activity (dpm g^{-1})	% clay	% silt	% sand
0-2		ND	87.1	12.2	0.7
2-4			88	11.7	0.3
4-6			88.9	10.3	0.8
6-8			88.1	10.9	1
8-10			89.1	10.8	0.1
10-12			88.5	11.5	0
12-14			87.8	11.7	0.5
14-16			86.3	12.4	1.3

AC0302 BC9		(-92.27, 29.48)			
Depth interval (cm)	Porosity	^{7}Be activity (dpm g^{-1})	% clay	% silt	% sand
0-2	0.8482198	ND	70.4	27	2.6
2-4	0.8435716		76.4	22.4	1.2
4-6	0.8448747		77.6	21.3	1.1
6-8			78.9	19.5	1.6
8-10			79.2	17.6	3.2
10-12			76.3	22.8	0.9
12-14			81.7	15.9	2.4
14-16			76.9	21.5	1.6
16-18			76	20.7	3.3
18-20			83.6	16.1	0.3
20-22			85.3	14.6	0.1

AC0302 BC10		(-92.28, 29.52)			
Depth interval (cm)	Porosity	^{7}Be activity (dpm g^{-1})	% clay	% silt	% sand
0-2	0.9124848	1.50 ± 0.37	85	15	0
2-4			82.9	17.1	0
4-6	0.8922104	1.64 ± 0.38	78.9	19.2	1.9
8-10	0.881137	0.99 ± 0.33	81.6	18.4	0
10-12			80.4	19.6	0
12-14	0.8697502	0.49 ± 0.28			
14-16			79.4	17.4	3.2
16-18	0.869774	ND	77.2	21.8	1
18-20			83.2	16.8	0
20-22	0.8416582		83.2	16.8	0
22-24			79.3	19.4	1.3
24-26	0.8285488				
26-28			82.9	17.1	0
28-30	0.780638		85.4	14.6	0
30-32			89.3	10.7	0

AC0302 BC11		(-92,27, 29.45)			
Depth interval (cm)	Porosity	^{7}Be activity (dpm g^{-1})	% clay	% silt	% sand
0-2		ND	78.9	20	1.1
2-4			73.7	24.9	1.4
4-6			66.9	32.8	0.3
6-8			73	25.7	1.3
8-10			76.9	21.8	1.3
10-12			77.2	20.9	1.9
12-14			77.6	20.7	1.7
14-16			78.9	19.2	1.9
16-18			71.3	28.7	0
18-20			76	22.7	1.3
20-22			80.5	16.1	3.4
22-24			72.7	26.3	1
24-26			74.6	24.5	0.9

AC0302 BC12		(-92.07, 29.43)			
Depth interval (cm)	Porosity	^{7}Be activity (dpm g^{-1})	% clay	% silt	% sand
0-2	0.9286456	1.48 ± 0.41	86.5	13.2	0.3
2-4			64.7	35.1	0.2
4-6	0.7942593	0.70 ± 0.23	61.1	38.5	0.4
6-8	0.8345008	ND	64.7	32.6	2.7
8-10	0.7861825		55	42.9	2.1
10-12			59.5	39	1.5
12-14			64.9	32.8	2.3
14-16			67.2	31.4	1.4
16-18			65.3	33	1.7
18-20			72.8	26.4	0.8
20-22			74.2	25.8	0
22-24			73.3	26.5	0.2
24-26			77.3	19.9	2.8

AC0302 BC13		(-92.07, 29.38)			
Depth interval (cm)	Porosity	^{7}Be activity (dpm g^{-1})	% clay	% silt	% sand
0-2	0.9236537	2.72 ± 0.43	78.9	19.4	1.7
2-4			72.4	26.1	1.5
4-6	0.703388	ND	43.5	34.9	21.6
6-8	0.7462494		56.6	37.8	5.6
8-10	0.730701		62.7	32.5	4.8
10-12			55.7	39.5	4.8
12-14			63.6	32.7	3.7

AC0302 BC14		(-92.07, 29.33)
Depth interval (cm)	Porosity	^{7}Be activity (dpm g^{-1})
0-2		1.44 ± 0.40

AC0302 BC15		(-92.07, 29.28)
Depth interval (cm)	Porosity	^{7}Be activity (dpm g^{-1})
0-2		ND

AC0302 BC16		(-92.07, 29.23)
Depth interval (cm)	Porosity	^{7}Be activity (dpm g^{-1})
0-2		ND

APPENDIX D

MAY 2002 BOXCORE DATA

AC0502 BC1		(-92.42, 29.44)			
Depth interval (cm)	Porosity	^{7}Be activity (dpm g^{-1})	% clay	% silt	% sand
0-2	0.8724765	0.88 ± 0.23	76.6	21	2.4
2-4			72.3	27.7	0
4-6	0.8361545	0.42 ± 0.18	75.1	23.8	1.1
6-8	0.8257228	ND*	72.4	27.6	0
8-10			66.8	32.6	0.6
10-12			65.1	35.4	0
12-14			62.8	36.7	0.5
14-16			65.9	34.1	0
16-18			76.6	23.4	0
20-22			79.4	19.5	1.1
24-26			76.1	22.2	0

*ND = not detectable

AC0502 BC2		(-92.42, 29.48)			
Depth interval (cm)	Porosity	^{7}Be activity (dpm g^{-1})	% clay	% silt	% sand
0-2	0.8850466	ND	78.4	19.7	1.9
2-4			81.7	16.5	1.8
4-6	0.858533		81.8	17.7	0.5
6-8			76.2	22.6	1.2
8-10	0.8359211		77.7	22.1	0.2
10-12			78.5	20.7	0.8
12-14			78.9	19.9	1.2
14-16			79.6	19.3	1.1
16-18			78.3	21.4	0.3
18-20			78.6	19.9	1.5
20-22			79	20.8	0.2
22-24			80.7	17.7	1.6

AC0502 BC3		(-92.41, 29.51)			
Depth interval (cm)	Porosity	^{7}Be activity (dpm g^{-1})	% clay	% silt	% sand
0-2	0.9250094	1.40 ± 0.30	84	14.9	1.1
2-4			82.8	15.3	1.9
4-6	0.877562	1.13 ± 0.25	82.5	17.3	0.2
6-8			84.4	13.8	1.8
8-10	0.8559775	0.59 ± 0.23			
10-12	0.8407027	ND	85.7	13.1	1.2
12-14			79.4	20.6	0
14-16			79	20.1	0.9
16-18			85.7	13.6	0.7
18-20			82.6	16.4	1
20-22			85.8	12.7	1.5
22-24			82.3	17.1	0.6
24-26			82	17.5	0.5
26-28			82.4	16.4	1.2
28-30			78.3	21.1	0.6
30-32			74.3	25.6	0.1
32-34			80.6	19.4	0
34-36			82.4	17.5	0.1

AC0502 BC4		(-92.42, 29.54)			
Depth interval (cm)	Porosity	^{7}Be activity (dpm g^{-1})	% clay	% silt	% sand
0-2	0.9201817	ND	85.5	11.8	2.7
2-4			84.9	13.8	1.3
4-6	0.9069767		84.3	12.8	2.9
6-8			83.9	15	1.1
8-10	0.9012006		87.1	11.3	1.6
10-12			69	30.2	0.8
12-14	0.90343		85.8	13.1	1.1
14-16			85.6	13.3	1.1
16-18			68.2	28.8	3
18-20			85.3	13.8	0.9
20-22			86.7	11.8	1.5
22-24			86.1	9.7	4.2
24-26			88.9	9.7	1.4
26-28			67.3	32	0.7
28-30			83.4	16.6	0
30-32			76.2	20.2	3.6
32-34			72.5	26.9	0.6
34-36			80	16.8	3.2
36-38			89.9	9.3	0.8
38-40			86.0	14.0	0
40-42			81.8	15.9	2.3

AC0502 BC5		(-92.41, 29.54)			
Depth interval (cm)	Porosity	^{7}Be activity (dpm g^{-1})	% clay	% silt	% sand
0-2	0.9141052	1.73 ± 0.26	84.8	15.2	0
4-6	0.898749	2.01 ± 0.30	80.7	18.7	0.6
8-10	0.8582071	0.48 ± 0.15			
10-12	0.8609409	ND			
12-14			71.4	26.9	1.7
14-16			70.5	28.4	1.1
16-18			69.1	30.9	0
18-20			68.2	31.8	0
20-22			58.9	37.5	3.6
22-24			70.6	28.4	1
24-26			78.5	21.5	0
26-28			83.7	15.8	0.5
28-30			73.7	24.9	1.4
30-32			78.3	17.9	3.8

AC0502 BC6		(-92.49, 29.53)			
Depth interval (cm)	Porosity	^{7}Be activity (dpm g^{-1})	% clay	% silt	% sand
0-2	0.7727725	ND	73.5	26.5	0
2-4			77.9	17.2	4.9
4-6	0.7945451		78.5	18.1	3.4
6-8			79.2	18.4	2.4
8-10	0.798025		86	12.5	1.5
10-12			79.4	20.6	0
12-14			83.7	14.8	1.5
14-16			79.6	17.1	3.3
16-18			82.9	14.8	2.3
18-20			81.5	16.3	2.2

AC0502 BC7		(-92.45, 29.52)			
Depth interval (cm)	Porosity	^{7}Be activity (dpm g^{-1})	% clay	% silt	% sand
0-2	0.8902844	ND	79	19.2	1.8
2-4			75.7	24.3	0
4-6	0.8368402		73.7	25.2	1.1
6-8			73.8	25.2	1
8-10	0.8115512		75	23.6	1.4
10-12			76.5	21.7	1.8
12-14			77.2	20.9	1.9
14-16			79.8	18.6	1.6
16-18			80.8	18.9	0.3
18-20			78.7	18.5	2.8
20-22			79.6	19	1.4
22-24			82	15.3	2.7

AC0502 BC8		(-92.41, 29.51)			
Depth interval (cm)	Porosity	^{7}Be activity (dpm g^{-1})	% clay	% silt	% sand
0-2	0.8907113	2.36 ± 0.33	82.6	15	2.4
2-4			83.7	13.8	2.5
4-6	0.8799408	1.51 ± 0.31	84.6	13	2.4
6-8			82.7	17.2	0.1
8-10	0.866168	1.01 ± 0.35	82.8	14.6	2.6
10-12			83.3	13.7	3
12-14	0.8581368	0.80 ± 0.25	82.1	16.7	1.2
14-16			82.7	14.9	2.4
16-18	0.8506766	1.22 ± 0.36	81.9	17.9	0.2
18-20			82.2	13.1	4.7
20-22	0.8410007	0.67 ± 0.34	83.1	14.6	2.3
22-24			84.1	13.4	2.5
24-26	0	ND	81.3	15	3.7
24-26			83.5	13.4	3.1
26-28			81.2	15.8	3
28-30			79.5	18.8	1.7

AC0502 BC9		(-92.36, 29.53)			
Depth interval (cm)	Porosity	^{7}Be activity (dpm g^{-1})	% clay	% silt	% sand
0-2	0.9053226	0.44 ± 0.27	77.3	22.1	0.6
2-4		ND	75.9	23.2	0.9
4-6	0.8825353		79.2	20.4	0.4
6-8			81.2	18.2	0.6
8-10	0.8744857		84.5	16.4	0
10-12			83.9	16.4	0
12-14			79.2	19.8	1
14-16			78.5	19.3	2.2
16-18			77.6	21.2	1.2
18-20			76.9	22.7	0.4

AC0502 BC10		(-92.36, 29.50)			
Depth interval (cm)	Porosity	^{7}Be activity (dpm g^{-1})	% clay	% silt	% sand
0-2	0.9057972	ND	79.6	20	0.4
2-4			79.8	19.8	0.4
4-6	0.8479597		83.9	14.3	1.8
6-8			84.3	14.7	1
8-10	0.8223385		82.7	15.9	1.4
10-12			82.5	15.8	1.7
12-14			81.6	14.9	3.5
14-16			80.3	17.6	2.1
16-18			79	18.2	2.8
18-20			79.2	20.2	0.6

AC0502 BC11		(-92.36, 29.48)			
Depth interval (cm)	Porosity	^{7}Be activity (dpm g^{-1})	% clay	% silt	% sand
0-2	0.8489241	ND	72.7	25.2	2.1
2-4	0.8075956		72.2	25.6	2.2
4-6	0.8110595		66.6	32.1	1.3
6-8			73	25.4	1.6
8-10			79.1	15.6	5.3
10-12			79.8	18.2	2
12-14			80.6	18.6	0.8
14-16			76.6	23.4	0
16-18			70.8	26.8	2.4
18-20			68.5	25.7	5.8
20-22			65.9	30.8	3.3
22-24			68	30.9	1.1
24-26			69.7	27.6	2.7
26-28			72.9	24.4	2.7
28-30			74.7	23.9	1.4
30-32			74.8	23.6	1.6

AC0502 BC12		(-92.28, 29.45)			
Depth interval (cm)	Porosity	^{7}Be activity (dpm g^{-1})	% clay	% silt	% sand
0-2	0.8797217	0.92 ± 0.25	77.2	21.6	1.2
2-4	0.8482986	ND	77.8	21.8	0.4
4-6	0.8057277		66.2	32.4	1.4
6-8			68.8	29.8	1.4
8-10			72.4	25.5	2.1
10-12			76.4	20.2	3.4
12-14			80.8	18.5	0.7
14-16			77.9	22.1	0
16-18			77.6	20.7	1.7
18-20			73	26.8	0.2
20-22			78.3	19.8	1.9
22-24			83.9	16	0.1
24-26			82.5	15.8	1.7
26-28			78.4	21.6	0
28-30			74.2	23.1	2.7
30-32			78.4	20.4	1.2
32-34			77.4	22.6	0

AC0502 BC13		(-92.28, 29.48)			
Depth interval (cm)	Porosity	^{7}Be activity (dpm g^{-1})	% clay	% silt	% sand
0-2	0.8971316	1.40 ± 0.37	78.2	20.6	1.2
2-4			78.3	19.4	2.3
4-6	0.8347486	1.08 ± 0.27	68.8	30.6	0.6
6-8		ND	72.1	25.5	2.4
8-10			74.8	21.9	3.3
10-12			75.6	22.7	1.7
12-14			72.7	25.5	1.8
14-16			79.4	17.7	2.9
16-18			82.6	16.7	0.7
18-20			77.6	20.2	2.2
20-22			80.4	17.1	2.5
22-24			85	13.4	1.6
24-26			81.7	15.2	3.1
26-28			78.1	19.6	2.3
28-30			72.4	26.6	1
30-32			77.9	18.4	3.7
32-34			72.2	23.6	4.2
34-36			71.6	27.1	1.3
36-38			74.0	26.0	0
38-40			82.2	15.4	2.4

AC0502 BC14		(-92.28, 29.52)			
Depth interval (cm)	Porosity	^{7}Be activity (dpm g^{-1})	% clay	% silt	% sand
0-2	0.8728426	1.01 ± 0.37	77.2	20.4	2.4
2-4			79.1	19.5	1.4
4-6	0.8704078	0.87 ± 0.42	81.3	18.2	0.5
6-8	0.8653016	0.52 ± 0.36	78.8	20.5	0.7
8-10	0.8564115	ND	77	19.6	3.4
10-12			76.6	20.2	3.2
12-14			89.4	8	2.6
14-16			80.3	18.2	1.5
16-18			74.8	21.9	3.3
18-20			71.3	27.6	1.1
20-22			76.6	20.4	3
22-24			81.1	15.5	3.4

AC0502 BC15		(-92.07, 29.23)			
Depth interval (cm)	Porosity	^{7}Be activity (dpm g^{-1})	% clay	% silt	% sand
0-2	0.5149178	ND	2.5	22.6	74.9
2-4	0.5945676		13.6	26.4	60
4-6	0.6210893		21.1	35.6	43.3
6-8			41.2	45.6	13.2
8-10	0.6582006		43.9	33.7	22.4
10-12			46.2	35.9	17.9

AC0502 BC16		(-92.07, 29.28)			
Depth interval (cm)	Porosity	^{7}Be activity (dpm g^{-1})	% clay	% silt	% sand
0-2	0.4561143	ND	40.6	38.6	20.8

AC0502 BC17		(-92.07, 29.33)
Depth interval (cm)	Porosity	^{7}Be activity (dpm g^{-1})
0-2	0.574929	ND

AC0502 BC18		(-92.07, 29.38)
Depth interval (cm)	Porosity	^{7}Be activity (dpm g^{-1})
0-2	0.8337016	2.26 ± 0.33
2-4	0.8461784	1.73 ± 0.36
4-6		1.24 ± 0.51
6-8		
8-10	0.6458555	ND

AC0502 BC19		(-92.07, 29.42)			
Depth interval (cm)	Porosity	^{7}Be activity (dpm g^{-1})	% clay	% silt	% sand
0-2	0.8194669	0.57 ± 0.32	59.4	38.8	1.8
2-4			56.9	40	3.1
4-6	0.7751417	ND	61.9	30.6	7.5
6-8			68.7	28.1	3.2
8-10			55.2	27.7	17.1
10-12			65.6	28.4	6
12-14			66.4	30.3	3.3
14-16			58.5	38.8	2.7
16-18			65.4	31.2	3.4
18-20			64.4	31.9	3.7

VITA

Kristina Rotondo was born on March 29, 1978, in Newburgh, New York. She graduated from Newburgh Free Academy in June 1996. She received a Bachelor of Arts degree in geological sciences at the State University of New York at Geneseo in May 2000. After spending a year "finding herself", while attending the University of British Columbia in Vancouver, British Columbia, for a semester and substitute teaching in New York, she began a graduate program in the Coastal Studies Institute of the Department of Oceanography and Coastal Sciences at Louisiana State University in August 2001. Kristina is currently a candidate for the Master of Science degree in the Department of Oceanography and Coastal Sciences.